

TFY4705

---

WAXS studies of water transport in a  
layered synthetic silicate

*Lars Ramstad Alme*

*Supervisor: Professor Dr.ing. Jon Otto Fossum*

---

DEPARTMENT OF PHYSICS — NTNU SPRING 2006

# Abstract

This project was an experimental Wide Angle X-ray Scattering (WAXS) study on different aspects of water transport through a powder sample of a nanoporous layered synthetic smectite clay, Na-fluorohectorite. Na-fluorohectorite crystallites, like all smectites, are able to swell due to intercalation of water between the fundamental layer silicate. The dynamics of such a process is reflected in the scattering signature and can be directly related to the interlayer distance through application of Bragg's law.

The temperature was lowered, and a fixed humidity gradient was imposed on a quasi one dimensional powder sample thereby initiating the transition from a monohydrous state to a bi-hydrated state implying the intercalation of one monolayer of water into the interlayer spacing. Applying a pseudo-Voigtian function the Bragg peaks were fitted and the normalized hydration states estimated. These are believed to be proportional to the ratio of crystallites in a representative scattering volume existing in the corresponding mono- or bi-hydrated state. The signature of mixed intercalation states in the neighbourhood of the intercalation front was demonstrated.

The intercalation front was shown to be modulated with a stretched exponential. The width and speed of the front through a sample volume was shown to increase with time and/or spatial ingress. Suggestions of anomalous behaviour were evident, however the crude inaccuracy did not allow for any definite conclusions at this point.

Finally an ordered (linear) and small displacement in the monohydrated peak center position was observed over a significant spatial interval for positions far from the intercalation front. This is suggested to be related to the water vapor front and the ingress of *small* amounts of water molecules into the interlayer spacing without altering the water layer *state* itself, only its dimensionality.

# Pretext

The project work was performed during the spring semester 2006 at the *Complex Systems and Soft Material Group* at the Norwegian University of Science and Technology (NTNU), Department of Physics, in Trondheim, and is a compulsory subject in the 9th semester of the Master of Science (norwegian: 'sivilingeniør') degree.

The work has given a good insight into practical lab work, thorough preparations and data acquisitions, as well as the subsequent extensive and demanding data processing and analyzing process.

I greatly acknowledge my supervisor, professor Jon Otto Fossum, for extensive training on the X-ray instrument as well as invaluable guidance and motivation on the data evaluation. A special thanks also goes to Yves Méheust for his ideas and contributions to the data analysis, especially with the fitting function. I would also like to thank the staff at Bruker for useful guidance in solving hardware problems concerning the X-ray apparatus as well as professor Geraldo Jose da Silva for helpful discussions on certain theoretical matters.

Trondheim, June 22nd, 2006

Lars Ramstad Alme



# Contents

<b>1 Theory</b>	<b>1</b>
1.1 Clays . . . . .	1
1.1.1 General considerations . . . . .	2
1.1.2 Smectite clays . . . . .	5
1.1.3 Hectorite . . . . .	10
1.1.4 Na-fluorohectorite . . . . .	10
1.2 X-ray diffraction (XRD) . . . . .	11
1.2.1 Diffraction . . . . .	12
1.2.2 Interference . . . . .	13
1.2.3 Bragg's law of diffraction . . . . .	13
1.2.4 From one electron to a complete lattice . . . . .	14
1.2.5 Kinematic scattering . . . . .	18
1.2.6 Powder diffraction . . . . .	21
1.2.7 Putting it all together: The complete differential cross-section for a crystal . . . . .	22
1.2.8 Scattering from a layered clay . . . . .	23
1.2.9 Putting it all together: Intensity for a layered clay . . . . .	26
1.2.10 Modelling the intensity for Na-fluorohectorite . . . . .	27
1.2.11 Peak width . . . . .	32
1.2.12 Hendricks-Teller state . . . . .	34
1.3 Diffusion . . . . .	36
1.3.1 Normal diffusion . . . . .	38
1.3.2 Anomalous diffusion . . . . .	39
1.3.3 Method . . . . .	41
1.4 Pseudo-Voigtian approximation . . . . .	41
1.4.1 Gaussian distribution . . . . .	41
1.4.2 Lorentzian distribution . . . . .	41
1.4.3 Convolution . . . . .	42
1.4.4 Voigtian distribution . . . . .	43
1.4.5 Pseudo-Voigtian distribution . . . . .	43
1.4.6 Application . . . . .	44
<b>2 Experiment</b>	<b>45</b>
2.1 Experimental setup . . . . .	45
2.1.1 Components of the SAXS system . . . . .	45
2.1.2 Sample holder . . . . .	48
2.1.3 Software . . . . .	48
2.2 Experimental method . . . . .	49

2.2.1	Clay sample . . . . .	49
2.2.2	Scattering geometry . . . . .	50
2.2.3	Preparations . . . . .	52
2.2.4	Scans . . . . .	53
2.2.5	Series . . . . .	54
<b>3</b>	<b>Data processing, analysis and results</b>	<b>55</b>
3.1	Data aquisition and processing . . . . .	55
3.1.1	Frames . . . . .	55
3.1.2	Integration . . . . .	56
3.1.3	Normalization . . . . .	57
3.1.4	Peak fitting . . . . .	58
3.2	Data analysis . . . . .	62
3.2.1	General observations . . . . .	62
3.2.2	Dynamics of water intercalation . . . . .	69
3.2.3	Hydrophilic character of glass capillaries . . . . .	80
3.2.4	Disordered/mixed intercalation . . . . .	81
3.3	Discussion . . . . .	83
3.3.1	Peak displacement . . . . .	83
3.3.2	Anomalous transport . . . . .	85
<b>4</b>	<b>Conclusion</b>	<b>88</b>
<b>A</b>	<b>Lattice sum as Dirac's delta function</b>	<b>94</b>
<b>B</b>	<b>Calculations of atomic form factor</b>	<b>95</b>
B.1	Detailed expression for the atomic form factor . . . . .	95
B.2	Calculations . . . . .	95
B.3	Atomic scattering factor squared . . . . .	99
<b>C</b>	<b>MatLab script for peak fitting</b>	<b>103</b>

# Chapter 1

## Theory

### 1.1 Clays

Clays represents one of the traditional materials which applications have played a major role in traditional as well as modern history; ceramics, building material, rheology modifications, catalysis and barriers for high level radioactive waste just to mention a few. Apart from these traditional approaches and disciplines, the fundamental studies of clay is merely at its beginning.

The majority of natural occurring clays are heterogene mineral mixtures. However, the increasing availability of pure chemistry synthesized clays, rendering possible well controlled chemistry and structure, has led to a deeper interest for clays as interesting and available experimental as well as theoretical model systems, and clays have subsequently been included in modern material science along with often better understood synthetic and complex applicable materials like colloids, polymers, liquid crystals, biomaterials etc. [1]

Clays belong to the earth, however most of their characteristics are due to interactions with water and air. Clay minerals constitute the fine grain side of geology, and originally in the 19th century it was defined as minerals of grain size  $< 2\mu m$  [2]. Of the minerals classified with respect to grain size, several also exhibit a common mineral structure; clays, in particular, belong to the group called *phyllosilicates* due to the intrinsic layer structure typically described by high *aspect ratio*.<sup>1</sup>

Clays are on one hand regarded as *aquous suspensions of physical colloids*, where platelike layer silicates constitute the primary particles. Thus clays must be included in the physics of hard colloid suspensions. On the other hand, dehydrated clays are described in terms of *intercalation compounds*. Thereby the study of clays in relation to 'nano sandwiches' is of fundamental importance [1].

---

<sup>1</sup>Which means that the layer length and width dimensions are substancially larger compared to the thickness.

### 1.1.1 General considerations

The fundamental building block of all clays is a layered silicate (silicon tetroxide,  $\text{SiO}_4$ ) mesostructure.<sup>2</sup> There are two fundamental *layer*<sup>3</sup> types; *tetrahedral*, where generally a silicon (Si) atom is tetrahedrally bound to four oxygen (O) atoms, and *octahedral*, where generally aluminium (Al) or magnesium (Mg) are octahedrally bound to six oxygen atoms or hydroxyls ( $\text{OH}^-$ ). A *platelet* is composed of different associations of these two layer types, whereas a clay *crystallite* is subsequently an association of identical platelets.

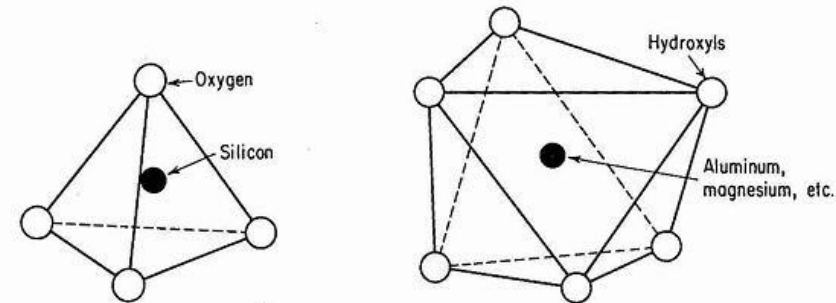


Figure 1.1: Schematic diagram showing a single silicate tetrahedron to the left and a single aluminium or magnesium tetrahedral unit to the right. Taken from [3].

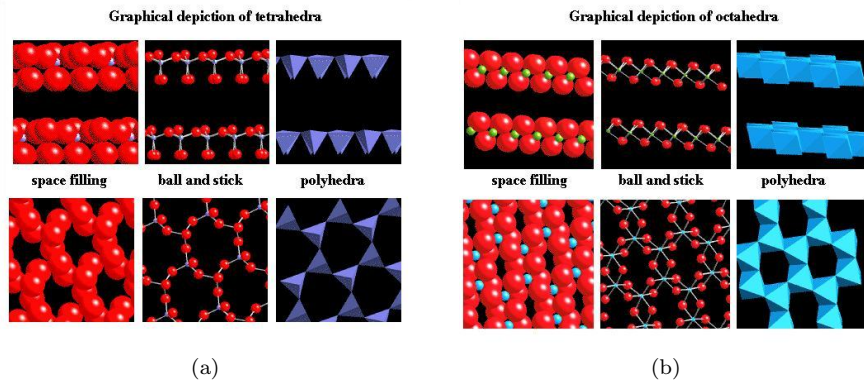


Figure 1.2: Different views of tetrahedral and octahedral layers. The top three illustrate a sideview using three different motifs (space-filling spheres, ball and sticks and polyhedra). The bottom row shows a top view perspective. Taken from [4]. (a) Tetrahedral layer made up of single tetrahedral units. (b) Octahedral layer made up of single octahedral units.

**Clay subgroups** Clays and clay-intercalation compounds (CICs) (see below) can be divided into subgroups according to the underlying structure and layer charge; 1) 1:1 layered, 2) 2:1 layered and 3) 2:1 + 1 layered. A variety of different

<sup>2</sup>The prefix *meso* signifies 'middle', which alludes to the layers being middle structural composites of the total particle structure.

<sup>3</sup>The term *sheet* is often used instead of layer.

species of clays arises through substitutions of cations of the same or different charges in the tetrahedral and octahedral sites.

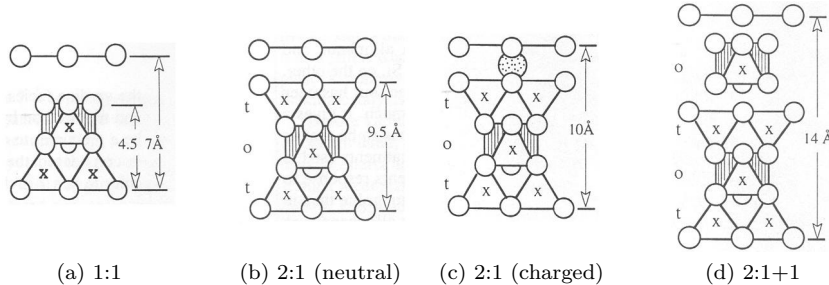


Figure 1.3: Schematic diagrams of different platelet compositions.  $x$  is a cation site.  $t$  and  $o$  stand for tetrahedral and octahedral layers respectively. All pictures taken from [5]. (a) Schematic diagram of the 1:1 layer, which usually has no layer charge or very small layer charge. (b) Schematic diagram of the 2:1 layer with 0 layer charge. (c) Schematic diagram of the 2:1 layer with interlayer cation. (d) Schematic diagram of the 2:1+1 layer. The interlayer octahedral sheet is positively charged.

**Layer structure** The versatility of clays is attributable to the layered microstructure and platelet morphology. The individual particles are made up of one or more silicate lamellae or sheets stacked by sharing exchangeable interlayer cations. Although the layered subunits are crystalline, the relative positioning and orientations between the lamellae usually display a substantial degree of disorder [6]. The layered particles can become relatively thick, and according to [7] they constitute the class of the most rigid layered solid crystals.<sup>4</sup>

As a result of the high rigidity and the structural anisotropy, clays are in possession of several interesting characteristics of both fundamental as well as practical interest. Furthermore it supplies the material science with an arena of low-dimensional (2D) physics.

When a tetraheder- and an octaheder form the surface of adjacent platelets (as in 1:1 or 2:1+1 type minerals), a force is created due to the hydrogen bonding between the oxygen atom associated to the tetrahedrally arranged cation and the hydroxyl ion associated to the octaheder group. This force ensures as stable crystal.

However, when two tetraheder layers constitute the surfaces of adjacent platelets, as in the case of 2:1 type clays, there are no hydrogen atoms present to create these bounds, and the sheets are kept together by electrostatic forces acting between the platelets due to their the electrical charge [2]. For some clay minerals (the so-called *high-charge structures*<sup>5</sup>) this force is strong as a result of the presence of a multitude of interlayer ions, while in other (denoted

<sup>4</sup>Layered silicate clays and clay-intercalation-compounds (CICs) constitute a subgroup of the general class of layered solids, including i.e. graphite intercalation compound (GICs), layered perovskites and layered dichalcogenides. These are classified by Solin by the rigidity of the host layers against transversal displacements perpendicular to the layer planes.[8]

<sup>5</sup>These minerals hold high charge substitutions, between 0.9 and 1.0 per unit cell [9]. The bonding connecting the sheets is very tight.

*low-charge structures*<sup>6</sup>) the layers may expand further due to interlayer influx of water and/or other polar ions and molecules hence increasing the basal distance.<sup>7</sup>

**Pores** One can, in the case of a powder sample, imagine pore sizes of different length scales; 1) the ability to intercalate guest ions and molecules counts for a *nano*porous material with sub 10nm pores between platelets, where the sheet separation can be controlled to a certain degree, 2) *mesopores* of intermediate (micrometer) order originating in the air space between the adjacent particles and 3) 'human inferred' *macropores* due to packing effects.<sup>8</sup>

Clays have, among other materials as e.g. carbon fibres and ceramic membranes, been shown to contain oriented pores in the meso-range [10].

In a clay that undergoes a change in volume by swelling or shrinking, porosity is altered because of changes in clay volume.

See also 1.3.

**Intercalation and swelling** As what is typical for layered solids, clays easily form intercalation compounds in which several guest substances may be inserted into the interlayer spacing in such a way that the host layer itself remains fairly unchanged. However, the number and the form of the guest intercalates successfully inserted greatly exceeds the other types of layered solids [8].

Water is attracted to the clay surfaces, thus creating a water reservoir for its surroundings. The attraction of water molecules to the grain surfaces is called *adsorption*, while *absorption* is the term for describing the incorporation of watermolecules into the crystalline- or grain structure (Figure 1.4). All clays adsorb, though not necessarily absorb. Whether or not a clay mineral undergoes swelling depends on the layer charge and the contributing Coulomb interaction between guest cations and host layer [11].

As a result of mainly two aspects, small grain size and the crystallographic, layered habit with its intercalation features, clays display a high surface to mass ratio.<sup>9</sup> Substitution of metals either in-plane or of the exchangeable interlayer cations create a residual surface charge<sup>10</sup> that in the case of some clay subgroups affects the water absorption in the interlayer space,<sup>11</sup> thereby controlling the basal spacing [12]. These water layers are loosely structured, however considerable effort is needed for the water to leave the surface, either by increasing the temperature and/or pressure [9].

---

<sup>6</sup>These minerals hold low charge substitutions, between 0.2 and 0.9 per unit cell. Hence the bonding is not as tight, and polar molecules, as water, are allowed between the layers, thus enabling the swelling ability[9].

<sup>7</sup>These clays can not strictly be considered as crystals because of the *varying* basal distance. However, the denotation is still used for reasons of simplicity.

<sup>8</sup>In this experiment we inter alia wish to determine the effect of nanopores on diffusion through the mesoporous space. The macropores are results of bad sample preparations, which effects we intend to eliminate through proper grinding and filtering.

<sup>9</sup>For swelling-clays (see 1.1.2) the *specific surface area* (surface per mass) can reach up to 800m<sup>2</sup> per gram.

<sup>10</sup>The platelet inhibits a negative surface charge and a smaller positive edge charge.

<sup>11</sup>The water is absorbed in layers, possibly up till as many as four depending on the surrounding conditions.

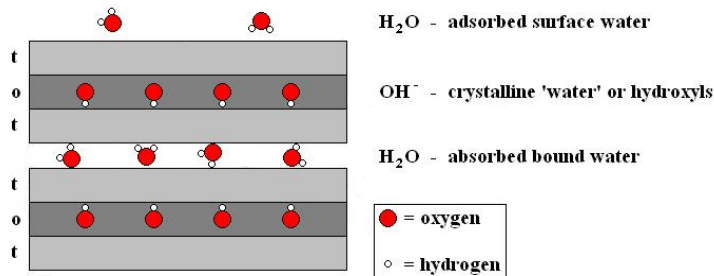


Figure 1.4: Location of type of water in a clay mineral; adsorbed water on the grain surface, absorbed water in the interlayer spacing and crystalline in-plane water (or hydroxyls). *t* and *o* refer to tetrahedral and octahedral layers respectively.

The ability to adsorb/absorb water is possibly the most important characteristics of clays; hence they are classified as swelling or non-swelling [9], the latter being a feature exclusively exhibited by some clays (among them *smectites*) resulting in considerable volume variations.

Thus there are two types of water inside clays: 1) *crystalline* water bound in the internal structure as hydroxyls ( $\text{OH}^-$ ) and 2) *absorbed* water in the interlayer spacings in the form of  $\text{H}_2\text{O}$ . The former contribution is lost at temperatures above  $\sim 500^\circ\text{C}$ , whereas the latter at temperatures prior to  $\sim 120^\circ\text{C}$ .

A hydrated system is a complex system; the detailed interactions between the interlayer cations, the coordinated water molecules and charged silicate surface lead to static structural characteristics og hydration dynamics that are not yet fully understood [7].

### 1.1.2 Smectite clays

Among the clay families the 2:1 layered silicates are the ones most frequently studied due to their wide span of chemical composure, intercalation availabilites of water and other polar ions and molecules, and the characteristics of swelling and undergo pillaring [11]. Thus their area of application is enormous. 2:1-clays are, with respect to the layer charge per unit cell, divided into *talc-phyrophyllite*, *smectites*, *vermiculites* and finally *micas* and *brittle-micas*, each type differentiated by type and location of cations in the oxygen framework [11].

Smectite is the name for the group of minerals all of which display the property of being able to expand and contract their structures while maintaining a two-dimensional crystallographic integrity [5]. The layer charge is sufficiently high for the individual platelets to be able to stack by sharing cations, and at the same time moderate enough to allow further intercalation of water molecules into the resulting "decks of cards"-like smectite particles (Figure 1.9c)[14]. The silicate sheets of 2:1 smectites are generally composed of three atomic layers; one octahedral metal hydroxid layer sandwiched in between two identical silicon tetrahedral layers. Thus each platelet is  $\sim 1\text{nm}$  thick, and the charge per unit cell varies between  $0.4 - 1.2e/\text{unit cell}$ . The thickness of each clay crystallite is typically  $\sim 0.1\mu\text{m}$ , corresponding to  $\sim 100$  stacked platelets [15].

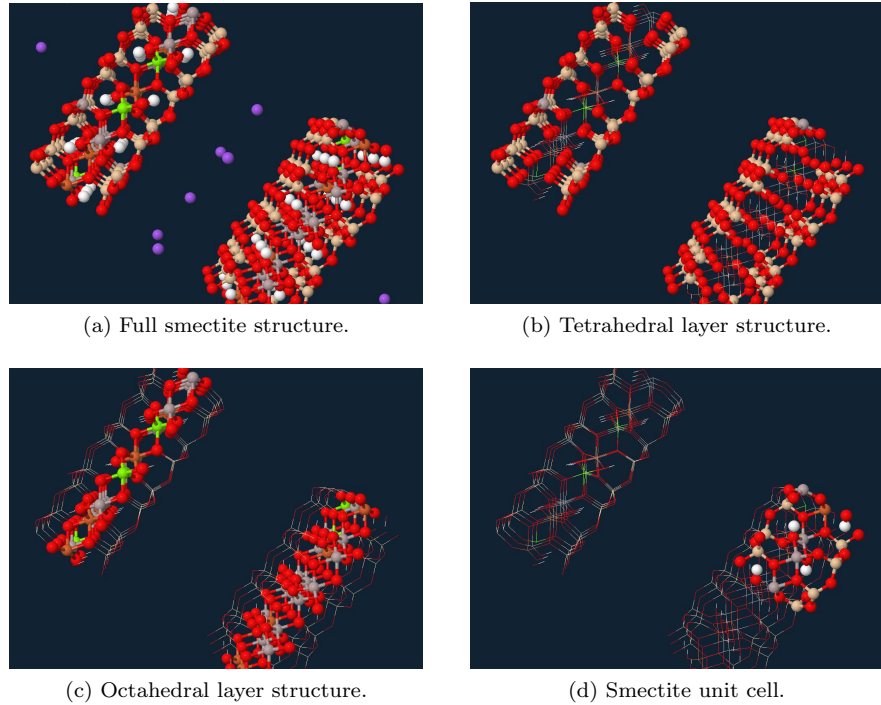


Figure 1.5: Schematic ball and stick diagrams of a smectite clay mineral structure. Though the model is not Na-FH (The model has the composition of a soil smectite derived from the Webster soil series in south central Minnesota. Its structure is based on the muscovite structure of Collins and Catlow (1992) with cation substitutions to accommodate differences in chemistry and changing in spacing between the 2:1 layers. The structure shown is based on a 14 Ångström c-spacing.), it resembles that of Na-FH from a structural point of view. The following symbolism is prevailing: light grey = silicon, red = oxygen, dark grey = aluminium, brown = iron, green = magnesium, purple = sodium, white = hydrogen. Taken from [13]

**Water intercalation** The low layer charge implies two important characteristics; first the interlayer cations are not fixed stably between the layers, and secondly the incorporation of polar ions and molecules. The cations are hydrated (Figure 1.6) as a function of conditions of relative humidity (RH)<sup>12</sup> and temperatures under  $\sim 120^\circ\text{C}$ . Depending on the chemical characteristics of the cation, the ion will generally be hydrated with three or six water molecules. The three molecule situation gives the one water layer (1WL) structure with a general increase of the basal distance of roughly  $\sim 2.5\text{\AA}$ , whereas the six molecule situation results in a two water layer (2WL) structure with an increase of the basal distance of additional  $\sim 2.5\text{\AA}$  [9].<sup>13</sup> Different substitutional cations in their hydrated states display small dimensional variations; monovalent cations

<sup>12</sup>The reason for this is that in humid air the number of achieved hydrates relies on the balance between the concentration of water molecules in the humid air and on the basal surfaces of the crystallites as well as between the hydration levels of the basal surfaces and the interlamellar space [16].

<sup>13</sup>The zero water layer (0WL) situation generally corresponds to a basal distance of roughly  $\sim 10\text{\AA}$

normally involve smaller basal distances than twovalent cations.

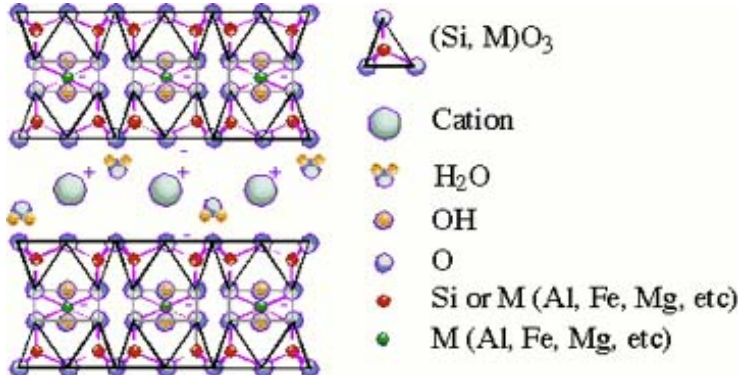


Figure 1.6: Generic structure of smectite with different hydration states coordinated with the intercalation cation found in smectites. Taken from [17]

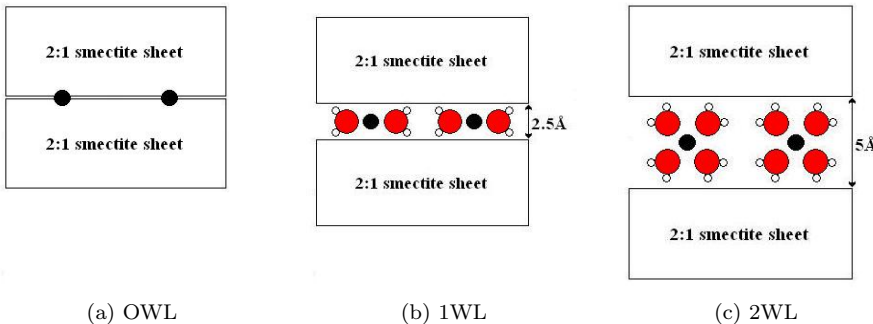


Figure 1.7: Different hydration states for some smectite mineral structures. (a) Dry clay mineral. (b) One monolayer of water. (c) Two monolayers of water.

If the smectite minerals are exposed to other polar ions (liquid or vapor), these molecules will often enter the interlayer and surround the cation-water-complex, thus expanding the interlayer distance additionally. In systems of only water present, the amount of bounded water molecules is a function of both humidity and temperature. Monovalent cations will often easier release water than divalent cations.

**Offset** The linking of tetraheders and octaheders is barely offset with respect to the adjacent oxygen layers, implying that the octahedral cations are not directly under the tetrahedral cations (Figure 1.8). The mineral structures are thereby not orthogonal in all directions, but *monoclinic*. Hence the direction perpendicular to the layer is not  $c$  (one of the unit cell dimensions), but  $c \sin \gamma$  where  $\gamma$  is the monoclinic angle. There will however not be the same regularity in the atomic configurations in the  $a$  and  $b$  crystallographic directions as the offset is placing the different ions in more specific crystallographic sites. The main result from this geometrical offset is that the dominating X-ray crystallographic direction is (001) where a multitude of atoms are adjusted to form basal planes.

Meanwhile, the other primary reflections, as (010) or (100), include fewer atoms and do not display the same strong diffraction.

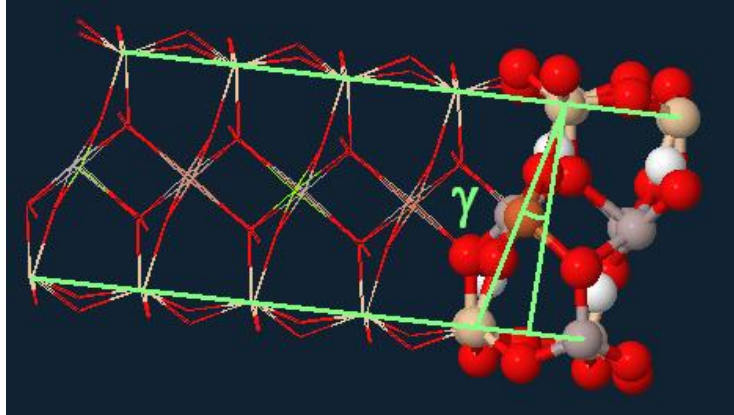


Figure 1.8: Schematic figure of the smectite unit cell in perspective and the subsequent offset, which is general for all clay minerals. The parallel green lines coincide with the crystallographic *ab*-plane. Observe that the octahedral ion does not fall directly below the tetrahedral ion in the layers, thus the mineral structure is not orthogonal in all directions. However, the offset defines the clay mineral as monoclinic. The monoclinic angle *gamma*, defined by this offset, is depicted in the figure. Modified from [13]

The (001) repetitive distance is the distance between equivalent layers of *basal oxygen atoms* (those constituting the basal surface of the tetrahedrally interwoven oxygen matrix) in the clay structure, and this is equal to the basal distance  $c \sin \gamma$ .<sup>14</sup>

**Cavity** The tetraheders in the same layer are bound such that a cavity of diameter  $\sim 3\text{\AA}$  is formed inside the hexagonal ring (forming a *kagomè lattice* [8]) of interlinked oxygen atoms constituting the basal sheet surface against the interlayer gallery space. Cation substitutions in the intralayer structure may bring a charge unbalance upon the sheet. However, this may be compensated for by inserting cations into the cavities of the basal oxygen matrix. Thus charge balance is effectuated on the complete structure (i.e. the two adjacent layers).<sup>15</sup> In this way the two dimensional sheets are stacked in a regular manner to form a three dimensional (pseudo-)crystal, each sheet effectively held together by cations attracted to the cavities.

An ideal hexagonal oxygen matrix is rare in phyllosilicates at normal surface conditions ( $22^\circ\text{C}, 1\text{atm}$ ). The cavity tends to be deformed into a ditrigonal (or pseudo-hexagonal) shape mainly accentuated by the different species of tetrahedral cations and to a lesser extent the other intralayer ions present [9].<sup>16</sup>

<sup>14</sup>This is the physical constant used to characterize clays due to the difficulties in measuring the monoclinic angle  $\gamma$ .

<sup>15</sup>It should be noted that alternative crystal theories exist suggesting proton exchange as responsible for the interlayer cation characteristics of the mineral.

<sup>16</sup>If the tetrahedral and octahedral layers were free (isolated), the interlayers of oxygen would possess different in-plane lattice parameters. The fusion of these two layers introduces a strain, which is reduced and compensated for by correlated corrections (rotations) of the

This deformation may affect the attraction of certain cations for this specific crystallographic site.

**Morphology** Smectite particles have a peculiar shape and appear in networks that make identification of individual members and definition of shape and form difficult. Effective dispersion breaks up the networks and lead to partial lamellae separation. Determination of the size distribution of a smectite is therefore mainly a question of clay sample preparation.

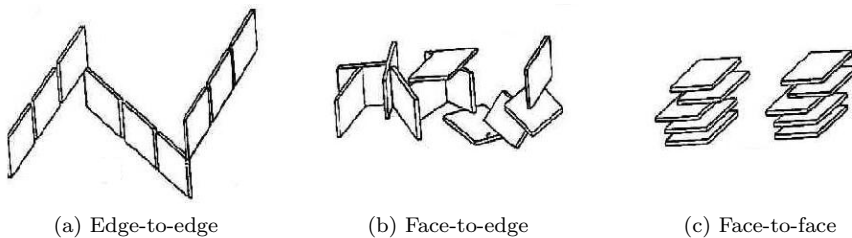


Figure 1.9: Possible structures generated from the 1nm thick platelet of a swelling clay. Taken from [18] (a) Chain structure (b) Like a house of cards (c) Like decks of cards

**Cation exchange capacity** The lattice charge deficit leads to absorption and exchange of ions and organic and inorganic molecules (Figure 1.10). This is apparent from the *cation exchange capacity* (CEC) of the smectites. Under a set of given circumstances different cations are not equally replaceable and do not show the same replacing power [16].<sup>17</sup>

**Standard unit cell** Following the above reasoning the standard smectite *unit cell* is composed of an octahedral layer sandwiched in between two identical tetrahedral layers with the following composites: 20 oxygen atoms and 4 hydroxyl groups together with 8 tetrahedral- and 6 octahedral sites and 4 cavities surrounded by a sixnumbered oxygen ring on the surface.

**Subgroups** Differentiated by the type and proportion of tetrahedral- and/or octahedral elements, smectites are divided into *montmorillonites*, *beidellites*, *nontronites*, *hectorites* and *saponites* [16].

tetraheder around the *c*-axis of the crystal.[8]

<sup>17</sup>The exchange-equilibrium equations leads to the *Gapon equation*, which determines the proportion of each replaceable cation to the total CEC as the outside concentration varies:

$$\frac{M_e^{+m}}{N_e^{+n}} = K \frac{[M_o^{+m}]^{1/m}}{[M_o^{+n}]^{1/n}}$$

where the subscripts *m* and *b* refers to the valence of the cations, *e* and *b* refers to the exchangeable and bulk solution ions and *K* is a function of specific cation adsorption and nature of the clay surface [16].

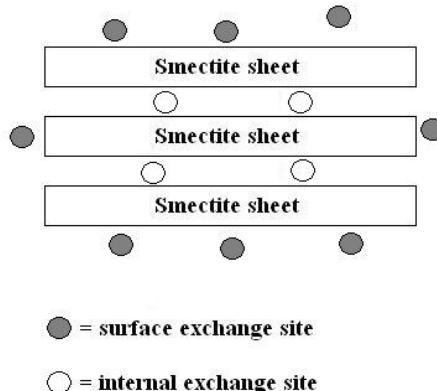


Figure 1.10: Different types of exchange sites on clay particles; surface and absorbed interlayer sites. These sites are quite similar to the sites of adsorbed and absorbed water on swelling clays (Figure 1.4).

### 1.1.3 Hectorite

Hectorites are composed of silicon tetrahedrals ( $\text{SiO}_4$ ) and octahedrals of hydroxyls and magnesium(Mg)- and lithium(Li)-ions. According to [19] the clay mineral originates from altered volcanic tuff ash with a high silicate content related to hot spring activity. The name relates to its locality; Hector, California. The mineral structure is monoclinic, and the chemical formulae is  $\text{Na}_{0.3}(\text{Mg}, \text{Li})_3\text{Si}_4\text{O}_{10}\text{OH}_2$  per half unit cell.

### 1.1.4 Na-fluorohectorite

Na-fluorohectorite (Na-FH) is a synthetic clean chemistry customized clay mineral where the hydroxyls of 'normal' hectorites have been substituted with fluorine ions ( $\text{F}^-$ ). This entails the following chemical formulae of



where  $x$  is the proportion of Li-ions per half unit cell [7].

Na-FH has a rather large surface charge of  $1.2e/\text{unit cell}$ , originating from the substitution of  $\text{Li}^+$  with  $\text{Mg}^{2+}$  in the octahedral layer,<sup>18</sup> compared to other synthetic smectites as for example laptonite ( $0.4e/\text{unit cell}$ ) or montmorillonite ( $0.6e/\text{unit cell}$ ). It also inhibits a fairly large and variable particle size ranging from a few nm up til  $\sim 10\mu\text{m}$  in diameter,<sup>19</sup> and it is expected to display a more homogenous composition and charge distribution compared to natural occurring clays [6, 15].

Wide Angle X-ray scattering (WAXS) studies of fluorohectorite in water suspensions show that fluorohectorite particles contain about  $80\text{ }1\text{nm}$  thick platelets. Because of the large surface charge ( $1.2e/\text{unit cell}$ ), the particles remain

<sup>18</sup>This clay mineral is classified as *trioctahedral* due to that the octahedral layer sites are still fully occupied (as opposed to a *dioctahedral* configuration and two threevalent octahedral cations).

<sup>19</sup>The polydispersity in particle size makes gravity effectively sort the water solvent particles according to size (see [6]).

intact when suspended in water, as opposed to for instance montmorillonite [14]. Other literature ([10, 15]) show particles of an average of  $\sim 100$  platelets, corresponding to a height of  $\sim 0.1\mu m$ . This implies that even though the individual platelets are stacked in high numbers, the resulting 'grain' will be a thin desk with a diameter to height ratio of closer to 100 : 1 in certain occasions. However, due to the already mentioned polydispersity in lateral size this ratio is by no mean fixed and may be considerably lower for other grains.

AFM photographs of Na-FH are shown in Figure 1.11a, Figure 1.11b and Figure 1.11c.

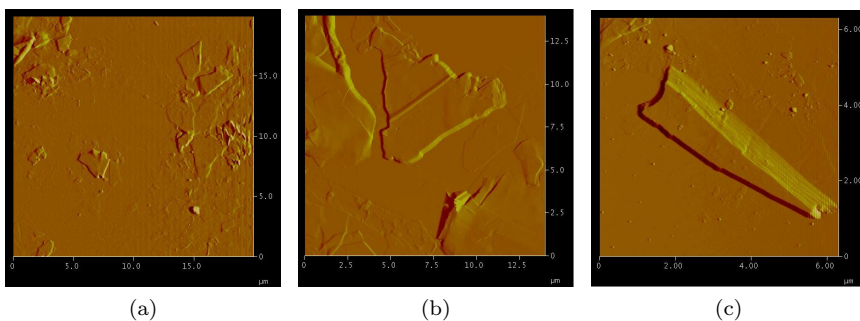


Figure 1.11: Atomic Force Microscope (AFM) photographs of Na-fluorohectorite. With the permission of Dr. Ahmed Gmira (Norwegian University of Science and Technology - NTNU).

**Water intercalation** Water intercalates under the right conditions into the interlayer spacing of Na-FH leading to subsequent swelling. For Na-FH this intercalation process, which is controlled by relative humidity (RH) and temperature, yields three stable hydration states.<sup>20</sup> These structures, normally referred to as *0 water layer* (OWL), *1 water layer* (1WL) and *2 water layers* (2WL), are quite well ordered along the stacking direction. The basal distance between the stacked platelets is around 10 $\text{\AA}$ , 12 $\text{\AA}$  and 15 $\text{\AA}$  for the 0WL, 1WL and 2WL cases respectively [7].

Whereas the number of monolayers able to intercalate is well mapped for hydration and dehydration by synchrotron X-ray diffraction techniques, the spatial configuration of the intercalated water molecules with respect to the silicate sheets and the intercalated cations are not yet fully known [14].

## 1.2 X-ray diffraction (XRD)

Materials are essential to our technological society. In order to understand the properties of these materials and to improve them, different means of diffraction techniques using neutrons from nuclear reactors or particle accelerators or X-rays from X-ray tubes, rotating anodes and synchrotrons have been developed.

<sup>20</sup>The high surface charge prevents further water intercalation and subsequent increase in basal distance. Also the Pauling radius of the intercalation cation is assumed to be an important contributing factor for explaining this limitation of crystalline swelling [20].

Since 1895 and the discovery of X-rays by *William Röntgen* plus the discovery of X-ray diffraction by *Max Theodor Felix von Laue* in the year 1912, this span of electromagnetic radiation has been established as an invaluable method to probe the structure of matter. The application's main limitation has primarily been the generating source, but since the mid 1970s more powerful synchrotron sources have been developed leading to more advanced research on matter.

There are three main processes of interaction of X-rays with matter; elastic scattering, inelastic scattering and X-ray absorption. Using X-rays in the range of approximately wavelength of  $1\text{\AA}$ , small angle scattering can be treated as elastic coherent scattering [21].

X-rays are scattered by electrons around the nuclei of the atoms composing the unit cell. However this scattering is modified in three ways: (i) by the electron distribution of an atom, (ii) by thermal vibrations that tend to blur the atoms as scattering centers as temperature increases and (iii) by atomic arrangements within the unit cell. The purpose of this section is to investigate these effects on the total scattering intensity applied to a layered clay.

### 1.2.1 Diffraction

About 95% of all solid materials can be described as crystalline [22]. When X-rays interact with a crystalline substance, one gets a diffraction pattern. X-ray diffraction (XRD) is the instrumentation most commonly used to study clay-sized minerals [5], though there are several other methods available.

Diffraction is a particular type of wave interference caused by partial obstruction or lateral restriction of a wave. The origin of this process is a periodically set of identical scatterers, whereas this structure may appear in form of one, two or three dimensional lattices. In principle the entire electromagnetic range can be utilized as the source beam, but the essential for diffraction is that the distance between the scattering centers must be of the same order as the wavelength of the waves being scattered.<sup>21</sup>

The interlayer spacing in a typical clay crystal and the wavelength of the X-rays both is of the order  $\text{\AA}$  (or 0.1 nm).

Also, since the crystalline arrangement is studied with detectors some centimetres away from the scatterers (atomic electrons), and the wavelength as well as the interatomic distance are in the order of 0.1 nm, the observed intensity may be dealt with in the plane wave approximation.

#### Thomson scattering

X-rays are electromagnetic radiation that best can be described as a polarized wave with an oscillatory electrical field,  $\vec{E}$ , and an oscillatory magnetic field,  $\vec{H}$ , mutually perpendicular as well as perpendicular on the direction of propagation.

In a *classical* description of a scattering event the electromagnetic field, when it encounters an electron, inflicts the electron with an equal frequency (the electron absorbs a tiny amount of energy from the incoming beam), which

---

<sup>21</sup>This is due to the *Laue condition* which states that the momentum transfer  $\vec{Q}$  caused by a scattering event must coincide with a reciprocal lattice vector  $\vec{G}_{hkl}$  in order for constructive interference to occur[23, chapter 4.4.1]

thereby reradiates this energy with the same wavelength in all directions due to its vibration. This is called *coherent scattering*, and the radiation is said to be *elastic*. Such scattering is also called Thomson scattering.

Quantum mechanically when a photon is scattered against electrons in the matter, a tiny amount of the incoming particle's linear momentum (or energy) is transferred to the electrons, but this loss in energy (or linear momentum) is so small that the energy and thus the wavelength is assumed to be conserved.

### Compton scattering

Energy may also be transferred to the electron with the result that the scattered photon has a lower frequency (or energy) to that of the incident one. Such an *inelastic* scattering process is called Compton scattering.

Elastic X-ray scattering is however the main process that is exploited in the investigation of the structure of materials, and in this case it mostly suffices to adopt a classical approach.

### 1.2.2 Interference

When waves are scattered from different scatterers, a phase difference originates due to the differences in optical path distance travelled. When two or more rays are in phase there is constructive interference, whereas destructive interference is caused by rays out of phase.

A diffracted beam that can be observed and measured is a beam composed of an enormous number of constructively interfering rays thereby mutually reinforcing one another [5]. For this condition to be achieved, the angle of incident can only take on certain discrete values most easily determined by Bragg's law (see 1.2.3 below).

### 1.2.3 Bragg's law of diffraction

The Laue condition,  $\vec{Q} = \vec{G}_{hkl}$ , for a scattering peak is identical to the condition for constructive interference of waves reflected from  $hkl$  planes. The incident and the scattered beam vectors are equal in magnitude and make equal angles with the  $hkl$  plane. Their difference is the momentum transfer vector,  $\vec{Q}$ , perpendicular to this very plane.

For two waves incident with an angle  $\theta$  on two parallel planes of interplanar distance  $d$ , the reflected waves interfere constructively provided that the difference in optical path travelled is a multiple of the wavelength<sup>22</sup>  $\lambda$ .

$$2d_{hkl} \sin \theta = n\lambda \quad (1.2)$$

where  $n$  is an integer. This equation is known as the *Bragg law* and was first worked out by *W.L. Bragg* in 1912. For reflections from other sets of  $hkl$ ,

---

<sup>22</sup>Some simplifying assumptions have to be taken into account in order to derive Bragg's law: the incident beam is assumed to be perfectly monochromatic as well as perfectly collimated, and secondly the equation is based on having only three planes of perfectly ordered atoms in a infinite perfect crystal with the exact orientation for diffraction to occur [5].

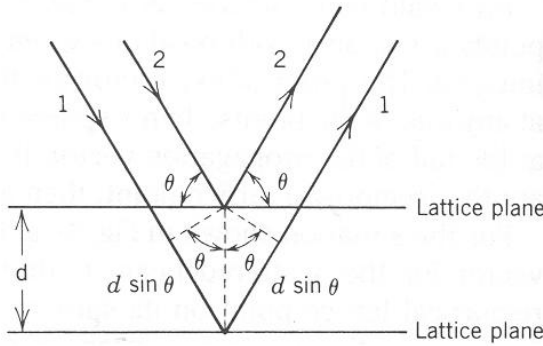


Figure 1.12: Scattering from two parallel planes. For constructive interference to occur the difference in optical path travelled by the two waves must equal a multiplum of the wavelength. Taken from [24].

constructive interference may also be reached provided that this condition is met.<sup>23</sup>

Note that Bragg's law is purely a simple geometrical interpretation of diffraction by a crystal grating in contrast to the Laue condition that is based on a pure physical platform. When a beam of X-rays is reflected in the Bragg sense from an extended crystal face, the phenomenon is not a surface reflection as with ordinary light. The X-rays penetrates to a depth of several million layers of the effectively infinite series of equispaced atomic planes before being appreciable absorbed. At each atomic plane only a minute portion of the beam may be considered to be reflected. Moreover, though the Bragg condition predicts the angular dependency on peak intensity, it does not enable us to calculate the numerical value of scattering intensity of constructive interference.

#### 1.2.4 From one electron to a complete lattice

In order to evaluate the integrated intensity of a Bragg reflection from a small crystal, which is the quantity that is readily determined in an experiment, it is required to know exactly how this integrated intensity is to be measured. Instead of referring to the intensity one can more precisely adapt the differential cross-section. Consequently in this section the differential cross-section for Thomson scattering from one electron to a whole lattice will be deducted very briefly [5, 7, 24, 23, 25, 26].

The differential cross-section is in fact a proportionality factor defined by (per scatterer)

$$\left( \frac{d\sigma}{d\Omega} \right) = \frac{I_{sc}}{I_0 N \Delta\Omega} \quad (1.3)$$

where  $I_0$  is the number of photons per second incident on the sample,  $I_{sc}$  is the number of photons scattered per second into a detector that spans a solid angle  $\Delta\Omega$  and  $N$  is the number of scatterers.

<sup>23</sup>The Bragg condition very well enlightens the limitations of wavelengths used in structure analysis. The Bragg condition clearly states that no intensisty peaks can occur if  $\lambda$  is larger than twice the largest crystal plane separation.

### One electron

The elementary scattering unit of an X-ray in material is the electron. The differential cross-section for an atom is

$$\left( \frac{d\sigma}{d\Omega} \right) = r_0^2 P \quad (1.4)$$

24

where  $r_0$  is the Thomson scattering length which expresses the ability of an electron to scatter an X-ray, and  $P$  is the polarization factor

$$P = \begin{cases} 1 & \text{synchrotron: vertical scattering plane} \\ \cos^2 \psi & \text{synchrotron: horizontal scattering plane} \\ \frac{1}{2} (1 + \cos^2 \psi) & \text{unpolarized source} \end{cases} \quad (1.5)$$

where  $\psi$  is the direction of the radiated field with respect to the direction of the incident beam.<sup>25</sup>

### One atom

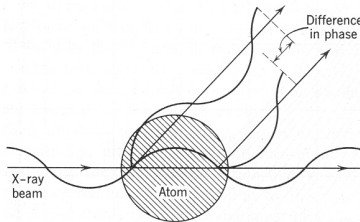


Figure 1.13: Phase difference in scattering from different parts of an atom. Taken from [26].

The total scattering length of an atom is given

$$-r_0 f^0(\vec{Q}) = -r_0 \int \rho(\vec{r}) e^{i\vec{Q}\cdot\vec{r}} d\vec{r} \quad (1.6)$$

with *atomic form factor* or *atomic scattering factor*

$$f^0(\vec{Q}) = \int \rho(\vec{r}) e^{i\vec{Q}\cdot\vec{r}} d\vec{r} \quad (1.7)$$

resulting from the contribution of the charge density  $\rho(\vec{r})$  in a volume element  $d\vec{r}$  in  $\vec{r}$  to the scattered field introducing a phase factor  $e^{i\vec{Q}\cdot\vec{r}}$ , where  $\vec{Q}$  is the wavevector or momentum transfer.<sup>26</sup>

<sup>24</sup>The power of two arises from the fact that the intensity is proportional to the squared amplitude of the electric field, which in itself is proportional to the Thomson scattering length. The latter is by convention the prefactor of the spherical wave reradiated from the oscillating electron set in motion by the incoming field

$$\frac{E_{\text{rad}}(r, t)}{E_{\text{in}}} = r_0 \frac{e^{ikR}}{R} \cos \psi$$

where  $R$  is the distance from the electron and  $\psi$  the angle with respect to the direction of the incident beam.

<sup>25</sup>In our case  $\Psi \equiv 2\theta$  as will be seen later.

<sup>26</sup>Atomic electrons are necessarily governed by quantum mechanics and have discrete energy

### One molecule

Indexing the different atoms in the molecule by label  $j$ , the molecular structure factor may be written

$$F^{\text{molecule}}(\vec{\mathbf{Q}}) = \sum_{\vec{\mathbf{r}}_j} f_j(\vec{\mathbf{Q}}) e^{i\vec{\mathbf{Q}} \cdot \vec{\mathbf{r}}_j} \quad (1.9)$$

<sup>27</sup> Due to the different spatial locations of the electrons a phase factor was introduced to the atomic form factor in Equation (1.7). Likewise different spatial locations of the atoms in the molecule correspondingly introduce another phase factor,  $e^{i\vec{\mathbf{Q}} \cdot \vec{\mathbf{r}}_j}$ , further complicating the expression of the molecular structure factor.

### A lattice

Following the approach described above and substituting the molecule with the unit cell, the calculation of the lattice structure factor is straightforward

$$F^{\text{crystal}}(\vec{\mathbf{Q}}) = F^{\text{unit cell}}(\vec{\mathbf{Q}}) \cdot S_N(\vec{\mathbf{Q}}) \quad (1.10)$$

$$= \sum_{\vec{\mathbf{r}}_j} f_j(\vec{\mathbf{Q}}) e^{i\vec{\mathbf{Q}} \cdot \vec{\mathbf{r}}_j} \cdot \sum_{\vec{\mathbf{R}}_n} e^{i\vec{\mathbf{Q}} \cdot \vec{\mathbf{R}}_n} \quad (1.11)$$

where  $\vec{\mathbf{R}}_n$  are the lattice vector defining the lattice and  $\vec{\mathbf{r}}_j$  the positions of the atoms with respect to an arbitrary lattice site.

In the subsequent paragraphs the last sum in Equation (1.10), the lattice sum,

$$S_N(\vec{\mathbf{Q}}) = \sum_{\vec{\mathbf{R}}_n} e^{i\vec{\mathbf{Q}} \cdot \vec{\mathbf{R}}_n} \quad (1.12)$$

will be investigated. The lattice points are specified by the lattice vector  $\vec{\mathbf{R}}_n = n_1 \vec{\mathbf{a}}_1 + n_2 \vec{\mathbf{a}}_2 + n_3 \vec{\mathbf{a}}_3$ ; hence in the case of a three dimensional finite lattice with

---

levels. The most tightly bound electrons are in the K-shell, with comparable energy levels to a typical X-ray photon. If the energy of the X-ray photon is significantly smaller than the bonding energy of the K-shell, the response of these electrons to an external driving field will be reduced due to the fact that they are bound. On the other hand, electrons in less tightly bound shells (L, M, etc.) will be able to respond better, but on a whole a reduction of the atomic scattering length, denoted  $f'$  by convention, is to be expected. For energies substantially exceeding the bonding energy, the electrons are to be considered as free and  $f'$  equals zero. In between these limits  $f'$  is expected to display resonant behaviour at energies corresponding to atomic absorption edges.

Apart from altering the real part of the scattering length, the electron is (by analogy with a forced harmonic oscillator) allowed to display a phase lag with respect to the driving field represented by the complex term  $if''$ .

Thus, when scattering is treated in the second order Born approximation, the complete atomic form factor becomes [27]

$$f(\vec{\mathbf{Q}}, \hbar\omega) = f^0(\vec{\mathbf{Q}}) + f'(\hbar\omega) + if''(\hbar\omega) \quad (1.8)$$

which in particular is of importance for wavelengths with energies close to absorption edges of atoms.

<sup>27</sup>To compute the intensity in absolute units, the multiplicative factor of  $-\vec{\mathbf{r}}_0$  has to be accounted for in addition to the structure factor in accordance with Equation (1.6).

$N = (N_1, N_2, N_3)$  unit cells, Equation (1.12) can be written

$$S_N(\vec{\mathbf{Q}}) = \prod_{j=1}^3 \sum_{n_j=0}^{N_j-1} e^{iQ_j n_j |\vec{\mathbf{a}}_j|} \quad (1.13)$$

In order to consider the behaviour of the lattice sum when the Laue condition is almost fulfilled, a small parameter  $\vec{\xi} = (\xi_1, \xi_2, \xi_3)$  is introduced, which implies that

$$\vec{\mathbf{Q}} = \vec{\mathbf{G}}_{hkl} + \vec{\xi} = (h + \xi_1)\vec{\mathbf{a}}_1^* + (k + \xi_2)\vec{\mathbf{a}}_2^* + (l + \xi_3)\vec{\mathbf{a}}_3^*$$

where the momentum transfer  $\vec{\mathbf{Q}}$  is expressed in terms of the Miller indices,  $(hkl)$ , the vector parameter  $\vec{\xi}$  and the basis vectors in reciprocal space,  $\vec{\mathbf{a}}_j^*$  ( $j = 1, 2, 3$ ).

Recognizing the sum in Equation (1.13) as a geometrical series (see page 94), rewriting Equation (1.13) gives

$$S_N(\vec{\xi}) = \prod_{j=1}^3 e^{i\pi\xi_j(N_j-1)} \frac{\sin(N_j\pi\xi_j)}{\sin(\pi\xi_j)} \quad (1.14)$$

Thus for the real value limited to one dimension  $j$  ( $j = 1, 2$  or  $3$ )

$$\begin{aligned} |S_{N_j}(\xi_j)| &= \left| \frac{\sin(N_j\pi\xi_j)}{\sin(\pi\xi_j)} \right| \Big|_{\xi_j \rightarrow 0, N_j \sim \text{large}} \longrightarrow N_j \\ |S_{N_j}(\xi_j = \frac{1}{2N_j})| &\approx \frac{2}{\pi} N_j \approx \frac{1}{2} (\text{Peak Height}) \end{aligned} \quad (1.15)$$

<sup>28</sup> showing that the peak height is equal to  $N_j$  and that the  $j$ 'th full width at half maximum (FWHM) is approximately  $\frac{1}{N_j}$ .

As  $N_j$  gets large and the width narrows and tends to zero while the area remains constant<sup>29</sup>, the lattice sum can be written in terms of a Dirac delta function,  $\delta$ ,<sup>30</sup>

$$|S_{N_j}(\xi_j)| \longrightarrow \delta(\xi_j) \quad (1.16)$$

The lattice sum may be equivalently written<sup>31</sup>

$$|S_N(Q_j)| \longrightarrow |\vec{\mathbf{a}}_j^*| \delta(Q_j) \quad (1.17)$$

According to Equation (1.4) it is the squared structure factor and hence the squared lattice sum that is of interest in a diffraction experiment. By similar

<sup>28</sup>Since  $\sin x \rightarrow x$  for small values of  $x$  and

$$\left| S_{N_j} \left( \xi_j = \frac{1}{2N_j} \right) \right| = \left| \frac{\sin(\frac{\pi}{2})}{\sin(\frac{\pi}{2N_j})} \right| = \left| \frac{1}{\sin(\frac{\pi}{2N_j})} \right| \Big|_{N_j \sim \text{large}} \approx \frac{1}{\frac{\pi}{2N_j}} = \frac{2}{\pi} N_j \approx \frac{1}{2} (\text{Peak Height})$$

<sup>29</sup>While the amplitude and the FWHM are dependent of  $N_j$ , it can be shown that the area and consequently the integrated intensity is equal to unity and thus independent of  $N_j$ .

<sup>30</sup>See Appendix A

<sup>31</sup>The factor  $|\vec{\mathbf{a}}_j^*|$  is the  $j$ 'th one dimensional equivalent to the factor  $v^*$  appearing in the three dimensional transformation of  $\delta(\vec{\xi}_j)$  to  $\delta(\vec{\mathbf{Q}} - \vec{\mathbf{G}})$ :

$$\delta(\vec{\mathbf{Q}} - \vec{\mathbf{G}}) = \delta \left( \sum_{j=1}^3 \xi_j |\vec{\mathbf{a}}_j^*| \right) = \sum_{j=1}^3 \delta(\xi_j |\vec{\mathbf{a}}_j^*|) = \sum_{j=1}^3 \frac{1}{|\vec{\mathbf{a}}_j^*|} \delta(\xi_j) = \frac{1}{v_c^*} \sum_{j=1}^3 \delta(\xi_j) = \frac{1}{v_c^*} \delta(\vec{\xi})$$

argumentations as above, showing that the peak is proportional to  $N_j^2$  and the width inversely proportional to  $N_j$ , whereas the sum  $|S_{N_j}(Q_j)|^2$  still equals unity, the lattice sum can also be written in terms of a delta function

$$|S_N(Q_j)|^2 \longrightarrow |N_j \vec{a}_j^*| \delta(Q_j) \quad (1.18)$$

The generalization to three dimensions is straightforward, and the delta function character will be maintained for any crystal shape provided a large number of unit cells in every direction

$$\left| S_N(\vec{\mathbf{Q}}) \right| \longrightarrow N v_c^* \delta(\vec{\mathbf{Q}} - \vec{\mathbf{G}}) \quad (1.19)$$

where  $N$  is the total number of unit cells and  $v_c^*$  is the volume of a unit cell in reciprocal space.

### 1.2.5 Kinematic scattering

When scattering is considered in a certain sense to be weak, multiple scattering effects are allowed for to be neglected thereby leading to considerable simplifications. This limit is also known as the *kinematical approximation*.

#### Lattice vibrations

So far the lattice considered has been assumed to be perfectly rigid. However, atoms in crystal lattices do vibrate, and this effect will now be investigated.

Vibrations are due to two distinct causes. The first contribution is purely quantum mechanical in origin and attributed to the uncertainty principle. These vibrations are independent of temperature and occur even at absolute zero of temperature. Hence they are known as zero-point fluctuations. The second contribution arises at finite temperatures and is due to thermal excitation of elastic waves (or phonons) in the crystal, thus increasing the amplitude of the vibrations.

To begin with we shall assume scattering from a simple crystal structure in which we find one type of atom located in each lattice site. Vibrational affects are allowed for by writing the instantaneous position of an atom as  $\vec{\mathbf{R}}_n + \vec{\mathbf{u}}_n$ , where  $\vec{\mathbf{R}}_n$  is the time averaged mean position and  $\vec{\mathbf{u}}_n$  is the displacement.

The structure factor is then, according to Equation (1.10) and (1.11),

$$F^{\text{crystal}}(\vec{\mathbf{Q}}) = F^{\text{unit cell}}(\vec{\mathbf{Q}}) \cdot S_N(\vec{\mathbf{Q}}) = \sum_{\vec{\mathbf{r}}_j} f_j(\vec{\mathbf{Q}}) e^{i \vec{\mathbf{Q}} \cdot \vec{\mathbf{r}}_j} \cdot \sum_{\vec{\mathbf{R}}_n} e^{i \vec{\mathbf{Q}} \cdot \vec{\mathbf{R}}_n}$$

From Equation (1.3) and (1.4) we observe that the measured intensity,  $I_{sc}$ , is proportional to the structure factor, hence

$$I_{sc} \propto \langle \left| F^{\text{unit cell}}(\vec{\mathbf{Q}}) \right|^2 \rangle = I_{\text{Debye-Waller}} + I_{\text{TDS}} \quad (1.20)$$

where

$$\begin{aligned} I_{\text{Debye-Waller}} &= \sum_m \sum_n f(\vec{\mathbf{Q}}) e^{-\frac{1}{2} Q^2 \langle u_{Qm}^2 \rangle} e^{i \vec{\mathbf{Q}} \cdot \vec{\mathbf{R}}_m} f^*(\vec{\mathbf{Q}}) e^{-\frac{1}{2} Q^2 \langle u_{Qn}^2 \rangle} e^{-i \vec{\mathbf{Q}} \cdot \vec{\mathbf{R}}_n} \\ I_{\text{TDS}} &= \sum_m \sum_n f(\vec{\mathbf{Q}}) e^{i \vec{\mathbf{Q}} \cdot \vec{\mathbf{R}}_m} f^*(\vec{\mathbf{Q}}) e^{-i \vec{\mathbf{Q}} \cdot \vec{\mathbf{R}}_n} \{ e^{Q^2 \langle u_{Qm} u_{Qn} \rangle} - 1 \} \end{aligned}$$

The first term,  $I_{\text{Debye-Waller}}$ , is recognized as elastic scattering from a lattice with the atomic form factor being replaced by

$$f^{\text{atom}} = f(\vec{\mathbf{Q}})e^{-\frac{1}{2}Q^2\langle u_Q^2 \rangle} \equiv f(\vec{\mathbf{Q}})e^{-W(Q)} \quad (1.21)$$

where  $f(\vec{\mathbf{Q}})$  is the atomic form factor and the exponential term,  $e^{-W(Q)}$ , is known as the *Debye-Waller factor*. Despite that this term contains contributions for large values of  $|\vec{\mathbf{R}}_m - \vec{\mathbf{R}}_n|$ , it still gives rise to a delta function in the scattering. We observe that the intensity of the elastic scattering is reduced in virtue of atomic vibrations, whereas the width does not increase.

As for the second term,  $I_{\text{TDS}}$ , in crystallographic experiments *thermal diffuse scattering* (TDS) gives rise to a background signal which occasionally needs to be subtracted from the data.<sup>32</sup>

The generalization of Equation (1.21) is straightforward

$$F^{\text{unit cell}}(\vec{\mathbf{Q}}) = \sum_{\vec{\mathbf{r}}_j} f_j(\vec{\mathbf{Q}})e^{-W_j(Q)}e^{i\vec{\mathbf{Q}} \cdot \vec{\mathbf{r}}_j} \quad (1.22)$$

where each type of atom in a compound in general will have a different Debye-Waller factor.<sup>33</sup>

The Debye-Waller factor of each atom in a compound will generally differ, as should be expected from the fact that lighter atoms normally vibrate more intensely than heavier ones. Furthermore this factor doesn't need to be isotropic due to the bonding may restrict the vibration along certain directions. For instance the energy required to alter the angle of the bonding is often less compared to changing the length of the same bonding, so that atoms at the end of bondings tend to have a larger amplitude perpendicular to the bonding than along this.

### Measured intensity from a crystallite

Combining the Equations (1.4), (1.11) and (1.19), the differential cross-section for a crystallite, prior to taking the vibrational effects into consideration, can be written

$$\left( \frac{d\sigma}{d\Omega} \right) = r_0^2 P \left| F(\vec{\mathbf{Q}}) \right|^2 N \nu_c^* \delta(\vec{\mathbf{Q}} - \vec{\mathbf{G}}) \quad (1.23)$$

where  $r_0$  is the Thomson scattering length which expresses the ability of an electron to scatter an X-ray,  $P$  is the polarization factor,  $F(\vec{\mathbf{Q}})$  is the unit cell structure factor from Equation (1.22),  $N$  is the number of unit cells,  $\nu_c^*$  is the volume of the unit cell in reciprocal space,  $\vec{\mathbf{Q}}$  is the momentum transfer and  $\vec{\mathbf{G}}$  is a reciprocal lattice vector.

---

<sup>32</sup>The intensity increases as the average mean displacement decreases, and its width is determined by the correlations  $\langle u_{Q_m} u_{Q_n} \rangle$  between the displacements of different atoms.

<sup>33</sup>Given by

$$W_j = \frac{1}{2} Q^2 \langle u_{Q_j}^2 \rangle = \frac{1}{2} \left( \frac{4\pi}{\lambda} \right) \sin^2 \theta \cdot \langle u_{Q_j}^2 \rangle = B_T^j \left( \frac{\sin \theta}{\lambda} \right)^2$$

The incident beam has so far been assumed to be perfectly monochromatic and perfectly collimated, so that the scattered beam is also monochromatic due to its elastic characteristic. However, it will not necessarily be perfectly collimated. As the width of the Bragg peak is inversely related to the number of unit cells,  $N$  (see Equation (1.15)), and as  $N$  is not infinite, the peak has a finite width, thereby implying that the Laue condition doesn't need to be exactly fulfilled in order to record a measurable intensity.

This is illustrated in Figure 1.14. It is assumed that when the momentum transfer  $\vec{Q}$  falls within the grey ellipse,  $\vec{Q}$  is sufficiently close to the reciprocal scattering vector  $\vec{G}_{hkl}$  for an adequate intensity to be achieved, and thus the scattered wave will show some divergence (in  $\vec{k}'$ ). Assuming that every divergent scattered wave reaches the detector, this implies that all scattering processes where  $\vec{k}'$  terminates on the thick red line will be recorded. In order to observe the *sum* of all the scattering processes where  $\vec{Q}$  terminates within the elliptically smeared Bragg peak, the crystallite needs to be rotated with respect to the incoming wave  $\vec{k}$ , and the measurements are correspondingly repeated with the other thin red lines. Thereby the intensity is accumulated.

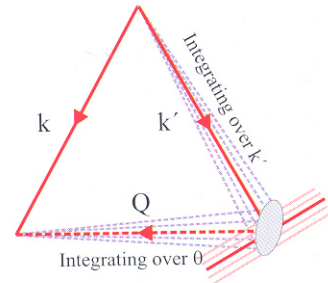


Figure 1.14: The uncollimated scattering from a crystallite is represented by the grey ellipse, which reflects the shape of the crystal in reciprocal space. By varying the orientation of the crystal, scattered waves with different  $\vec{k}'$ -values from terminating on different red lines are scattered into and recorded in the detector, and the resulting accumulated intensity shows a smeared Bragg peak. This arises from that the Laue condition is not absolute. Taken from [23].

### The Lorentz factor

The Lorentz factor is a combination of two geometrical factors; the first a formulation for the volume of the crystal that is exposed to primary irradiation, while the second relates the number of crystals favourably oriented for diffraction at any Bragg angle [5].

Equation (1.23) applies to a single setting of the instrumentations. By the arguments stated in the above subsections, integration over the scattered wave  $\vec{k}'$  and the angular variable  $\theta$ , defined by the incident vector  $\vec{k}$  and the reciprocal vector  $\vec{G}_{hkl}$ , must be allowed for in order to be able to compare this intensity with the measured experimental intensity.

The final result of these steps gives rise to two additional factors<sup>34</sup>

$$\frac{1}{k^3} \frac{1}{\sin 2\theta} \quad (1.24)$$

the last of which is known as the *Lorentz factor*. This factor depends on exactly how the intensity is integrated and therefore directly on the details of the experiment.

The above result implies the following modification of Equation (1.23)

$$\left( \frac{d\sigma}{d\Omega} \right) = r_0^2 P \left| F(\vec{\mathbf{Q}}) \right|^2 N \frac{\lambda^3}{v_c} \frac{1}{\sin 2\theta} \quad (1.25)$$

<sup>35</sup>

### 1.2.6 Powder diffraction

The sample is ground into a large number of small randomly oriented crystals. Imagine a crystal oriented so that a scattering peak occurs at a scattering angle  $\theta$ . Subsequent rotation of the crystal around the direction of the incident wave produces a scattering ring, a so called *Debye-Scherrer ring* of interference, in a detector plane perpendicular to the direction of the incident wave. In the case of powder crystals the crystals are not rotated, but the effect is nevertheless much the same as the scattered waves corresponding to the various orientations are produced *simultaneously*.

A crystalline powder then consists of a multitude of small crystal grains randomly oriented. An *ideal powder sample* implies that the directions of the reciprocal lattice vectors,  $\vec{\mathbf{G}}_{hkl}$ , are isotropically distributed over a sphere in reciprocal space. Given an incident beam defined by  $\vec{\mathbf{k}}$ , a fraction of the crystallites has the correct orientation for Bragg scattering. The reciprocal lattice vectors of these crystallites constitute a circle formed by a cut through the sphere in a plane perpendicular to the incident wave vector; a cut that constitutes the base of the so-called *Debye-Scherrer cone* formed by the scattered wave vectors  $\vec{\mathbf{k}}'$  (see Figure 1.15).

For a given  $(hkl)$ -reflection the fraction of crystal grains favourably orientated for detection is proportional to the circumference of the circle defining the basis of the Debye-Scherrer cone. By geometrical considerations this circumference is given by  $2\pi|\vec{\mathbf{G}}_{hkl}|\cos\theta$ .<sup>36</sup> Moreover, permutations of the Miller indices

---

<sup>34</sup>With the delta function in Equation (1.23) as the starting point,

$$\delta(\vec{\mathbf{Q}} - \vec{\mathbf{G}})$$

variations in  $\vec{\mathbf{k}}'$  and  $\theta$  and integration over  $\vec{\mathbf{k}}'$  yields

$$\int \delta(\vec{\mathbf{Q}} - \vec{\mathbf{G}}) d\vec{\mathbf{k}}' = \frac{2}{k} \delta(G^2 - 2kG \sin \theta)$$

Then integrating over  $\theta$  gives

$$\frac{2}{k} \int \delta(G^2 - 2kG \sin \theta) d\theta = \frac{1}{k^3} \frac{1}{\sin 2\theta}$$

For details confer a textbook, for example [23].

<sup>35</sup>Where  $k = \frac{2\pi}{\lambda}$  and  $v_c^* = \frac{(2\pi)^3}{v_c}$ .

<sup>36</sup>Or  $2\pi k \sin 2\theta$

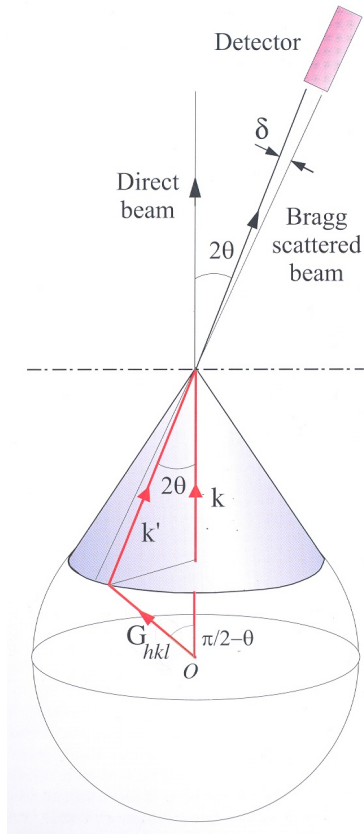


Figure 1.15: For an ideal powder sample, the fraction of the crystallites correctly orientated to the incident beam may be represented by a scattered wave vector evenly distributed on the Debye-Scherrer cone with  $\vec{\mathbf{k}}$  as axis and apex half angle  $2\theta$ . The angular acceptance of the detector is  $\delta$ . Taken from [23].

( $hkl$ ) may yield spheres with the same  $\vec{\mathbf{G}}_{hkl}$  vectors, and this fact is taken into account by introducing the multiplicity  $m_{hkl}$  of the reflections. Consequently for a given  $\vec{\mathbf{G}}_{hkl}$  the intensity is proportional to  $m_{hkl} \cos \theta$ .

At a *different*  $\vec{\mathbf{G}}_{hkl}$  vector the detector will see another fraction of the Debye-Scherrer defined circle. The circumference can be expressed as  $2\pi k \sin 2\theta$  independent of  $\vec{\mathbf{G}}_{hkl}$ , and the fraction seen by the detector with angular acceptance  $\delta$  is  $\frac{k\delta}{2\pi k \sin 2\theta}$ , which is proportional to  $\frac{1}{\sin 2\theta}$ .

Thus two additional factors are introduced to the Lorentz factor of a perfect powder sample

$$L^{\text{perfect powder}} = \frac{1}{\sin 2\theta} \cdot m_{hkl} \cos \theta \frac{1}{\sin 2\theta} = \frac{m_{hkl}}{2 \sin 2\theta \sin \theta} \quad (1.26)$$

### 1.2.7 Putting it all together: The complete differential cross-section for a crystal

Summarizing the key elements in subsections 1.2.4 to 1.2.6, the total differential cross-section can be expressed as

$$\left( \frac{d\sigma}{d\Omega} \right) = r_0^2 P |F(\vec{\mathbf{Q}})|^2 N \frac{\lambda^3}{\nu_c} \frac{m_{hkl}}{2 \sin 2\theta \sin^\beta \theta} \quad (1.27)$$

where each electron in a unit cell has the scattering cross-section  $r_0^2 P$ ; the scattering length  $r_0$  expressing an electron's scattering ability and  $P$  is the

source dependent polarization contribution. The total intensity is reduced in virtue of different optical path distances expressed by the structure factor of the unit cell,  $F(\vec{Q})$  (Equation (1.10) and Equation (1.11)). Differences in optical path distances of the unit cells also introduce a phase factor expressed by the lattice sum, which is reduced to a Dirac's delta function. Summation and proper integrations of this delta function give rise to the last factors  $N \frac{\lambda^3}{v_c} \frac{m_{hkl}}{2 \sin 2\theta \sin \theta}$ , where  $N$  is the number of unit cells,  $\lambda$  the wavelength of the radiation,  $v_c$  the volume of the lattice unit cell and  $\frac{m_{hkl}}{2 \sin 2\theta \sin \theta}$  the Lorentz factor for an ideal powder. The exponent  $\beta$  in the modulated *Lorentz-polarization factor*<sup>37</sup>

$$Lp = \frac{m_{hkl} P(\theta)}{\sin 2\theta \sin^\beta \theta} \quad (1.28)$$

(omitting the constant factor of  $\frac{1}{2}$  in Equation (1.26) and where  $P(\theta)$  is the polarization factor (Equation (1.5))) is related to the number of crystals favourably orientated for Bragg scattering. In the high-resolution limit  $\beta = 0$  for a perfect crystal and  $\beta = 1$  for a perfect powder [5, 7]. For natural clays and finite resolution measurements the correct value of  $\beta$  is unknown, and what is only certain is that the value of  $\beta$  is in between these limits.

The integrated intensity,  $I_{sc}$ , is found by the multiplication of the differential cross-section in equation (1.27) with incoming flux,  $\Phi_0$  (the number of photons per unit area per unit of time)

$$I_{sc} = \Phi_0 \cdot \left( \frac{d\sigma}{d\Omega} \right) \quad (1.29)$$

### 1.2.8 Scattering from a layered clay

For larger crystals almost all the scattering is concentrated at the Bragg angles of diffraction and hence only the structure factor  $F$  is needed. The shape of the diffraction peaks carries little information, and Equation (1.27) is valid.

However, for small, thin crystals as those of clay minerals, there is additional scattering adjacent to the  $hkl$  diffraction peak positions and even in small amounts between these 'normal' positions [5]. The characteristics of diffraction peak shapes originating in this extra scattering, and the correlation with the structural aggregates of unit cells, can be separated from the structure of the unit cell itself. This extra contribution is termed *the interference function*  $\Gamma$  and is a continuous function in  $\theta$ .

#### Layer structure factor

The structure factor of the unit cell,  $F(\vec{Q})$  (Equation (1.10) and Equation (1.11)),

$$F^{\text{unit cell}}(\vec{Q}) = \sum_{\vec{r}_j} f_j(\vec{Q}) e^{i\vec{Q} \cdot \vec{r}_j}$$

is however defined by  $hkl$ . Hence it is not a continuous function in  $\theta$ .

---

<sup>37</sup>As the Lorentz factor and the polarization factor always occur together, it is in practice convenient to be able to correct for them simultaneously.

The transformation of a discrete structure factor in  $hkl$  to a continuous function in  $\theta$  is simple in the one dimensional case; we define a function  $G$ , also known as the *layer structure factor* or *layer scattering factor* [5], which is essentially the same as  $F$ , though continuous in  $\theta$ . Considering the sample as a centrosymmetric system it permits us to write the structure factor as [5]

$$G(\theta) = \sum_j n_j f_j(Q) \cos(Qz_j)$$

where the summation is still taken over all the atoms of the unit cell,  $f_j$  is the temperature-corrected atomic form factor (Equation (1.21)),  $n_j$  is the number of atoms of type  $j$  located at the distance  $z_j$  from the origin of the structure, which in the case of Na-fluorohectorite is chosen to be the plane defined by the Mg and Li atoms in the octahedral layer.<sup>38</sup> Considering the relationship  $\vec{Q} = \vec{k} - \vec{k}'$  for the one-dimensional case, we get

$$Q = 2k \sin \theta$$

from geometrical considerations (see Figure 1.12 on page 14). Setting  $k = \frac{2\pi}{\lambda}$ , we find  $Q = \frac{4\pi}{\lambda} \sin \theta$ , and

$$G(\theta) = \sum_j n_j f_j(\theta) \cos\left(4\pi z_j \frac{\sin \theta}{\lambda}\right) \quad (1.30)$$

From Equation (1.21) and the expression for the exponent in the Debye-Waller factor  $e^{-W_j(Q)}$  (page 19), the atomic form factor's  $\theta$ -dependency can be expressed as

$$f_T^{\text{atomic form factor}}(\theta) = f_{\text{rest}}^{\text{atomic form factor}} e^{-B_T \left(\frac{\sin \theta}{\lambda}\right)^2}$$

where  $f_{\text{rest}}^{\text{atom}}(\theta)$  is the atomic form factor at rest,  $f_T^{\text{atom}}(\theta)$  is the temperature-corrected value while  $B_T$  is a measure of the mean square displacement of an atom from its equilibrium position in the structure.<sup>39</sup>

Thus Equation (1.30) can be fully expressed as

$$G(\theta) = \sum_j n_j f_j^{\text{rest}} e^{-B_T^j \left(\frac{\sin \theta}{\lambda}\right)^2} \cos\left(4\pi z_j \frac{\sin \theta}{\lambda}\right) \quad (1.31)$$

with the physical interpretation of  $|G|^2$  being the square of the scattered amplitude from a single unit cell oriented such that its *ab*-plane makes the angle  $\theta$  with respect to the incident beam.

### Interference function $\Gamma$

A layered clay will function as a *diffraction grating* for the purpose of X-ray diffraction [28]. A diffraction grating can be modeled as a series of equispaced slits. The net electric field is the sum of all the component fields. Given the slit separation,  $d$ , the optical path difference between successive beams for a given observation angle  $\theta$  is  $2d \sin \theta$ , and the corresponding phase difference  $\Delta\phi = 4\pi d \frac{\sin \theta}{\lambda}$  (geometry shown in Figure 1.16).

<sup>38</sup>The complex value of  $G$  consists of real cosine terms and complex sine terms. When squared, in order to find the intensity, the sine terms disappear because of the invoked symmetry ( $\sin(x) = -\sin(-x)$ ).

<sup>39</sup>Thermal diffuse scattering (TDS) is neglected.

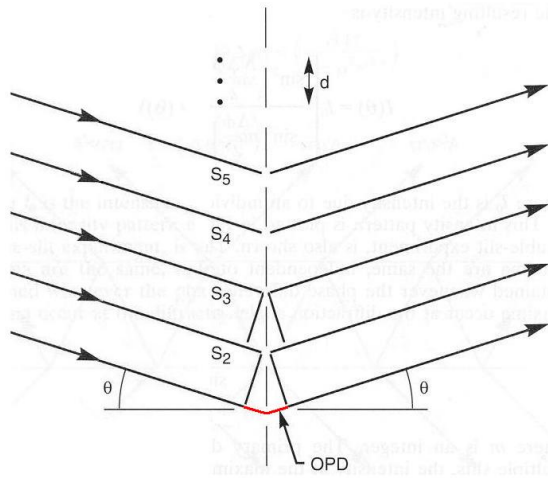


Figure 1.16: The layered clay creates as a diffraction grating resulting in multiple wave interference as a function of differences in the optical path distance (OPD). Modified from [28].

The field due to the  $n$ th slit at a distant observation point is

$$E_j(\theta) = Ae^{i(j-1)\Delta\phi}, , j = 1, 2, \dots N$$

where all of the beams have been referenced to the first slit, and there are  $N$  total slits. The net field is

$$E(\theta) = \sum_{j=1}^N E_j(\theta) = A \sum_{j=1}^N (e^{i\Delta\phi})^{j-1}$$

which, being a geometrical series (see page 94), simplifies to

$$E(\theta) = A \frac{1 - e^{iN\Delta\phi}}{1 - e^{i\Delta\phi}}$$

The resulting intensity, proportional to the squared absolute value of the field, is

$$I(\theta) = I_0 \left[ \frac{\sin^2 \left( \frac{N\Delta\phi}{2} \right)}{\sin^2 \left( \frac{\Delta\phi}{2} \right)} \right] = I_0 \left[ \frac{\sin^2 \left( 2N\pi d \frac{\sin \theta}{\lambda} \right)}{\sin^2 \left( 2\pi d \frac{\sin \theta}{\lambda} \right)} \right]$$

where  $I_0$  is the intensity due to an individual slit.

The locations of the maxima are the same, independent of the number of slits. A maximum of intensity is obtained whenever the phase difference between adjacent slits is a multiple of  $2\pi$ . The maxima occurs at the diffraction angles given by

$$\sin \theta = \frac{n\lambda}{2d}$$

<sup>40</sup>where  $n$  is an integer; that is at the Bragg angles. The intensity at the maximum increases to  $N^2$  times that of a single slit, an this energy is concentrated

---

<sup>40</sup>This is the Laue interference function/Bragg's law.

into a much narrower range of angles. Thus the interference function produces peaks with equal areas for all  $00l$  diffraction positions. The full width of a diffraction peak between intensity zero corresponds to a phase difference  $\Delta\phi$  of  $\frac{4\pi}{N}$ . The number of intensity zeros between the peaks is  $N - 1$ . As the number of slits increases, the angular resolution or resolving power of the grating greatly increases.

The *interference function*  $\Gamma$  for the purpose of Na-fluorohectorite is thus a continuous function in  $\theta$  and given by

$$\Gamma(\theta) = \frac{\sin^2(2\pi N d \frac{\sin \theta}{\lambda})}{\sin^2(2\pi d \frac{\sin \theta}{\lambda})} \quad (1.32)$$

where  $N$  is the number of unit cells stacked in coherent scattering array along the axis perpendicular to the interlayers and  $d$  is the interplanar distance  $d_{001}$ .

The assumption that diffraction occurs only for crystals of exactly  $N$  unit cells is unrealistic, and mathematically it produces  $N - 2$  weak ripples evenly spaced. However, a more realistic assumption leading to a more realistic pattern is based on that the diffraction is composed of a series of crystallites with different  $N$  values and proportions  $p(N)$  (where  $\sum p(N) = 1$ ) [5]. The different ripples will then produce a smooth background assuming that the diffraction equation (Equation (1.32)) can be modified as

$$\Gamma(\theta) = \sum_{N=n_1}^{N=n_2} p(N) \frac{\sin^2(2\pi N d \frac{\sin \theta}{\lambda})}{\sin^2(2\pi d \frac{\sin \theta}{\lambda})} \quad (1.33)$$

This changes the form of the peaks. Among other things the tails are broader for a given width at half maximum.

### 1.2.9 Putting it all together: Intensity for a layered clay

When taking into account section 1.2.8, the intensity for a crystal (Equation (1.29) through Equation (1.27)) is modulated in the case of a layered clay yielding

$$I_{sc}(\theta) \propto |G(\theta)|^2 Lp(\theta) \Gamma(\theta) \quad (1.34)$$

where  $I_{sc}$  is the measured intensity,  $G$  the continuous unit cell structure factor (Equation (1.31)),  $Lp$  the Lorentz-polarization factor (Equation (1.28)) and  $\Gamma(\theta)$  the interference function (Equation (1.32)), the latter of which is the sought for function.

Equation (1.34) may produce results that are at variance with Bragg's law when  $N$  is small (typical  $< 10$ ). Then the various orders will be shifted from their nominal positions due to the width of the interference function at small  $N$ . If, as often is the case, the maximum in the interference function occurs in an angular region where the  $|G|^2 Lp$  function has a significant slope, the multiplication of  $\Gamma$  will cause the peak maximum to shift in the direction of this slope. The smaller the  $N$ , the bigger the width and hence the bigger the shift.

### 1.2.10 Modelling the intensity for Na-fluorohectorite

The chemical formula for Na-FH is  $\text{Na}_x(\text{Mg}_{3-x}\text{Li}_x)\text{Si}_4\text{O}_{10}\text{F}_2$  per half unit cell where  $x$  is the variable proportion of octahedral Li atoms. For the sample used in this experiment (see 2.2.1)  $x = 0.6$ .

In this section a modelled theoretical presumption of the two hydration states (1WL and 2WL) is performed.

**Layer structure factor  $G$**  The summation of Equation (1.31) is taken over only half of the cell and the result multiplied by two, for by symmetry the other half is identical. Also note that only half of the actual number of atoms in the symmetry plane is included in the sum as they are shared by adjacent unit cells.

Half-ionized atomic scattering factors are used for Si and silicate O ( $\text{Si}^{3+}$  and  $\text{O}^-$  respectively), while fully ionized values are used for the other cations. For water and  $\text{OH}^-$  the scattering factor is the sum of the factors for  $\text{H}^+$  and  $\text{O}^{2-}$  [5].

The evaluation of the complete atomic scattering factor (Equation (1.8)) is an elaborate process. The 'normal' (non-dispersive) coherent contribution  $f^0$  is found in literature as a discrete function of the Bragg angle as well as the energy of the radiation (through the momentum transfer  $\vec{Q}$  in Equation (1.7) and the Laue condition (or Bragg's law) for constructive interference) and consequently has to be fitted with a proper function in order to be continuously evaluated over the proper interval of interest.

The dispersive contributions,  $f'$  and  $f''$ , are multi-termed, where each term is tabulated in [29]. Two of these terms are discretely tabulated as a function of energy, and thus a function fit is appropriate in order to determine the contribution for the proper wavelength of this experiment.

For a fully and detailed elaboration of the complete atomic scattering factor, see Appendix B. The results for the complete atomic scattering factor squared over the appropriate angular interval ( $2\theta \in [2.0^\circ, 10.8^\circ]$ ) are summarized in Table 1.1.

The distance  $z$  from the location of the atom to the origin, in this case the horizontal plane defining the center of symmetry of the platelet (the octahedral Li and Mg atoms), and the proportions of each element of the intralayer clay sheets were obtained from [7]. See Figure 1.17.

Typical values of  $B_T$  for layer silicates show considerable variations as the quantity includes not only the effects of thermal vibration, but also the effects of structural and substitutional order. From crystal structure analysis different values for each atom in the unit cell have been isolated suggesting that  $B_T \sim 1.4$  for cations and  $B_T \sim 1.8$  for oxygen are good average values for layer silicates [30]. Other literature suggests  $B_T \sim 1.5$  for cations and  $B_T \sim 2$  for anions, while  $B_T \sim 11$  is used for one of the water molecule sites in the two layered water-smectite structure [5]. [31] also suggests  $B_T \sim 11$  for one of the molecule sites in the bi-hydrated case and  $B_T \sim 2$  for the other water molecule sites.<sup>41</sup> In [7]  $B_T \sim 1.6$  is utilized for all of the intercalants.

---

<sup>41</sup>In [31] it is shown that accounting for hydration heterogeneity (which means that the water molecules may display different values) allows better fitting of the profiles of all experimental  $00l$  reflections for the bi-hydrated case, especially for the higher order reflection peaks.

$ f ^2$ for $2\theta \in [2.0^\circ, 10.8^\circ]$	
H	3.4535E-07†
Li	[3.9951,3.9006]
O	[81.8530,73.5716]‡ [101.0170,90.5710]††
F	[101.3753,94.7750]
Na	[102.4551,99.1559]
Mg	[103.2587,100.7009]
Si	[126.5147,122.5386]

Table 1.1: Atomic scattering factor squared for all of the composite elements of Na-FH.

† Hydrogen appears as  $H^+$ -ion (or proton). Thus there are no scattering electrons present, and only the dispersive contributions are included, for which the order indicates that they can be neglected.

‡ For the  $O^-$  case.

†† For the  $O^{2-}$  case.

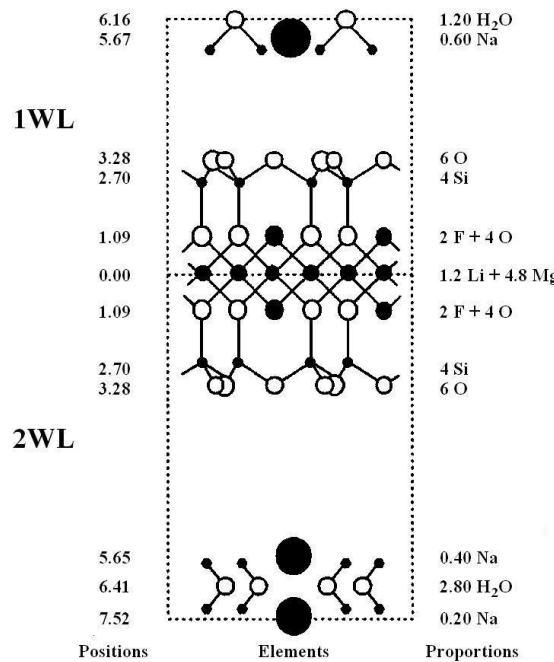


Figure 1.17: Schematic representation of the elements comprising the Na-fluorohectorite unit cell (see also Table 1.2). The centre of symmetry defined by the octahedral Li and Mg atoms is taken as origin. The positions are labeled on the left whereas the proportions are labeled on the right. The upper and lower halves represent the 1WL and 2WL case respectively. Taken from [7].

	$z(\text{\AA})$	$n$	$ f ^2$	$B_T$
<b>Silicate layer</b>	0.0	0.6Li	[3.9951, 3.9006]	1.4
		2.4Mg	[103.2587, 100.7009]	1.4
	1.09	2F	[101.3753, 94.7750]	1.8
		4O	[101.0170, 90.5710]	1.8
	2.70	4Si	[126.5147, 122.5386]	1.4
	3.28	6O	[81.8530, 73.5716]	1.8
	$n$	$z(\text{\AA})$	$ f ^2$	$B_T$
<b>One water layer (1WL)</b>	5.67	0.6Na	[102.4551, 99.1559]	1.6
	6.16	1.2H <sub>2</sub> O	[101.0170, 90.5710]	1.6
	$n$	$z(\text{\AA})$	$ f ^2$	$B_T$
<b>Two water layers (2WL)</b>	5.65	0.40Na	[102.4551, 99.1559]	1.6
	7.52	0.20Na	[102.4551, 99.1559]	1.6
	6.41	2.8H <sub>2</sub> O	[101.0170, 90.5710]	1.6

Table 1.2: Values for the proportions  $n$  [7], the positions  $Z(\text{\AA})$  [7], the atomic form factors  $f$  and the Debye-Waller  $B_T$  values [30].

However, we observe from the exponential term  $e^{-B_T(\frac{\sin \theta}{\lambda})^2}$  that as long as the calculated intensities are restricted to low diffraction angles, large errors will not be caused by uncertainties in  $B_T$ .<sup>42</sup>

Thus the layer structure factor squared  $|G|^2$  is by Equation (1.31) illustrated graphically in Figure 1.18 for the angular interval where the two hydration peaks (1WL and 2WL) appear. Structural parameters used for the calculations are listed in Table 1.2.

**Lorentz-polarization factor  $L_p$**  The Lorentz-polarization factor for random powders ( $\beta = 1$ ) and for single crystals ( $\beta = 0$ ) are very different at low values of  $2\theta$ . Previous experiments [7] using clay from the same original sample provided a fitted  $\beta$  parameter to the Lorentz-polarisation factor (Equation (1.28)) of  $\beta = 0.98 \pm 0.14$  and  $\beta = 0.94 \pm 0.16$  for the 0WL and 1WL case respectively. For our purpose the mean value of  $\beta = 0.96$  was chosen for both hydration cases.<sup>43</sup>

The multiplicity of Na-FH clay mineral is 1. However, in this context it is of no importance.<sup>44</sup>

Thus the general Lorentz-polarization factor (Equation (1.28)) in this case is concretized as

$$L_p \propto \frac{1 + \cos^2 2\theta}{\sin 2\theta \sin^{0.96} \theta} \quad (1.35)$$

Figure 1.19 shows a graphical representation of the Lorentz-polarization factor determined by Equation (1.35).

<sup>42</sup>For instance at  $2\theta = 10^\circ$   $B_T$  values of 1.0 and 2.0 amounts to a difference in the layer structure factor of only  $\sim 0.3\%$ . At lower angles the difference is less.

<sup>43</sup>A mean value of  $\beta = 0.96 \pm 0.16$  is typical for natural clay minerals [7].

<sup>44</sup>This factor is static and therefore unimportant for studying the dynamical diffusive behaviour.

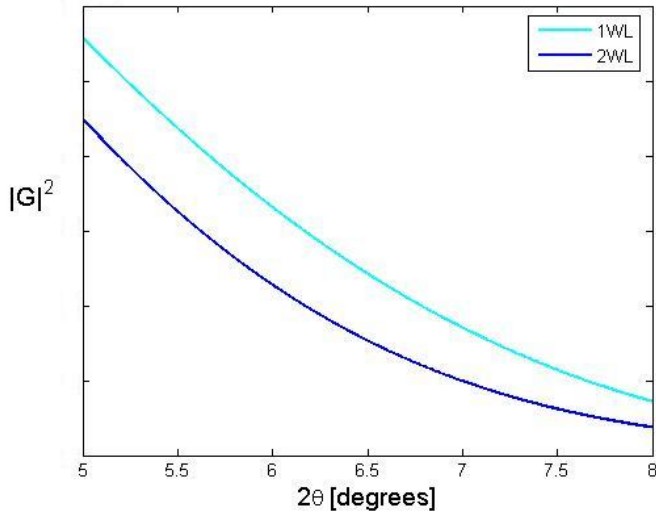


Figure 1.18: Graphical representation of the layer structure factor squared,  $|G|^2$ , over the interval  $2\theta \in [5.0^\circ, 8.0^\circ]$ . Note that different hydration states imply different factors. For transition states an intermediate factor of the two must be assumed.

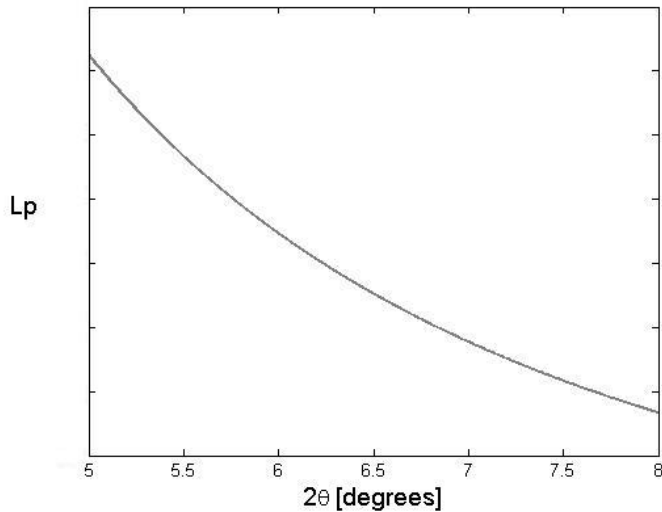


Figure 1.19: Graphical representation of the Lorentz-polarization factor,  $Lp$ , over the interval  $2\theta \in [5.0^\circ, 8.0^\circ]$ . Note that this factor is independent of hydration state.

The combined effect of the squared layer structure factor and the Lorentz-polarization factor,  $|G|^2 Lp$ , is demonstrated in Figure 1.20. For the angular range covered in this experiment this calculated effect is sufficiently consistent with the corresponding experimentally obtained plot in [7].<sup>45</sup>

<sup>45</sup>There seems to be a scaling error in the abscisse of Figure 6 in [7]. Also note that different polarization factors (Equation (1.5)) are prevailing for the two respective experiments. This

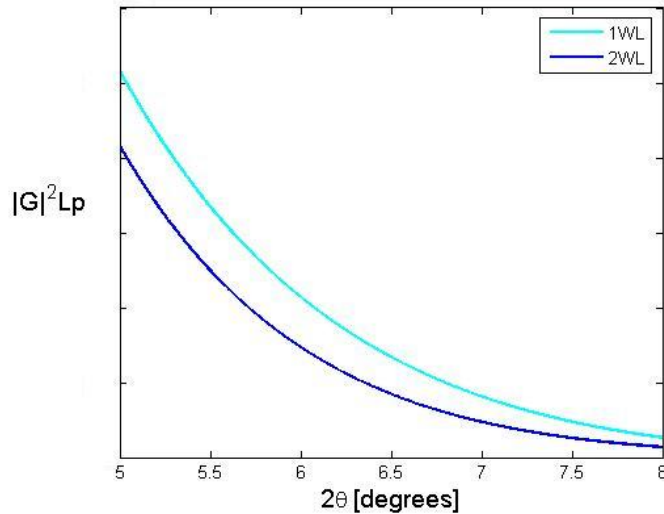


Figure 1.20: Graphical representation of the squared layer structure factor and the Lorentz-polarization factor,  $|G|^2 Lp$ , over the interval  $2\theta \in [5.0^\circ, 8.0^\circ]$ .

**Interference function  $\Gamma$**  The interference function originates in thin crystals creating additional scattering adjacent to or between the 'normal' diffraction positions determined by the structure factor  $F$ . The interference function shows maxima of equal intensity at the Bragg angles and thereby carries the very information that relates the measured intensity to the interplanar distance  $d_{001}$  through Bragg's law. *Thus this function is of the very interest for the purpose of studying the dynamics of the intercalation front* (and thereby hopefully the dynamics of the diffusion).

Figure 1.21 shows a graphical representation of the interference function  $\Gamma$  determined by Equation (1.32) and the assumption of a clay crystallite composed of  $\sim 100$  platelets.

**Method**  $\Gamma$  applies to centers that scatter equally in all directions. However, real minerals do not contain such centers, and as we have seen, the observed diffraction profile consists of  $\Gamma$  multiplied by other factors (Equation (1.34)).<sup>46</sup>

Thus, in order to study the dynamics of the intercalation front, *the measured intensities must be adjusted for unwanted contributing factors*, in the case of Na-FH primarily  $G$  and  $Lp$ , before applying the analysis to the then 'pure' interference function,  $\Gamma$ .

---

taken into account the agreement is sufficient for *low* angles. For higher angles both the shapes and scaled amplitudes seem to differ slightly. This disagreement may be due to differently chosen scattering factors (the scattering factors presented in this experiments were based on *ionized* elements) and Debye-Waller factors (which mainly gives a noticeable contribution at higher angles).

<sup>46</sup>Equation (1.34) in fact demonstrates that the atomic distribution in an individual unit cell is experimentally observable only when the interference function has finite values, or as stated in [30] as "the interference function provides the only 'window' through which we may study the layer factor, that is, the atomic structure of the unit cell."

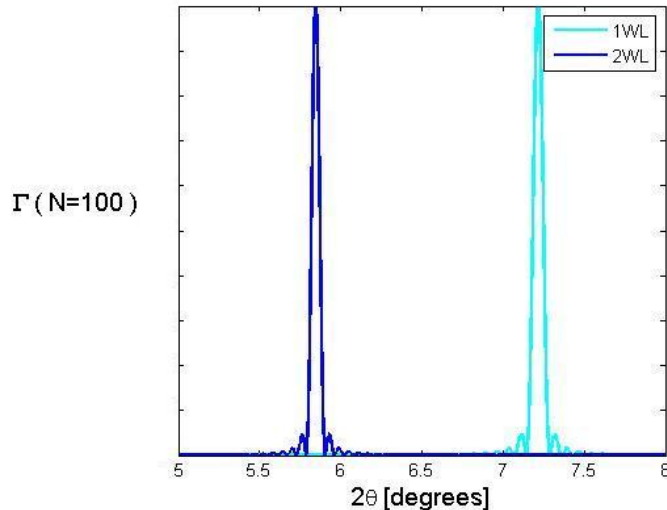


Figure 1.21: Graphical representation of the interference function,  $\Gamma$ , over the interval  $2\theta \in [5.0^\circ, 8.0^\circ]$ . Note that the peaks for different pure hydration states (1WL and 2WL) are identical in shape and differs only by the angular centering.  $N = 100$  stacked platelets in a clay crystallite is assumed.

In Figure 1.22 a comparison of the contributions from the different factors ( $|G|^2$ ,  $L_p$  and  $\Gamma$ ) is displayed, while Figure 1.23 represents the final expected *theoretical* intensity for the two pure hydration states (1WL and 2WL) in Na-fluorohectorite.

### 1.2.11 Peak width

Note that destructive interference is just as much a consequence of diffraction from a periodically repeating structure as is constructive interference. The slightest deviation from the Bragg angle, and destructive interference from a multilayer structure will occur making the Bragg peaks narrow. For an infinite layered structure, the Bragg peaks will in fact modulate delta functions, that is the width tending to zero. However, as no real structure is infinite layered, the peaks will demonstrate a finite width (see also 1.2.4, especially Equation (1.15) on page 17.)

**Instrumental width** Other factors contribute to the peak broadening. Although assumed perfectly collimated and perfectly monochromatized incident beam, neither is technically possible and both of these deviations add some peak broadening. These effects are purely *instrumental*. Other instrumental factors add to this instrumental width.

**Sample width** Several microstructural parameters contribute to the sample peak broadening. The diffraction peaks, when corrected for all non-Bragg components, i.e. background, instrumental contribution etc., bear informations

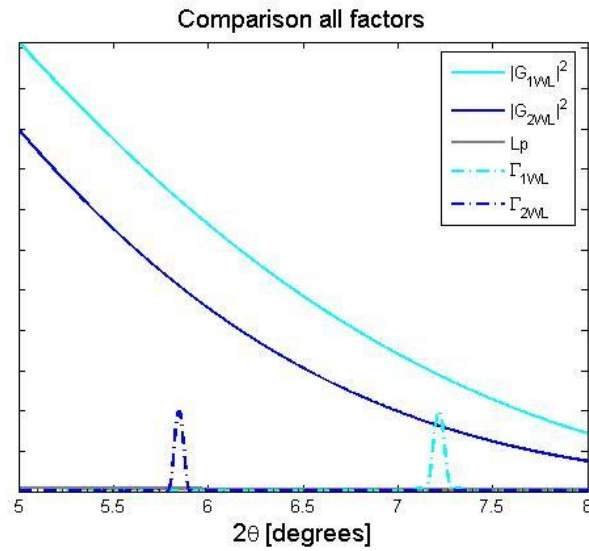


Figure 1.22: Graphical comparison of the different contributing factors,  $\Gamma$ ,  $L_p$  and  $|G|$ , over the interval  $2\theta \in [5.0^\circ, 8.0^\circ]$ . The  $L_p$  factor is very small in size compared to  $|G|^2$  and  $L_p$  (it almost disappears in the abscisse), however its contribution is essential due to that it is biased with respect to the angular distribution (see Figure 1.19).

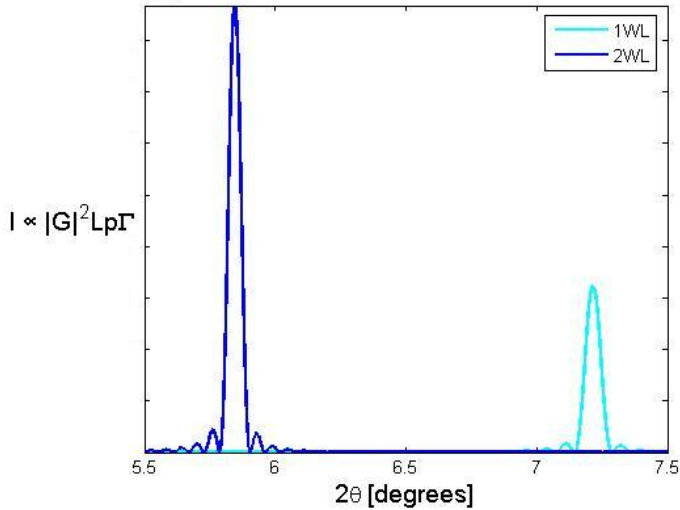


Figure 1.23: Theoretical modelled intensity for pure hydration states in Na-fluorohectorite. Note that the area of the 2WL hydration states is expected to be almost three times that of the 1WL hydration state according to this model.

about crystallite size, mean-square strain and other microstructural parameters [32].

*Disorder* A characteristic of all minerals is imperfection in crystal order because of their small crystal size. Many clays are often  $1000\text{\AA}$  in the largest

dimension and may have disordered subunits within this distance. These small crystallites cause noticeable line broadening.

This line broadening effect which results from random displacements of unit cells or groups of unit cells from their ideal positions of perfect registry, is simply denoted *strain broadening*.

*Shape transform* Particle-size broadening or, in the case of Na-fluorohectorite, thickness of the crystal is conveniently inferred from the FWHM [5]. Since the thickness only is of the order micrometer, the extension of the scattering region due to the limitation of the lattice in the direction of the beam is considerable. An estimate of the particle-size or the crystal thickness can be found by the *Scherrer equation*[5]

$$L = \frac{\lambda K}{\beta \cos \theta} \quad (1.36)$$

where  $\lambda$  is the radiating wavelength,  $L$  the mean crystallite dimension<sup>47</sup> along a line normal to the reflecting plane,  $K$  is a shape factor, a constant near unity,<sup>48</sup> and  $\beta$  is the FWHM.

*Impurities* Another reason for line broadening is the impurity of the sample and hence the mixed layering, also known as interstratification, of different kinds of clay minerals. This, however, is not a big issue concerning *synthetic* clays, although the degree of ion exchange may affect the line broadening.

*Temperature* Finally temperature (phonons) contributes to the peak broadening. However, a further investigation of this effect is omitted in this context.

### 1.2.12 Hendricks-Teller state

The behaviour of the hydration states in smectite clays is dependant on several external parameters (humidity, temperature, pressure etc.) [33]. Changing these parameters will often, once a critical parameter is reached, effectuate a hydration transition from one state to another. This transition is a *dynamic* transition; thus we may encounter a two-state coexistence which will be manifested in the recorded diffraction spectra. In general, this phenomena gives rise to different maxima which are found at positions intermediate between the poles of the two constituents [9]. Furthermore, the exact position of this combined band depends upon the proportion of each component and the state of ordering of the sequence of layers.

In 1953 Hendricks and Teller published a report on diffraction phenomena caused by different types of disorder, in particular layer lattices in which phase shifts between consecutive layers and the layer structure factor are not strictly periodic [34]. The application of this assumption comprises the case of water intercalation in smectite clays, and a formulae for the diffraction effect to be expected from random interstratification of pairs of spacings likely to occur in this type of clay is easily developed.

The purpose of this section is to enlighten the effects of mixed water intercalation states on the diffraction spectra and very briefly calculate the accompanying diffraction formulae.

---

<sup>47</sup>  $L$  is equivalent to the value of  $N$  times  $d_{001}$  in Equation (1.32)

<sup>48</sup> A more accurate value of  $K$  is 0.91 [30]

### Formula for random interstratification

For the case of a finite number of phase shifts between layers, Hendricks and Teller made the following assumptions: 1) all layers have the same structure factors, 2) all crystallites are of infinite extent and 3) the succession of phase changes is completely random.

The amplitude of the radiation for the entire clay crystallite is obtained from adding the scattered radiation from all layers constituting the crystallite. Thus the problem is reduced to a one dimensional challenge as the calculation is reduced to a single summation over layer structure factors.

The scattered radiation may be represented by a vector in the complex plane

$$|\vec{\Psi}| = \Psi e^{i\varphi}$$

where  $\Psi$  is the amplitude and  $\varphi$  the phase of the wave. The influence of the layer structure factor is included in  $\Psi$ . Let  $\vec{\Psi}_k$  represent the scattering from the  $k$ th layer, and assume, for the sake of simplicity, that only two phase shifts,  $\varphi^{(1)}$  and  $\varphi^{(2)}$ , between neighbouring layers may occur.<sup>49</sup> Then the total scattering function from the entire crystallite of  $n$  layers will be

$$\vec{\Psi}_{\text{total}} = \sum_{k=1}^n \vec{\Psi}_k$$

and subsequently the total intensity

$$I_{\text{total}} = |\vec{\Psi}_{\text{total}}|^2 = \vec{\Psi}_{\text{total}}^* \cdot \vec{\Psi}_{\text{total}}$$

Hence, the average intensity per layer is

$$I = \frac{1}{n} \sum_{k=1}^n \sum_{l=1}^n \vec{\Psi}_k^* \cdot \vec{\Psi}_l$$

Intermediate calculations<sup>50</sup> give

$$\bar{I} = \Psi^2 \frac{1 - [\cos \frac{1}{2}(\varphi^{(1)} - \varphi^{(2)})]^2}{1 - 2 \cos \bar{\varphi} \cos \frac{1}{2}(\varphi^{(1)} - \varphi^{(2)}) + [\cos \frac{1}{2}(\varphi^{(1)} - \varphi^{(2)})]^2} \quad (1.37)$$

where  $\bar{\varphi} = \frac{1}{2}(\varphi^{(1)} + \varphi^{(2)})$ . Equation (1.37) gives the mean scattered intensity in every direction for which  $\Psi \neq 0$ . If both  $\varphi^{(1)}$  and  $\varphi^{(2)}$  approach multiples of  $2\pi$  at the same rate as their difference approaches multiples of  $2\pi$ , then the equation approaches infinity.<sup>51</sup> This corresponds to the case of interference maxima, as should be the case.

Equation (1.37) will produce sharp interference maxima where the maxima of these two crystallite conditions respectively ( $2\theta_c^{(1)}$  and  $2\theta_c^{(2)}$ ) occur near the same angle. On the other hand, lower and wider maxima are found for the case of isolated maxima poles of the two conditions [34].

<sup>49</sup>This corresponds to the case where there are either one or two water layers between two neighbouring layers.

<sup>50</sup>Specially interested readers are advised to see [34]

<sup>51</sup>The nominator approaches zero linearly while the denominator approaches zero quadratically.

Another way of expressing Equation (1.37) would be by [35]

$$\bar{I} \propto \left[ \frac{2p(1-p) \sin^2 \left( \pi \frac{(d_2-d_1)}{d'} \right)}{1 - 2p(1-p) \sin^2 \left( \pi \frac{(d_2-d_1)}{d'} \right) - p \cos 2\pi \frac{d_1}{d'} - (1-p) \cos \pi \frac{d_2}{d'}} \right] \quad (1.38)$$

where  $p$  ( $0 \leq p \leq 1$ ) is the proportion of expanded layers and  $(1-p)$  the proportion of unexpanded layers.  $d'$  is the *apparent* interlayer spacing (apparent due to its continuous representation and hence does not necessarily represent any physical interplanar distance), whereas  $d_1$  represents the higher and  $d_2$  the lower interlayer spacing.

### Remarks

Of the three assumptions for the derivation of the Hendricks-Teller mixed intercalation state in the previous subsection, the two first are obviously impossible in reality; the first assumption is equal to saying that the identical layers are separated by different distances, but with no interlayer material to support these separations. However, provided that the layers consist of relatively heavy atoms and the interlayer material is of low scattering power, then the assumption is reasonably accurate.<sup>52</sup>

The second assumption implies diffraction peaks approaching a delta function, i.e. very sharp. However, finite crystallites of small size show considerable peak broadening,<sup>53</sup> though otherwise the diffraction pattern is the same [35].

It should be stated that this is a very simplified description of the real physical conditions, which for the time being lacks a complete description.<sup>54</sup> However, this simplified model does provide a very basic explanation of the intermediate peaks that often occurs in the dynamical transitions from one hydration state to another.

## 1.3 Diffusion

*Diffusion* is a type of transport phenomena described as the spontaneous spreading of matter (particles), heat or momentum. The transport originates in the driving force of the system towards chemical equilibrium and is consequently due to movement of particles from a higher to a lower chemical potential.<sup>55</sup> Thus diffusion is a physical process rather than a chemical reaction. Furthermore it is a spontaneous process. In most cases the chemical potential can be represented by a change in the concentration.

---

<sup>52</sup>Hendricks and Teller also provided calculations in cases of different layer structure factors, but the additional mathematical complications are not justified for in this context.

<sup>53</sup>See 1.2.4 and 1.2.8 for details.

<sup>54</sup>There is current research on this matter going on [36].

<sup>55</sup>Diffusion is a direct result of the second law of thermodynamics, stating that the entropy or disorder of any closed non-equilibrium system must always increase with time until equilibrium is reached. When water vapor is diffusing from a region with high concentration to a region of lower concentration, the water is moving from a higher order to a lower order state in accordance with the second law of thermodynamics.

### Short on random walks and diffusion

A *random walk* considers a 'walker' which starts at a given point and takes steps in random directions. Sometimes the length of the step may be random as well. In the limit as the steps length and time between steps both goes to zero, the walker inhibits a form of *Brownian motion* [37].

The *Central Limit Theorem* simply states that 'most' random walks spread out like *normal diffusion*. Mathematically normal diffusion is defined as the variance of a group of random walkers growing *linearly* in time;  $\langle (\Delta x)^2 \rangle = D \cdot t$  where  $D$  is the diffusion constant and  $t$  the time. By the Central Limit Theorem, for most random walks the details of the random walk only change the diffusion constant.

For *anomalous diffusion* the variance does not vary linearly with time, but goes like  $\langle (\Delta x)^2 \rangle \propto D \cdot t^\gamma$  ( $\gamma = 1$  naturally still corresponds to normal diffusion).  $\gamma > 1$  is defined as *superdiffusion*, which for instance applies to the fragments of an exploding rocket (thereby often also called ballistic diffusion). In some cases  $\gamma < 1$ , which is denoted *subdiffusion* and corresponds to cases where average time steps become infinite<sup>56</sup> [37].

### Diffusion equation

For quantitatively modelling diffusion, different diffusion equations are used for different diffusion forms. For a steady-state<sup>57</sup> bi-molecular diffusion, we utilize *Fick's first law*

$$\vec{j} = -D(W) \nabla W(\vec{r}, t) \quad (1.39)$$

which assumes that the net flux of the transported molecules is equal to the physical property of *diffusivity* (diffusion coefficient),  $D$ , multiplied by a local concentration gradient,  $\nabla W$ .

The *continuity equation*,

$$\frac{\partial W}{\partial t} + \nabla \cdot \vec{j} = 0$$

where  $\vec{j}$  is the flux of the diffusing material, combined with *Fick's first law* yields the *diffusion equation*

$$\frac{\partial W}{\partial t} = \nabla \cdot D(W) \nabla(\vec{r}, t) \quad (1.40)$$

a nonlinear partial differential equation where  $W$  is the density of the diffusing material,  $D$  is the diffusion coefficient and  $\vec{r}$  and  $t$  the spatial and time coordinates respectively. Also notice that the continuity equation introduces a time dependency, thus applying the diffusion equation to non-steady- or continuously changing state situations<sup>58</sup> as well. Equation (1.40) also goes by the name of *Fick's second law*.

<sup>56</sup>An infinite average step size only means that while long steps are rare, they are not so rare that the average term is finite.

<sup>57</sup>Steady-state implies that the concentration within the diffusion volume does not change with respect to time;  $\vec{j}_{in} = \vec{j}_{out}$ .

<sup>58</sup>i.e. when the concentration within the diffusion volume changes with respect to time.

## Clay

The porosity of Na-fluorohectorite was briefly mentioned in 1.1.1. From [6] we know that the porosity (pore-volume to total volume in the dried-out 0WL state) of the sample used in this experiment is 41%. Here we study the transport of water vapor through the porous network originating from both the interparticle as well as the interlayer spacings in the solid framework of clay crystallites. Most of the water transport is expected to take place in the mesoporous space *between* the clay grains. However, water transport is also expected in the nanoporous interlayer space between the platelets. These represent two completely different sets of pore types, and the water ingress into these pores is likely to display significantly different time constants.

Water vapor will distribute itself over the available porous space by diffusion. The subject of this study is for one thing to investigate whether or not the nature of the diffusion is normal or anomalous (see 1.3.2), and if so if it is plausible that the anomalous effect originates in the nanoporous water flow. It is important to note that we are only able to study the *intercalation front, not the water front*. The next question that naturally arises is what is then the relation between the intercalation front and the water front.

## Boltzmann's transformation

A useful mathematical technique in studying the diffusion process is the application of similarity transformations, such as *Boltzmann's transformation*

$$\eta = \frac{x}{t^{1/2}} \quad (1.41)$$

This transformation leads to approximations that are shown to be valid provided that certain physical parameters satisfy given limiting conditions [38]. These conditions are reflected in the assumption of a semi-infinite media [39] and may be explicitly expressed in the boundary conditions of the given case (see for example Equation (1.44) in 1.3.1).

The theoretical deductions of the mathematical content in the two subsequent sections (1.3.1 and 1.3.2) are mainly based on [40].

### 1.3.1 Normal diffusion

In our experiment water vapor diffuses through a highly porous medium packed in a very thin and long glass capillary. Consequently we consider the diffusion to be one-dimensional from a macroscopic point of view.

Thus, according to the one dimensional representation of Equation (1.40), we define  $W(x, t)$  as the local water concentration in a representative volume element (volume water;element volume). Then the one dimensional normal diffusion equation (deducted from Equation (1.40)) can be written as

$$\frac{\partial W(x, t)}{\partial t} = \frac{\partial}{\partial x} \left( D_1 \frac{\partial W(x, t)}{\partial x} \right) \quad (1.42)$$

where  $D_1$  is the normal Fickian diffusivity,  $D_1(W)$ , assumed to be a function only of the concentration of the diffusing medias.

Assuming the validity of Boltzmann's transformation (Equation (1.41)), we introduce a new variable, the *spatio-temporal scaling variable*  $\eta$ ,

$$\eta = \frac{x}{t^{1/2}}$$

with partial derivatives

$$\begin{aligned} \frac{\partial \eta}{\partial x} &= \frac{1}{t^{1/2}} \\ \frac{\partial \eta}{\partial t} &= -\frac{1}{2} \frac{x}{t^{3/2}} = -\frac{1}{2t} \eta \end{aligned} \Rightarrow \begin{aligned} \delta x &= t^{1/2} \delta \eta \\ \delta t &= -2t \frac{1}{\eta} t^{1/2} \delta \eta \end{aligned}$$

Thus Equation (1.42) with respect to the one spatio-temporal variable  $\eta$  becomes

$$\begin{aligned} -\frac{1}{2t} \eta \frac{\partial W(x,t)}{\partial \eta} &= \frac{1}{t^{1/2}} \frac{\partial}{\partial \eta} \left( D_1(W) \frac{1}{t^{1/2}} \frac{\partial W(x,t)}{\partial \eta} \right) \\ &= \frac{1}{t} \frac{\partial}{\partial \eta} \left( D_1(W) \frac{\partial W}{\partial \eta} \right) \\ &\Downarrow \\ -\frac{1}{2} \eta \frac{\partial W(\eta)}{\partial \eta} &= \frac{\partial}{\partial \eta} \left( D_1(W) \frac{\partial W}{\partial \eta} \right) \\ &\Downarrow \\ -\frac{1}{2} \eta \frac{dW(\eta)}{d\eta} &= \frac{d}{d\eta} \left( D_1(W) \frac{dW}{d\eta} \right) \end{aligned} \tag{1.43}$$

This very transformation is useful with the assumption of a semi-infinite ( $x \geq 0$ ) solid in contact with a water reservoir located in  $x < 0$  so that the boundary conditions can be expressed as

$$\left. \begin{aligned} W(x=0, t) &= W_0 && \text{for } t > 0 \\ W(x, t=0) &= 0 && \end{aligned} \right\} \Leftrightarrow \left\{ \begin{aligned} W(\eta=0) &= W_0 && \text{for } t > 0 \\ W(\eta \rightarrow \infty) &= 0 && \end{aligned} \right. \tag{1.44}$$

thus fulfilling the conditions for the validity of Boltzmann's transformation (Equation (1.41)).

**Application** As both the diffusion equation (Equation (1.43)) as well as the boundary conditions (Equation (1.44)) are functions of the variable  $\eta$  alone, the same should apply to the local water concentration variable,  $W = W(\eta)$ . This directly implies that a universal curve should be obtained when the normalized concentration profiles,  $\frac{W}{W_0}$ , for all values of  $x$  and  $t$ , are plotted as a function of the scaling variable  $\eta = \frac{x}{t^{1/2}}$ .<sup>59</sup>

### 1.3.2 Anomalous diffusion

*Anomalous diffusion* differs, as briefly initially stated (see page 37), from normal diffusion by the diffusion velocity. For systems displaying a lower diffusion velocity than that of normal diffusion, we denote the phenomena *subdiffusion*, whereas *superdiffusion* is the notation utilized for higher diffusion velocities.

---

<sup>59</sup>Note that it is essential to assume a concentration dependant diffusivity,  $D(W)$ , in order to achieve a scaling variable leading to a universal curve. For other assumptions such a behaviour is not guaranteed.

### Subdiffusion

*Subdiffusion* is observed in several structures. Assuming a constant generalized diffusivity,  $D_\gamma$  [cm/s $^\gamma$ ], subdiffusion can be characterized in one dimension by the mean quadratic displacement

$$\langle (\Delta x)^2 \rangle = \frac{2D_\gamma t^\gamma}{\Gamma(1+\gamma)} \quad (1.45)$$

where  $0 < \gamma < 1$  and  $\Gamma$  is Euler's gammafunction.

However, when a macroscopic concentration gradient exists in a real system displaying *normal* diffusion ( $\gamma = 1$ ), the *Fickian* diffusivity can in general not be expected to be a constant, but is assumed to vary with the local concentration of the diffusing media. A similar behaviour is also to be expected for *subdiffusive* transport areas [40].

One of several generalization of Equation (1.42) is by the method of the time-fractional diffusion equation

$$\frac{\partial^\gamma W(x,t)}{\partial t^\gamma} - \frac{t^{-\gamma}}{\Gamma(1-\gamma)} W(x,0) = \frac{\partial}{\partial x} \left( D_\gamma \frac{\partial W(x,t)}{\partial x} \right) \quad (1.46)$$

for  $0 < \gamma < 1$  and where  $D_\gamma$  is a function of  $W$ .<sup>60</sup>

We here only consider the case where the diffusivity is not a constant, but a function of the concentration of the diffusing medias, and thus seek a generalization of Equation (1.43) for  $0 < \gamma < 1$ . The boundary conditions are assumed to be

$$\begin{aligned} W_\delta(x,0) &= \delta(x) \\ W_\delta(x,t) &\rightarrow 0 \quad \text{for } x \rightarrow \pm\infty \end{aligned} \quad (1.47)$$

thereby fulfilling the criterias for the validity of Boltzmann's transformation (Equation (1.41)).

Thus the term  $W(x,0)$  in Equation (1.46) can be omitted. Once again introducing the generalized term  $\Phi(x,t) = \frac{W(x,t)}{W_0}$ , where  $W_0$  is deducted from placing a water reservoir at  $x < 0$  so that  $W(x,0) = W_0$  for all  $t > 0$ , Equation (1.46) can be written

$$\frac{1}{\Gamma(1-\gamma)} \frac{\partial}{\partial t} \int_0^t \frac{\Phi(x,t')}{(t-t')^\gamma} dt' = \frac{\partial}{\partial x} \left( D_\gamma(\Phi) \frac{\partial \Phi(x,t)}{\partial x} \right) \quad (1.48)$$

Then rewriting the variables

$$u = \frac{t'}{t} \quad \eta = \frac{x}{t^{\gamma/2}}$$

and performing the time derivative in Equation (1.48), we get

$$\frac{1}{\Gamma(1-\gamma)} \int_0^t \left[ (1-\gamma)\Phi(\eta/u^{\gamma/2}) - (\gamma/2)\eta \frac{\partial \Phi(\eta/u^{\gamma/2})}{\partial \eta} \right] \frac{du}{(1-u)^\gamma} = \frac{\partial}{\partial \eta} \left( D_\gamma \frac{\partial \Phi}{\partial \eta} \right) \quad (1.49)$$

---

<sup>60</sup>The Riemann-Liouville fractional derivative operator  $\frac{\partial^\beta}{\partial t^\beta}$  is defined by

$$\frac{\partial^\beta W(x,t)}{\partial t^\beta} = \begin{cases} \frac{1}{\Gamma(1-\beta)} \frac{\partial}{\partial t} \int_0^t \frac{W(x,t')}{(t-t')^\beta} dt' & \text{for } 0 < \beta < 1 \\ \frac{1}{\Gamma(-\beta)} \frac{\partial}{\partial t} \int_0^t \frac{W(x,t')}{(t-t')^{1-\beta}} dt' & \text{for } \beta < 0 \end{cases}$$

**Application** The important issue in this context is *neither* the mathematical deduction *nor* the final differential equation itself, but the fact that Equation (1.49) and its boundary conditions (Equation (1.47)) solely is a function of the scaling variable  $\eta$  alone. Thus, as in the case of normal diffusion, a universal curve is to be expected for all values of  $x$  and  $t$ .

### 1.3.3 Method

Assume a graphical plot of the diffusive front. Introducing the scaling variable  $\eta = \frac{x}{t^{1/2}}$  as the abscisse variable as well as allowing for anomalous diffusion, represented by the time-fractional parameter  $\gamma$  (thereby  $\eta = \frac{x}{t^{\gamma/2}}$ ), we *should* obtain a universal curve according to the theory described above. Thus for normal diffusion we expect  $\gamma = 1$ , whereas  $0 < \gamma < 1$  is expected in the case of subdiffusive behaviour.

## 1.4 Pseudo-Voigtian approximation

Several functions have been used to model X-ray peak shapes, and the Voigt function has been shown to demonstrate good results [41].

As discussed in 1.2.11 there will occur a peak broadening due to both instrumental resolution and peak widths intrinsic to the sample. The combined effects of these two contributions constitute a *Voigt distribution*, which in fact is a convolution of *Gaussian* and *Lorentzian* functions. Unfortunately, an analytic form for the Voigt function is not available. However, a practical approximation to the Voigt distribution has been adopted; namely the *pseudo-Voigtian* approximation.

### 1.4.1 Gaussian distribution

The Gaussian distribution, also known as the normal distribution, is a family of distributions of the same form differing in their location and scale parameters, the mean ('average') and standard deviation ('variability') respectively [42],

$$f_G(x, \mu, \sigma) = \frac{1}{\sigma\sqrt{2\pi}} e^{-\frac{(x-\mu)^2}{2\sigma^2}} \quad (1.50)$$

$\mu$  being the mean and  $\sigma$  the standard deviation (Figure 1.24a).

### 1.4.2 Lorentzian distribution

The Cauchy-Lorentz, named after Augustin Cauchy and Hendrik Lorentz, is a continuous probability distribution with probability density function [42]

$$f_L(x, x_c, \omega) = \frac{1}{\pi\omega \left[ 1 + \left( \frac{x-x_c}{\omega} \right)^2 \right]} = \frac{1}{\pi} \frac{\omega}{(x - x_c)^2 + \omega^2} \quad (1.51)$$

where  $x_c$  is the location parameter, specifying the location of the peak, and  $\omega$  is the scale parameter, specifying the half-width at half maximum (HWHM) (Figure 1.24b).

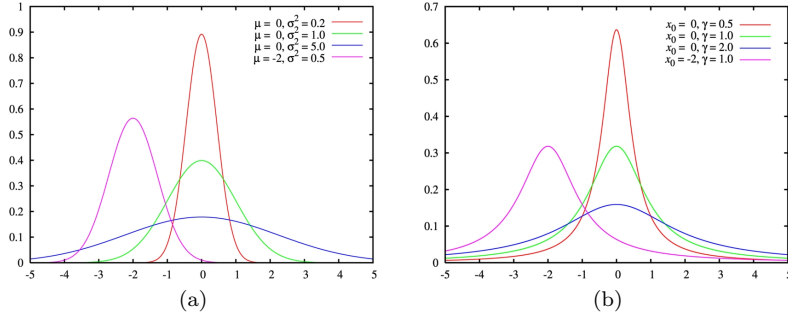


Figure 1.24: (a) Gaussian distributions with different means and standard deviation. The green line is the standard Gaussian distribution. (b) Lorentzian distributions with different location and scale parameters. The green line is the standard Lorentzian distribution.

The Cauchy-Lorentz distribution, or simply the Lorentz distribution among physicist, is among other things important in spectroscopy largely due to the fact that it describes the line shape of spectral lines which are broadened by several mechanisms.

### 1.4.3 Convolution

In functional analysis, in particular, *convolution* is a mathematical operator which takes two functions  $f$  and  $g$  and produces a third function that in a sense represents the amount of overlap between  $f$  and a reversed and translated version of  $g$ .

$$h(t) = (f \otimes g) = \int_0^t f(\tau)g(t-\tau)d\tau \quad (1.52)$$

A convolution is thus a kind of a very general moving average, as one can see by taking one of the functions to be an indicator function of an interval.

*Deconvolution* is a process used to reverse the effects of convolution on recorded data. In general, the object of deconvolution is to find the solution of a convolution equation of the form

$$f \cdot g = h$$

Usually, as in our case,  $h$  is a recorded signal, and  $f$  is the signal we wish to recover, but has been convolved with some other signal  $g$  before we recorded it. As long as we know  $g$  or at least the form of this, we can perform deterministic deconvolution.

However, in physical measurements the situation is usually closer to

$$(f \cdot g) + \epsilon = h \quad (1.53)$$

where  $\epsilon$  is noise that has entered the recorded signal. If we assume that the recorded signal is noiseless when trying to make a statistical analysis of  $g$  and  $f$ , the estimate will be incorrect. And the lower the signal-to-noise ratio, the poorer the estimate. However, if one have some knowledge of the type of noise in the data, one may be able to improve the estimate of  $g$  and hence  $f$ .

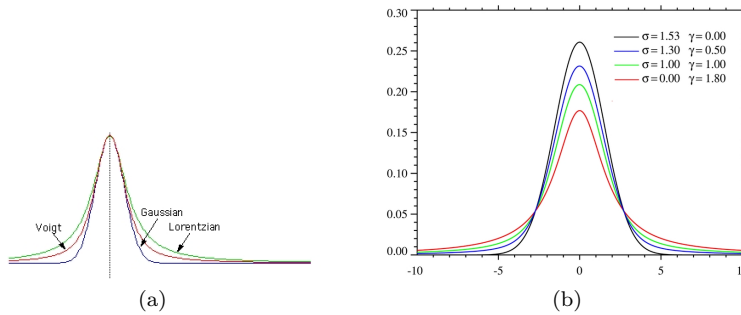


Figure 1.25: The Voigt distribution is the convolution between a Gaussian and a Lorentzian distribution. (a) The Voigtian distribution is a combination of the Gaussian and the Lorentzian distribution. (b) Voigtian distributions all centered and with combinations of different Gaussian and Lorentzian distributions (varying Gaussian standard deviation  $\sigma$  and Lorentzian scale parameter  $\omega$ ). Both figures taken from [43].

#### 1.4.4 Voigtian distribution

The Voigt distribution is therefore a convolution between a Gaussian and a Lorentzian and is often used in X-ray work.

$$V(x; \mu, \sigma, x_c, \omega) = (G \otimes L)(x; \mu, \sigma, x_c, \omega) = \int_{-\infty}^{\infty} G(\tau; \mu, \sigma) L(x - \tau; x_c, \omega) d\tau \quad (1.54)$$

The Voigt distribution is furthermore normalized since it is the convolution of normalized distributions.

#### 1.4.5 Pseudo-Voigtian distribution

The Voigt functional form has several practical applications for quantitative analysis. Unfortunately, an analytical form for the convolution of a Gaussian with a Lorentzian is not available, hence for practical systems two pseudo-Voigt approximations are adapted. The first allows for *different FWHMs*

$$f_{PV}(x; x_c, \eta, \omega_G, \omega_L) = (1 - \eta)f_G(x; x_c, \omega_G) + \eta f_L(x; x_c, \omega_L) \quad (1.55)$$

where  $f_G(x; x_c, \omega_G)$  and  $\eta f_L(x; x_c, \omega_L)$  are the normalized Gaussian and Lorentzian functions and  $\eta$  is the shape parameter that adjusts the relative contribution of the two; a shape factor of zero is pure Gaussian and a shape factor of one is pure Lorentzian.<sup>61</sup>

The second version includes Gaussian and Lorentzian distributions with *the same FWHM*,  $\omega$ ,

$$f_{PV}(x; x_c, \eta, \omega) = (1 - \eta)f_G(x; x_c, \omega) + \eta f_L(x; x_c, \omega) \quad (1.56)$$

<sup>61</sup>The domain of physical significance in terms of convolution is restricted to  $0 \leq \eta \leq 1$ . However, cases may be encountered where least-squares fitting gives values outside this range. Such sharply peaked super-Lorentzians ( $\eta > 1$ ) or flat-topped super-Gaussians ( $\eta < 0$ ) clearly indicate that other mechanisms apply [44].

However, both the shape parameter  $\eta$  and the width  $\omega$  are functions of the Gaussian and Lorentzian FWHMs,  $\omega_G$  and  $\omega_L$  respectively, through [41, 44]

$$\begin{aligned}\omega &= 1.36603 \frac{\omega_L}{\omega} - 0.47719 \left( \frac{\omega_L}{\omega} \right)^2 + 0.11116 \left( \frac{\omega_L}{\omega} \right)^3 \\ \eta &= (\omega_G^5 + 2.69269 \omega_G^4 \omega_L + 2.42843 \omega_G^3 \omega_L^2 + 4.47163 \omega_G^2 \omega_L^3 + 0.07842 \omega_G \omega_L^4 + \omega_L^5)\end{aligned}\quad (1.57)$$

It has been shown that such a linear combination using lines with the same FWHM as the Voigt profile provides an approximation accurate to about 1% [44].<sup>62</sup>

The useful range of the approximation includes lines sharper than Lorentzian and flatter at the top than Gaussian (compare with the Voigtian function, Figure 1.25a).

#### 1.4.6 Application

The noise created in this type of experiment will primarily be due to small angle scattering, which is known to follow a power law. In order to study the dynamics of the intercalation front, frequent scans (shorter scan time) will be preferred as opposed to greater resolution (long scan time) (see 2.2.3), resulting in a lower signal-to-noise ratio. Therefore, after fitting the background of the acquired data<sup>63</sup>, the noise  $\epsilon$ , according to Equation (1.53) must be subtracted from the recorded data  $h$  before properly deconvolving the signal.<sup>64</sup>

Sample-related X-ray diffraction profiles are often fitted with a pseudo-Voigt function [32]. For our purpose this is a good approximation to the experimental data, and we apply a least square approximation of the pseudo-Voigt function type II (Equation (1.56)) in the form

$$f_{PV}(x; \eta, x_c, \omega) = A \left[ \eta \frac{2}{\pi} \frac{\omega}{4(x - x_c)^2 + \omega^2} + (1 - \eta) \frac{\sqrt{4 \ln(2)}}{\sqrt{\pi} \omega} e^{-\frac{4 \ln(2)}{\omega^2} (x - x_c)^2} \right] \quad (1.58)$$

where  $A$  is the area,  $\eta$  the profile shape factor,  $x_c$  the center of the distribution and  $\omega$  the full width at half maximum. The Gaussian full width at half maximum  $\omega_G$  and the Lorentzian full width at half maximum  $\omega_L$  are subsequently derived through Equations (1.57).

---

<sup>62</sup>Better approximations have been obtained by including higher order terms, or simply by including additional peak functions [45].

<sup>63</sup>The background fitting is performed over intervals on both sides of and sufficiently far from the diffraction peaks. This small angle scattering varies with the positional sample composition. Thus a background fit must be performed for each scan frame.

<sup>64</sup>As the peak widths are relatively narrow compared to the slope of the background noise, a linear fit in the prevailing interval would be sufficient. However, we choose the power law fit as this is closer to the real physical conditions, though the fitting procedure is slightly more cumbersome. Also, this will not, at least, introduce additional errors.

# Chapter 2

# Experiment

## 2.1 Experimental setup

The X-ray scattering experiment was conducted at Norwegian University of Science and Technology (NTNU) utilizing NanoSTAR (Figure 2.1), a small angle X-ray scattering (SAXS) system, from Bruker AXS.<sup>1</sup> NanoSTAR uses a two dimensional detector and has the possibility of several different sample to detector distances.

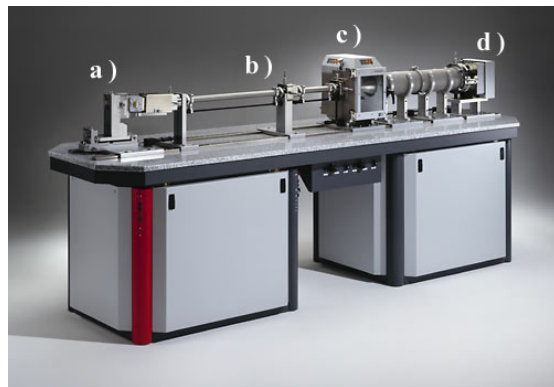


Figure 2.1: NanoSTAR hardware. a) Rotating anode b) Pinhole collimating system  
c) Sample chamber d) Detector. Taken from the Bruker webpage.

### 2.1.1 Components of the SAXS system

The instrumental setup is, broadly spoken, composed of four main parts; a generating source, a pinhole collimating system, a sample chamber and a detector. The first two parts constitute an optical system that conditions the primary X-ray beam to be monochromatic and well collimated.

---

<sup>1</sup>The main feature of the NanoSTAR SAXS system is that not only isotropic materials can be studied, by also more complex samples, especially anisotropic ones, such as fibrous or layered structures.

### Generating source

The SAXS system uses a point focus source, which means that a source with line focus  $F$  is arranged in such a way that the multilayer mirror system 'sees' a point focus. This is obtained when the mirror system is arranged in the line direction and the take off angle  $\alpha$  is small. Then the active source shape is the projection of the line and hence similar to a point. In the projection the line  $a$  is thus shortened by a factor  $\sin \alpha$  by geometrical considerations, dimensioning the 'point focus' to  $(a \sin \alpha) \times b$ . See Figure 2.2

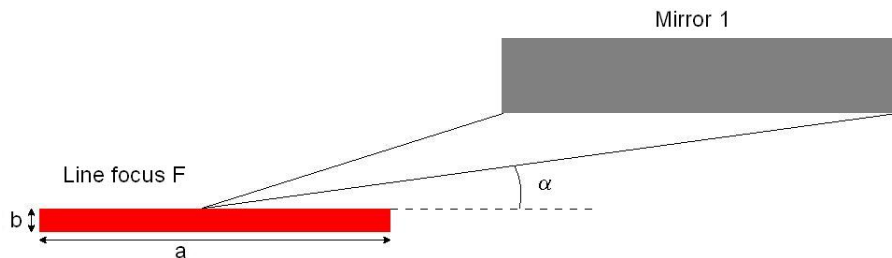


Figure 2.2: The line focus is projected to a 'point' focus with dimensions  $(a \sin \alpha) \times b$  through the geometrical setup.

The generating source is a water cooled rotating copper (Cu) anode.<sup>2</sup> A crossed coupled multilayer monochromator, the *Göbel mirrors* (Figure 2.3), selects the characteristic  $K_\alpha$  radiation from the continuous white spectrum and conditions the original two dimensional divergent beam to a two dimensional parallel beam.<sup>3</sup>

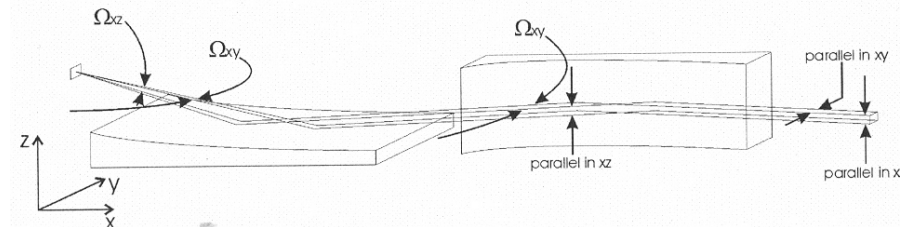


Figure 2.3: Göbel mirrors optics. The parabolic shape of the multilayers with a large scattering contrast monochromatises as well as collimates the beam. Taken from [21].

Deviations from the ideal situation implies that the 'parallel' beam of a cross coupled Göbel mirrors system without any pinhole collimating system has an intrinsic divergence FWHM of  $K_\alpha$  radiation (property of the X-ray mirror). Additionally there is a part of divergent non-monochromatic parasitic radiation of several *mrad* (property of the 'point' focus X-ray source) if no collimators, pinholes and slits are used.<sup>4</sup> See also Figure 3.8a.

<sup>2</sup>  $K_{\alpha_1} = 1.540562\text{\AA}$ ,  $K_{\alpha_2} = 1.544390\text{\AA}$ , customary weighed mean  $K_\alpha = 1.541838\text{\AA}$  and  $K_\beta = 1.392218\text{\AA}$  [46].

<sup>3</sup> Signifying a monochromatization and collimation of the X-ray radiation respectively.

<sup>4</sup> This parasitic radiation is divergent and only appears in the direct vicinity of the primary

### Pinhole collimating system

The pinhole collimation system (Figure 2.4) to a certain extent mends the above deviations and conditions a small X-ray beam with a defined cross section. The combination of three pinholes limits the divergence and shadows the edge scattering of the system.

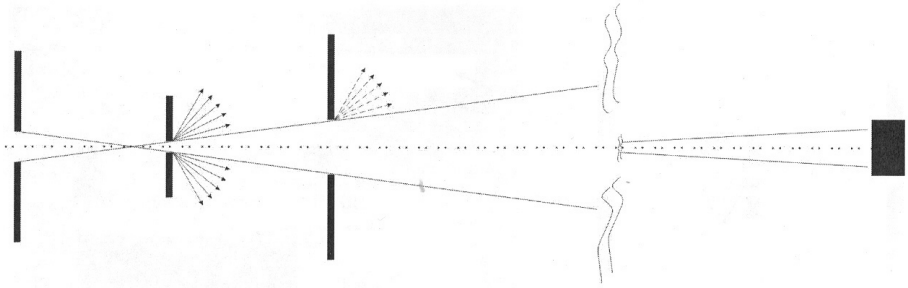


Figure 2.4: Geometrical principle of the three pinhole collimating system. The first two pinholes, called the divergence pinhole and the beam defining pinhole, limit the divergence whereas the third pinhole, the antiscatter pinhole, shadows the edge scattering of the second pinhole. Taken from [21].

The outcome from the first two parts of the NanoStar is a well defined and conditioned parallel and monochromatic X-ray beam. The size of the 'point' focus is  $0.4\text{mm} \times 0.8\text{mm}$  (width x height) [21], and the wavelength of the beam is  $\lambda = 1.541838\text{\AA}$ .

### Sample chamber

The sample chamber has a software operated goniometer drive allowing for precise and reproducible positioning of the sample in an xy-plane perpendicular to the incoming beam. This automatic sample changer allows sample positioning over distances of  $100\text{mm}$  in y- and  $80\text{mm}$  in x-direction with an accuracy of better than  $10\mu\text{m}$  each.

### Detector

The HiStar detector is a two dimensional multiwire grid detector with pressurized xenon gas which enables us to determine the x- and y-positions of X-rays in its imaging area. Noble gas atoms are ionized by incident X-rays. These charged particles are attracted to and interact with an electrode assembly to produce electrical signals indicative of the x- and y-positions of the original X-ray. Provided the signal, after amplification, falls within a fixed pulse height window, the signal is finally positioned and produced as a 14-bit (0 to 16383) location in x and y. These 14-bit values are mapped to a frame pixel (0 to 1023). The diameter of the active area is 10.5 cm with a resolution of  $1024 \times 1024$  pixels [21].

---

beam and hence it does not disturb the normal XRD measurements. Furthermore the intensity is low because it comes from the continuous white *bremsstrahlung* near the  $K_{\alpha}$  line.

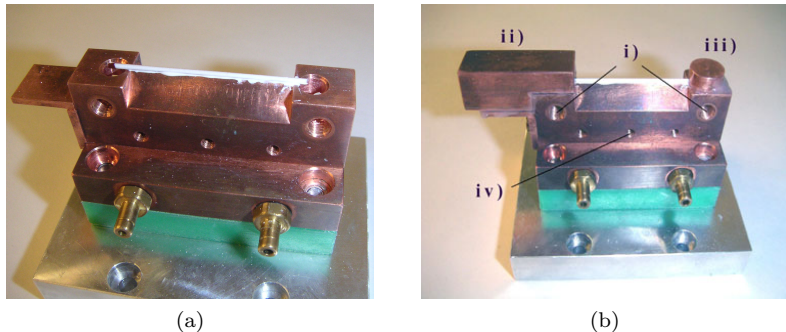


Figure 2.5: The glass capillary mounted on the sample holder consisting of, from bottom to the top, a mounting platform made of aluminium, a thermal isolator made of teflon and the copper block. (a) The capillary is glued on with thermal paste. (b) The chambers are sealed with silicon gel. The photograph pictures i) the channels through which the air with controlled humidity is circulated, ii) the dry chamber also containing grains of silica gel, iii) the humid chamber and iv) the point at which the indirect temperature of the sample is measured.

### 2.1.2 Sample holder

A custom made humidity- and temperaturecontrolled sample holder<sup>5</sup> was utilized in the experiment (figure 2.5). A glass capillary containing the sample was mounted with thermal paste on the sharp top edge of a copper block (Figure 2.5a).

Then a humidity gradient was imposed across the sample by exposing the two open ends of the capillary tube to closed chambers with different humidities, which were controlled by circulating air with controlled humidity through channels drilled through these chambers (Figure 2.5b). One end was kept at high humidity by circulating air above a saturated  $K_2SO_4$  solution, whereas the opposite end was kept dry by filtering air through a silica gel desiccant column (Figure 2.6). The relative humidity and temperature of the circulating air of both sides were measured by therma-hygrometers *prior* to passing through the chambers with the sample.

The temperature was controlled by water from a variable temperature heat sink circulating through interior channels in the lower part of the copper block and a temperature read of the copper block close to the sample using a thermistor sensor as an indirect temperature measurement of the sample.

### 2.1.3 Software

The SAXS software provided easy methods for pre-programmed scans of the sample. The built-in integration function included flat-field detector corrections and pixel sensitivity corrections. A script was written to integrate the entire frame range (see Appendix C).

Fit2D provided an easy way of finding the center of the beam, which is essential for unbiased integration of the frames.

<sup>5</sup>Modified version of the sample holder originally designed by *Bjørnar Sandnes* at the University in Oslo (UiO)



Figure 2.6: Setup of the circulating air; there are two systems, one for dry air passing through the blue silica gel, and one for humid air passing through the water solution of saturated  $K_2SO_4$ . Relative humidity sensors were placed close to the inlet air channels as a check on the imposed humidity gradient.

OriginPro 7.0 was among other things utilized for simultaneous updates of the water intercalation in the sample.

MatLab 7.0 was preferred to OriginPro 7.0 as the main tool for analysis due to its flexibility. Much time and effort was spent in order to comprehend and make full use of the program, but the result was several scripts easily adaptable to similar problems in likely future studies.

## 2.2 Experimental method

### 2.2.1 Clay sample

The clay sample was made from synthetic fluorohectorite (Corning Inc., New York) which had been subject to an ion-exchange process in order to produce a pure sodium fluorohectorite ( $Na - FH$ ) sample [33].<sup>6</sup>

---

<sup>6</sup>The raw material had been processed by dissolving clay powder in deionized water with subsequent stirring for several days. In order to make pure sodium fluorohectorite ( $Na - FH$ ) samples, an ion exchange method had been utilized.  $Na^+$  in the form of  $NaCl$  had been added to the clay suspension in an amount of approximately 10 times the interlayer charge. Due to the added salt, the suspension flocculated, and after stirring for about two weeks, the supernatant was removed. The flocculated clay was then placed in dialysis membranes, and excess ions were removed by dialysis where the deionized water was exchanged every second

To destroy the clusters of particles the powder was filtered and then thoroughly grinded in a mortar and filtered again. It is important to use the proper force when performing the grinding; too hard and the packing becomes anisotropic; conversely too loose and air filled voids arise in the sample which influence the diffusion process in an unwanted and uncontrolled manner.



Figure 2.7: Mortar and X-ray glass capillary used for the grinding and filling of the Na-fluorohectorite respectively.

Once grinded the clay powder was filled in an X-ray glass capillary<sup>7</sup> of length 80mm, outside diameter 1.0mm and wall thickness 0.01mm (Figure 2.7). The closed end of the capillary was cut, and the now dual open ended capillary was attached to the sample holder using a thermal paste (see Figure 2.5a). The distance from the X-ray exposed capillary to the physical capillary opening<sup>8</sup> was measured to be  $3.55 \pm 0.50\text{mm}$  and  $2.60 \pm 0.50\text{mm}$  for the dry and humid ends respectively.

The sample holder was mounted on the goniometer in the sample chamber thus enabling precise and reproduceable measurements in the  $xy$ -plane perpendicular to the incoming beam, and tubes for circulating air and for temperature control were properly connected. It is worth noticing that the circulating air could possibly introduce a pressure gradient between opposite chambers that in the worst case might influence the diffusion process. We did not have the proper equipment in order to measure the differential pressure, but not to enhance this effect and thus at least partly remedy the problem the pumps circulating the air were both set at an equally *low* frequency.

### 2.2.2 Scattering geometry

In a powder sample the particles are randomly orientated with respect to their angular distributions. Thus a fraction of the particles will have the correct

---

day. A check on this procedure was made by adding  $\text{AgNO}_3$  to detect possible  $\text{Cl}^-$  ions, which would precipitate as insoluble  $\text{AgCl}$ . The flocculated sediment was then heated for 6h at  $120^\circ\text{C}$  so as to remove its water content [7].

<sup>7</sup>Produced by *Hilgenberg*.

<sup>8</sup>The chamber copper lids effectively screen both ends of the capillary. See Figure 2.5.

orientation for Bragg scattering to occur. The scattering picture is a Debye-Scherrer cone with radius given as  $r \sin 2\theta$  (Figure 2.8), where  $\theta$  is the angle of incident with respect to the 001 orientation and  $r$  the sample to detector distance.

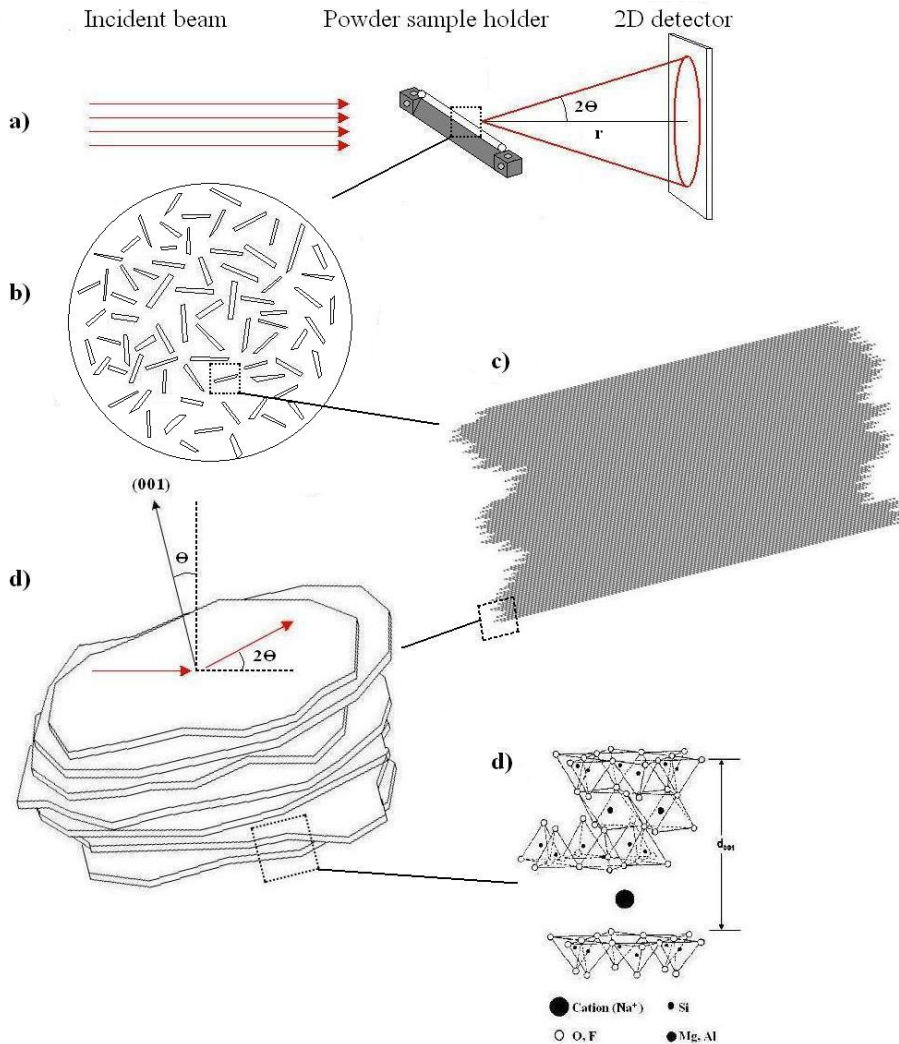


Figure 2.8: Schematic illustration of scattering geometry. a) The incident beam is scattered from a powder sample, where the particles are randomly orientated, thus resulting in a Debye-Scherrer scattering pattern on the 2D-detector. b) Cross-section of the capillary containing randomly oriented clay grains. c) Micron-scale clay particle formed from stacked lamellae. d) Layer configuration inside the particle grain. The angle between the incident beam and the 001 normal vector from a scattering particle is  $\theta$ , hence the scattering angle is  $2\theta$ . e) Generic structure of fluorohectorite synthetic clay.

The use of powder sample automatically implies that all the statistics are included in *one* scan frame, i.e. all particle shape and size variants as well as particle angular distributions.

### 2.2.3 Preparations

#### Setup settings

The sample position was detected with nanography (Figure 2.9).

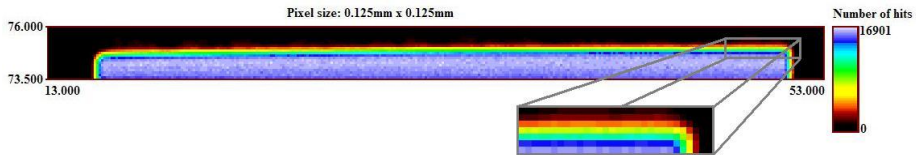


Figure 2.9: Sample nanography with equal  $x$ - and  $y$ -increments of  $0.125\text{mm}$  (note that this is less than the actual beam size dimensions (2.1.1 on page 47)) and a scan time of  $2\text{s}$ . The intensity is displayed as number of hits, and the dense sample region is recognized as the vertically green-, red- and yellow coloured stripes. The white-blue region represents empty air, whereas the black region is due to the copper device being poorly penetrable to X-rays.

The beam stop was properly adjusted with a horizontal and a vertical alignment screw. Then the beam center was found applying a sharp interference ring for a 1WL peak. These coordinates in terms of pixel numbering were set to  $(x, y) = (512.3, 506.4)$ .<sup>9</sup>

The pre-calibrated system was based on a different sample setting with a sample to detector distance of  $260.0\text{mm}$ . However, the sample in *this* experiment was  $\sim 1.5\text{mm}$  closer to the detector. The errors introduced were not big,<sup>10</sup> but in order to avoid unnecessary errors, a script was written to change the sample to detector setting in the heading of the raw data file in order for the subsequent integration to be correct.<sup>11</sup>

#### Pretest for 2WL

The start-up setting of the experiment required the sample to be in a pure 1WL hydration state. A pretest with the purpose of checking the sample for extra intercalated water was carried out at chosen sites in the sample (two at the

<sup>9</sup>Fit2D has a function that locates the beam center provided that three or more points on the circular arc can be defined. The beam center was found for several data frames, and the mean value was chosen as the correct center.

If the beam center is not properly set, the result will be smeared out and/or slightly shifted peaks. Thus sharp peaks of pure hydration states is an explicit indication of a correctly defined beam center.

<sup>10</sup>For the originally calibrated detector system we define the sample to detector distance  $a = 260.0\text{mm}$  and the corresponding detection spot height  $b$ , whereas for the *real* system we define the corresponding variables  $a' = 258.5\text{mm}$  and  $b'$ . Based on  $a$  and  $b$  the SAXS software calculates the scattering angle  $2\theta$  ( $\theta = \arctan\left(\frac{b}{a}\right)$ ). We note that  $b = b'$ . Then the *real*  $2\theta$  value is

$$2\theta' = \arctan\left(\frac{b'}{a'}\right) = \arctan\left(\frac{a}{a'} \tan 2\theta\right)$$

For  $2\theta \in [5^\circ, 8^\circ]$ , corresponding to the angular range for the mono- and by-hydrated peaks in our experiment, the subsequent errors would have been  $\Delta(2\theta) = |2\theta' - 2\theta| \in [0.0289^\circ, 0.0458^\circ]$ .

<sup>11</sup>Though we are primarily interested in the *dynamical* evolution of the peaks and not necessarily their correct numerical values.

beginning, two at the end and two in the middle). They all demonstrated pure 1WL Bragg peaks indicating no intercalation of additional water in the sample.

### Setting of scan variables

As a result of the accumulated intensity from test scans along with an estimated diffusion velocity based on [7], the measurement time was set to 20 minutes for each frame. This is close to a reasonable lower limit determined by the level of background noise. However, the demand for frequent scans weighed heavier than the wish for high resolution as the primary interest in this experiment was the *dynamics*. The interpositional increment<sup>12</sup> in lateral direction (along the capillary) was set to  $0.5\text{mm}$ .<sup>13</sup>

The scans were performed with the source settings of  $40\text{kV}$  and  $100\text{mA}$ .

### Initial reference scans

Reference diffraction scans, for later analytical application (Chapter 3), were taken at ambient temperature and humidity<sup>14</sup> while the sample state was pure 1WL, that is under equilibrium conditions.

#### 2.2.4 Scans

From experiments on hydration transitions in Na-FH [33] it is known that a significant volume of the clay sample resides in the 1WL intercalation state only for a small temperature interval between  $25^\circ\text{C}$  and  $40^\circ\text{C}$ . For lower temperatures the 2WL regime becomes more dominant. Thus the sample temperature was lowered to about  $\sim 15^\circ\text{C}$  while circulating dry air<sup>15</sup> at both ends. As for the stabilization of thermal equilibrium we waited about  $45\text{min}$  before imposing a humidity gradient by circulating humid air at one side. This moment marks the start of the experiment,  $t \equiv 0$ .

At the humid side water vapor starts to penetrate the sample by diffusing through the pore space between the clay particles. Thereby the pore space vapor concentration increases, and at some critical parametric values yet not fully understood a subsequent process of water intercalation into the particle's interlayer space is initiated. By studying the scattering profiles at different times and distances from the humid side of the sample the dynamics of the intercalation front can be traced.

The humidity control system and the temperature control system maintained the measured humidities,  $RH_{\text{dry}} = 0.307\%$  and  $RH_{\text{humid}} = 99.90\%$ <sup>16</sup>, and tem-

---

<sup>12</sup>The interpositional increment should as a minimum exceed the width of the beam.

<sup>13</sup>An alternative method would have been a scan time of for example 30 minutes and a positional incremental of  $0.75\text{mm}$

<sup>14</sup> $T_{\text{sample,initial}} = 30.2^\circ\text{C}$  and  $T_{\text{sample,end}} = 29.4^\circ\text{C}$

<sup>15</sup> $RH_{\text{dry}} \in [0.28\%, 0.31\%]$

<sup>16</sup>The immediate measurement at  $t \equiv 0$  read  $RH_{\text{humid}} 90.4\%$ . However, it took a good  $30\text{h}$  before the relative humidity stabilized at  $99.9\%$ . The time-weighted average is calculated with respect to the measurements subsequent to this, that is after circulating air humidity equilibrium is reached. Conversely, the time-weighted average for the *entire* period is  $RH_{\text{humid}} = 99.81\%$  with an uncertainty of  $\Delta RH_{\text{humid}} \in [-9.46\%, 0.14\%]$ .

perature,  $T_{\text{sample}} = 14.92^\circ C$  constant to within  $\Delta RH_{\text{dry}} \in [-0.032\%, 0.018\%]$ ,  $RH_{\text{humid}} \in [-0.05\%, -0.05\%]$  and  $\Delta T_{\text{sample}} \in [-0.32^\circ C, 0.33^\circ C]$ .<sup>17</sup>

**Terminating reference scan** At the end of the experiment a scan series was conducted for the entire positional range thus acting as a terminating reference scan. The dynamics at this state was extremely slow, which meant that assuming the reference series to be performed 'simultaneously' is an appropriate assumption.

### 2.2.5 Series

Three series of scans were conducted with 381, 404 and 1271 scan frames respectively. The two first series were terminated because of different reasons.<sup>18</sup> However, they both served as invaluable trials for properly adjusting the settings for the third and final experiment. Among other things different solutions for maintaining a fixed imposed humidity were tried, and important knowledge on the estimated intercalation speed was achieved. The two first series also function as control series of the data gathered in the third series, which is the fundament of the results here presented and subsequently referred to.

---

<sup>17</sup>The mean values were time-weighted averages, and the intervals were calculated as the differences between the mean and the two extremities of the series.

<sup>18</sup>The first experiment was terminated due to the holidays while the second was terminated due to maintenance of the NanoSTAR SAXS machine.

# Chapter 3

## Data processing, analysis and results

### 3.1 Data aquisition and processing

#### 3.1.1 Frames

The single scans were stored as *pixel frames* (Figure 3.1.1) with binary raw data as well as information on spatial- and timecoordinates in the frame header.

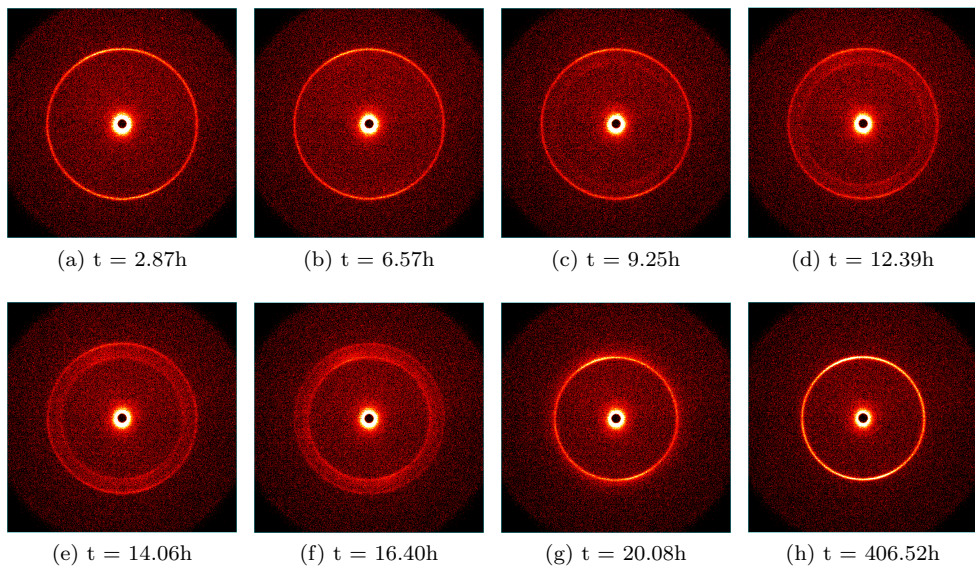


Figure 3.1: Photoseries of time-evolution of Debye-Scherrer scattering rings for  $x = 4.6\text{mm}$  into the sample. The time of the scan is given in the figure text.

### Unwarp

The SAXS software includes an integrated function called *unwarp* for essential corrections of the detected raw data. The two factors automatically corrected for are the (lack of) curvature of the detector as well as pixel sensitivity (some pixels are more sensitive than others).

### Spatial- and timecoordinates

From the frame header *xy*-coordinates and time and date of the scan were read and subsequently converted to spatial- and time coordinates for the sample frames;  $x \equiv 0$  was defined at the humid side of the capillary. The time coordinate for the individual scans was defined at the *middle* of the timescan.

#### 3.1.2 Integration

The pixel frames were radially integrated, that is with respect to conic line segments, utilizing the function *bin normalization*, which includes radial normalization (see 3.1.3) simultaneously to the integration process (Figure 3.1.2).

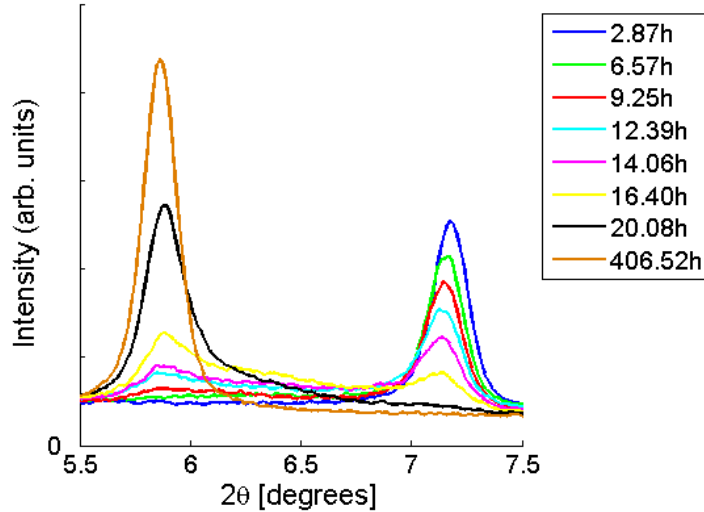


Figure 3.2: Radial integration of the raw data of the frames in Figure 3.1.1. Notice that the area of the pure 2WL peak is considerable larger than that of the pure 1WL peak. This is because of the scattering factors (layer structur factor and Lorentz-polarization factor) described in 1.2.8.

**Step size** The *angular step size* defines the interval between each integrated data point. The *detector* pixels are squared with sides of  $100\mu m$ . By geometrical considerations (Figure 3.3), a detector pixel covers an angular interval of

$$\Delta x = x_2 - x_1 = r(\tan 2\theta_2 - \tan 2\theta_1) \Leftrightarrow \tan 2\theta_1 = \tan 2\theta_2 - \frac{\Delta x}{r}$$

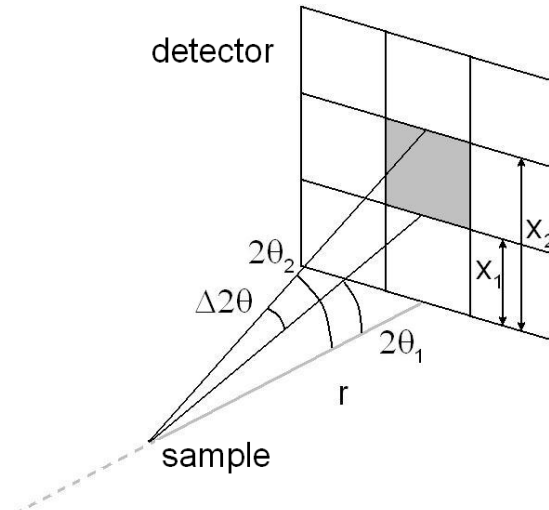


Figure 3.3: Each pixel in the pixel frame covers an angular interval of  $\Delta(2\theta)_{\text{pixel}}$ .

$$\Delta(2\theta)_{\text{pixel}} = 2\theta_2 - 2\theta_1 = 2\theta_2 - \arctan\left(\tan 2\theta_2 - \frac{\Delta x}{r}\right) \quad (3.1)$$

Thus for  $2\theta \in [2.0^\circ, 10.8^\circ]$ , we get  $\Delta(2\theta)_{\text{pixel}} \in [0.0214^\circ, 0.0313^\circ]$ .<sup>1</sup>

However, choosing the integration option *bin normalization*, the *bin* term permits us to set a lower step width without creating any additional noise. Thereby we define the integration resolution to be better than the detector resolution, but the software performs the necessary interpolation due to this inferior dectector resolution.

As the pure peaks are relatively narrow we would like as many integrated data points as possible for the subsequent curve fit (see 3.1.4) to be good. Therefore we set the step width to  $0.01^\circ$ .

### 3.1.3 Normalization

#### Radial normalization

When integrating pixels along a conic line segment (see 3.1.2), each pixel may be weighted by a normalization factor. This is due to geometrical considerations inferred from when integrating a raw data frame radially, the intensity with respect to the angular value,  $2\theta$ , is necessarily proportional to the circumference of the conic segment,  $2\pi r \sin(2\theta)$  (where  $r$  is the sample to detector distance (see Figure 3.3)). Thus the normalization included in the software integration function basicly divides each conic segment (as a function of  $2\theta$ ) by  $\sin(2\theta)$ .

#### Background subtraction

A background scattering, decaying with increasing angle, is clearly visible in the integrated frame plots. Small-angle scattering from the clay is expected.

---

<sup>1</sup>The lower limit corresponding to  $2\theta = 10.8^\circ$  and  $\Delta x = 100\mu\text{m}$  and the upper limit corresponding to  $2\theta = 2.0^\circ$  and  $\Delta x = \sqrt{2100}\mu\text{m}$  (for the diagonal of the pixel).

Variations in the background shape and intensity, both with time and spatial coordinate, is evidence of contributions beyond the clay itself. These are assumed to be primarily due to scattering from non-vacuum air and from the glass capillary. Also the amounts of water in the clay may affect the background scattering. Furthermore scattering from the copper sample holder is also possible in some cases, depending on how the sample holder is adjusted with respect to the beam.<sup>2</sup>

Small-angle crystal scattering is known to follow a power-law, thus resulting in asymmetrical peaks especially visible for broader peaks. Thereby we assume the collected contributions to follow a small-angle scattering. Because of time- and spatial background variations, a background power-law-fit is performed for each frame over an angular interval sufficiently far from the Bragg peaks (Figure 3.4a), typically  $2\theta \in [2.0^\circ, 3.8^\circ] \cup [8.5, 10.8]$ ,<sup>3</sup> and the result is subtracted from the raw data (Figure 3.4b) thus removing the unwanted background noise.<sup>4</sup>

#### Layer structure factor and Lorentz-polarisation factor corrections.

As discussed in 1.2.8 and 1.2.9 there are several contributing factors to the total recorded scattering intensity. According to Equation (1.34) these are the layer structure factor, the Lorentz-polarization factor and the interference function. The interference function is directly related to the interlayer spacing through Equation (1.32). The dynamics in the water intercalation front is thus reflected in the dynamics of the interference function. In other words the interference function is the essential function we wish to extract.

Hence we divide the recorded data, now integrated, normalized and background subtracted, by the product of the layer structure factor and the Lorentz-polarization factor (Figure 3.5). In 1.2.10 these factors were obtained as functions of the scattering angle,  $2\theta$  (and energy,  $\lambda$ ).

#### 3.1.4 Peak fitting

The data processing up till this point has exclusively been in order to 'purify' the recorded signal from unwanted contributions (radial normalization, background scattering and scattering factor contributions); the remaining data represent the *extracted interference function* (1.2.8), a direct implication of the interlayer spacing between the crystalline platelets. As the water intercalation proceeds, this interlayer spacing will increase as water molecules drive the sheets apart. Thus the diffraction rings will, by Bragg's law, shift towards lower angles (increasing basal distance  $d$ ).

We observed that during hydration scattered intensity appeared between the commensurate Bragg peak positions (see Figure 3.4a). This is a well-known signature of disordered intercalation or mixed intercalation along the stacking direction and will be closer investigated in 3.2.4. However, the preliminary main goal is to fit a function to the hydration *peaks*, which represent diffraction signals

---

<sup>2</sup>Remember that the height of the core beam is 0.8mm (2.1.1). Thus in cases of poor vertical alignment of the sample holder it is possible that a tiny fraction of the beam is actually deflected from the sharp copper holder edge along which the sample is mounted, although most of the beam hitting copper will be absorbed.

<sup>3</sup>These intervals are easily determined through a semi-log plot of the normalized curve plot.

<sup>4</sup>One could also do a linear fit around the baseline of the Bragg peaks. This is possible due to the widths being *narrow*. However, improved accuracy is achieved by fitting to a power-law.

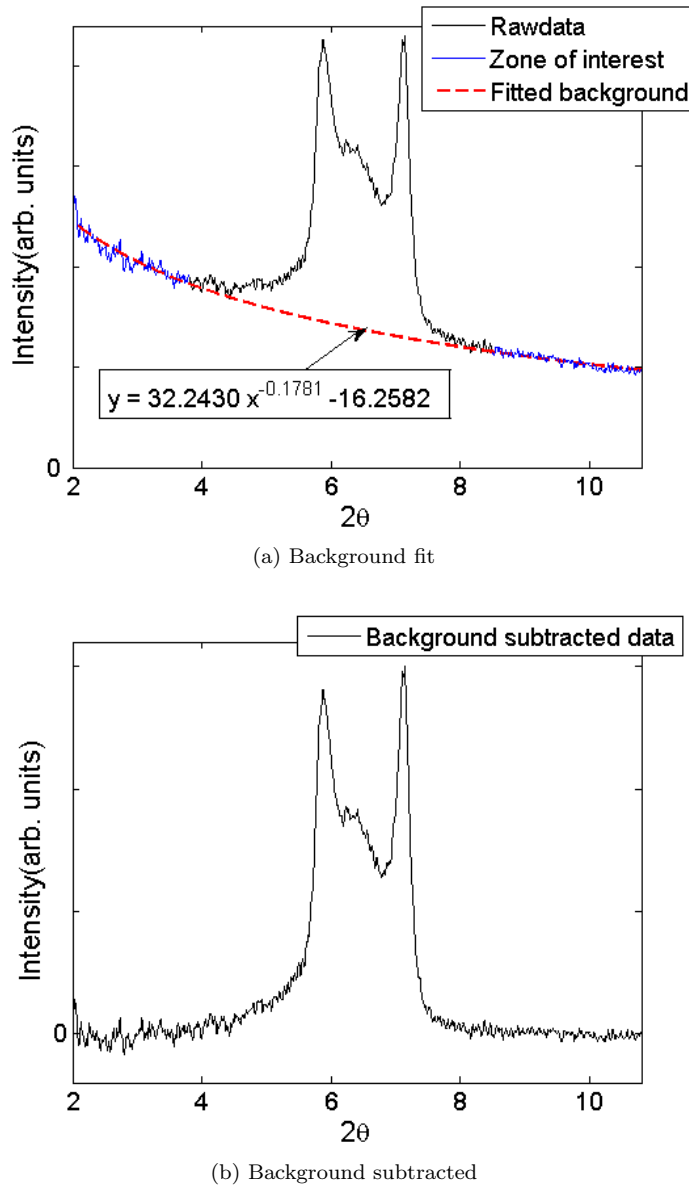


Figure 3.4: The background noise is fitted to a power-law and subtracted from the data. (a) Background fit of an arbitrary chosen scan frame. The fit is based on the angular interval (blue curvature) assumed to only inhibit unessential (that is *not* due to the interlayer spacing) scattering contributions, which means sufficiently far out from the Bragg peaks as well as the interpeak hydration transition interval where scattering from the clay is known to be considerable. (b) The fitted background subtracted from the same scan frame. We observe that for low angles the noise is considerable, but this angular interval is no longer important for the further analysis. Also observe a *slight* change in symmetry of the peaks (more symmetric).

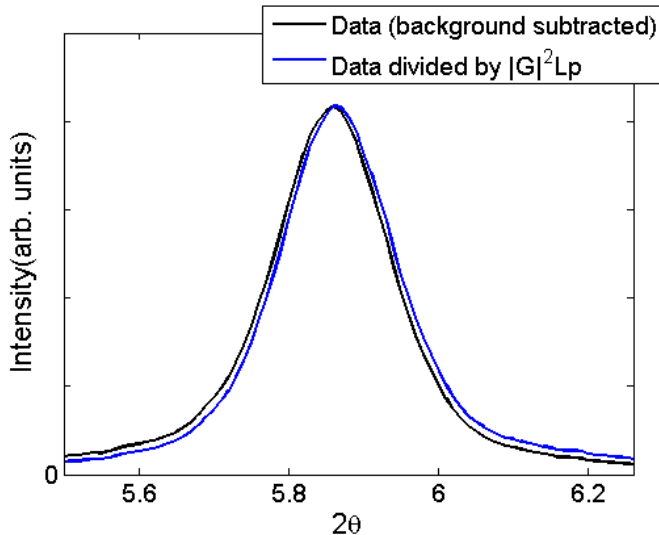


Figure 3.5: Division of the background subtracted data by the layer structure and Lorentz-polarization factors from an arbitrary scan frame displaying a pure 2WL state. The graphs have been scaled in order to coincide. Note how the layer structure and Lorentz-polarization factors slightly shift the symmetry of the peak. The layer structure factor differ from one hydration state to another, but only by a fraction for small scattering angles (see also Figure 1.18).

from crystallites of pure hydration states. Thus we are able to estimate the *area* of each peak, which we take to represent the amount of crystallites in pure hydrations states. The crystallites of mixed intercalation we do not consider for the time being.

The diffraction peaks are fitted with a pseudo-Voigtian peak shape function (see 1.4). Under some restrictions, the fitted design variables are the shape factor ( $\eta$ ), peak position ( $x_c$ ), peak width ( $\omega$ ) and peak area ( $A$ ) (Equation (1.56)).

The degree of goodness of a fit to a large extent depends on the chosen angular interval on which to do the function fit. For a scan frame displaying mixed hydration states, thus implying both a 1WL and a 2WL peak (as well as a disordered intercalation transition region between the peaks), it is necessary to do the fitting on the 'pure' peak side; for the case of a 1WL peak this corresponds to doing the fit on the datavalue mainly to the right of the Bragg peak, and conversely for the 2WL peak fit. This is because of the mixed hydration signals between the peaks, mainly originating in Hendricks-Teller states, interfering the recorded pure peaks by inflicting an asymmetrical peak shoulder on the same side as the mixed intercalation region.<sup>5</sup>

On the other hand, for a *pure* hydration state and thus a symmetric, well-defined peak, a fit over the entire angular interval would be preferred. Thus the ideal situation would be to define each peak on basis of its shape; a fit over only half of the interval for a biased peak, whereas over the entire interval for a

---

<sup>5</sup>The tails of the transition region coincide with the peaks thus adding to the signal.

pure peak. However, this would demand for a visualization of each peak, which would be too time-consuming given the number of frames to be integrated. Instead fixed fitting intervals, one for each hydration state, were determined for all frames on basis of a MatLab script especially designed for this purpose. The 1WL peaks were fitted for  $2\theta \in [0.075^\circ, 0.5^\circ]$  around the peak position, the 2WL peaks for  $2\theta \in [0.3^\circ, 0.075^\circ]$ .

Another MatLab script<sup>6</sup> was made for fitting the data to a pseudo-Voigt function. This script (see C) returned the values of the fitted design variables along with the corresponding errorbars and residual of the fit.

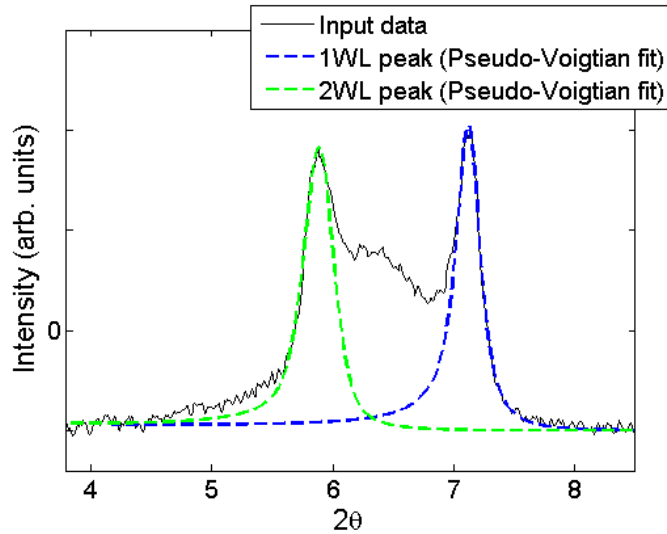


Figure 3.6: Pseudo-Voigtian peak fit on the 1WL and 2WL peaks of Figure 3.4b. The structure factors have been multiplied with the fitted peaks for comparison reasons (remember the different structure factors for different hydrations states).

Every frame was thus automatically fitted and the parameters written to a file.

---

<sup>6</sup>Originally designed by Yves Méheust, but a considerably modified and extended version was programmed for this purpose.

## 3.2 Data analysis

In this section the interference function extracted in 3.1 is subjected to closer examination. Basically by representing the data in various perspectives and with different relations, a picture of the dynamic process of water intercalation through the sample related to hydration vapor diffusion may be formed.

First some general observations will be investigated before concentrating on the analysis of the diffusive process.

### 3.2.1 General observations

#### CHARACTERISTIC BRAGG ANGLE AND INTERLAYER SPACING

To measure the characteristic Wide-Angle X-ray Scattering (WAXS) peak, better known as the Bragg angle, of the mono- and bi-hydrated states, *pure* hydration peaks of complete equilibrium were considered. For the monohydrated states the initial reference scans (2.2.3) were utilized for the calculations, whereas the first reference endscans (2.2.4) were used for the bi-hydrated case.

The mean characteristic 1WL peak was found at  $2\theta_{\text{mean}}^{\text{1WL}} = (7.225 \pm 0.006)^\circ$ . Conversely, the mean 2WL peak was at  $2\theta_{\text{mean}}^{\text{2WL}} = (5.869 \pm 0.004)^\circ$

**d-spacing** The interlayer spacing is directly related to the characteristic peak value through Bragg's law (1.2); the corresponding mean *d*-spacing is  $2\theta_{\text{mean}}^{\text{1WL}} = (12.23 \pm 0.03)\text{\AA}$  and  $2\theta_{\text{mean}}^{\text{2WL}} = (15.06 \pm 0.01)\text{\AA}$  respectively.<sup>7</sup>

**Thermal expansion coefficient** Initially a slight shift in center peak values was observed for the initial reference scans compared to the scans taken during the experiment. Peak shifts of pure states may origin in thermal expansion; when the crystallites cool down, the thermal activity decreases, and consequently so do the interatomic spacings, thereby reducing the size of the crystallite.

The thermal expansion coefficient,  $\alpha$ , can be defined as

$$\alpha = \frac{\Delta d}{d} \quad (3.2)$$

and by Bragg's law (Equation (1.2)) we deduct an expression for this particular case

$$\begin{aligned} d_{hkl} \sin \theta &= \frac{n\lambda}{2} = \text{const} \\ \frac{d}{dd_{hkl}} (d_{hkl} \sin \theta) &= \sin \theta + d_{hkl} \cos \theta \frac{d\theta}{dd_{hkl}} = 0 \\ \alpha &= -\frac{\Delta \theta}{\tan \bar{\theta}} = -\frac{(\theta_{T_{\text{room}}} - \theta_{T_{\text{experiment}}})}{\tan \left\{ \frac{1}{2}(\theta_{T_{\text{room}}} + \theta_{T_{\text{experiment}}}) \right\}} \end{aligned}$$

However, the thermal expansion coefficient for similar specimens are of order  $10^{-6} \text{ K}^{-1}$ , corresponding to an angular shift in  $2\theta \sim 10^{-6} \text{ }^\circ \text{K}^{-1}$ . Thus thermal expansion in this temperature and angular range as the cause of visual peak displacement can be rejected.

<sup>7</sup>This is within  $0.1\text{\AA}$  or less than  $0.1^\circ$  of the corresponding values found in [7].

**Peak displacement** A more thorough investigation of the peak displacement was carried out.

For sufficiently pure monohydrated peaks, where the function fit is assumed to be very good, a small displacement of the fitted characteristic angle systematically decreasing with positional distance, was observable (Figure 3.7a). Assuming that the degree of intercalation is a function of the surrounding relative humidity, this displacement shows the presence of humidity and subsequent initialization of the intercalation process, but only by a fraction not yet detectable by the shape of the scattering curve.

The plot of the characteristic angle displacements of the reference end scans and comparison to those of the initial reference scan (Figure 3.7a) reveals the ingress of humidity practically through the entire sample by the end of the experiment. The more interesting *d*-spacing counterpart of this plot (Figure 3.7b) shows this displacement to be of order  $(10^{-2} - 10^{-1})\text{\AA}$ .

The humidity gradient is expected to evolve with time towards a linear function with humidity values at the capillary ends equal to that of the corresponding humidity 'reservoirs' (one humid and one dry). However, the elapsed time for this humidity gradient to 'stabilize' linearly is related to the water vapor diffusion through the sample and therefore one of the subjects of this experiment.

In the same figure the curve of the end scan peaks approaches that of the initial reference scan peaks at an almost evenly rate, and the two curves *collapse* close to the far end (dry side). The point of collapse probably indicates the humidity front, at least very close to this. This is approximately at  $x \sim 35\text{mm}$ . Knowing the sample capillary to be  $\sim 42\text{mm}$ , this means that the humidity has regressed almost through the entire sample, and that the gradient soon is linear. At this point, however, it is not yet linear, but very close, which explains for the extremely slow dynamics.

It is important to underline that the above reasoning assumes that the degree or rate of intercalation is a function of the surrounding relative humidity, and that a certain threshold relative humidity has to be reached in order for a certain *proportion* of a representative sample volume to intercalate. One possible way of explaining this is by assuming that the relative humidity determines the amount of water molecules that intercalates into the interlayer spacing, but that for a given interval of low relative humidities these molecules do *not* form a new layer. Instead the lack of favourable molecule positions force the additional molecules to position themselves in such a way that the interlayer spacing is slightly shifted (increased), but not enough for a new hydration layer to be created.

For the formation of a new water layer, implying a reorganization of the layer structure of water molecules, a certain threshold relative humidity limit has to be reached, beyond which the intercalation is 'fast' as well as intense compared to the slow percolation behaviour of the small displacements.

Provided that this is true, peak displacement actually allows us to demonstrate humidity ingress, at least to some extent. Furthermore, the slowing down of the humidity ingress (described by the 'pure peak displacement') can be explained by the humidity gradient approaching linearity, whereas the fading of the intercalation front is due to a threshold limit. This matter will be discussed further in subsection 3.3.

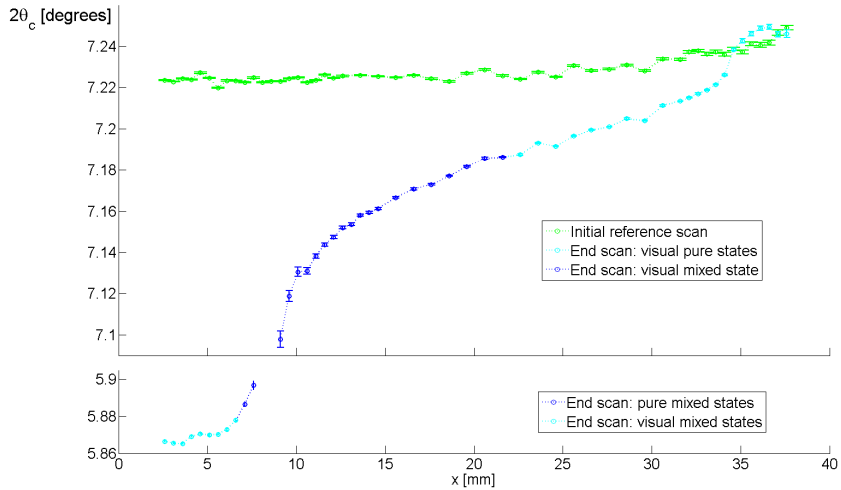
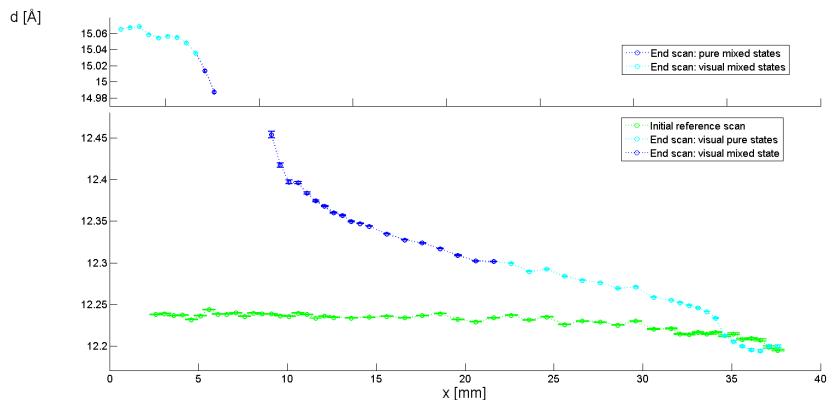
(a)  $2\theta$  plot(b)  $d$ -spacing plot

Figure 3.7: Monohydrated peak displacement. The plot shows a comparison of the initial reference scan (green line) to the end reference scan (blue line) of the monohydrated case. The end reference 2WL peaks are also plotted in the same graph.

The fitted 1WL peak center is slightly displaced. Towards the intercalation front ( $x \sim 9\text{ mm}$ ) this displacement is considerable (dark blue) and is detectable in a log plot of the Bragg scattering curve, whereas the shift decreases with increasing sample position eventually to disappear as the two curves *collapse* for the remaining last part of the sample. For these last scans (light blue) the shift is not observable in a log plot.

For the 2WL case a corresponding shift is seen for the peak center. The meaning of the colour code (dark and light blue) is equal to above.

All the data points of each set respectively are assumed to be recorded under the same conditions (see 2.2.4). (a) The angular displacement is of order  $10^{-2}^\circ$  (b) The corresponding  $d$ -spacing displacement is of order  $(10^{-2} - 10^{-1})\text{\AA}$

Moreover, a similar displacement, but towards higher angles, was shown for the 'pure' dihydrated peaks (lower part Figure 3.7a). By the same arguments

this displacement may be caused by slow intercalation, sensitive to the relative humidity, not altering the hydration state, but only slightly displacing the interlayer distance.

#### PEAK WIDTH

**Instrumental contribution** Let the distance from the Göbel mirrors (Figure 2.3) to the beam defining pinhole (2<sup>nd</sup> pinhole) be denoted  $s$  and the diameter of the pinhole (Figure 2.4) be denoted  $D$ . Then by simple geometrical considerations (Figure 3.8a) the maximum angular divergence  $\varphi$  caused by the property of the X-ray mirror and/or property of the 'point' focus X-ray source (see 2.1.1) to the effective core beam is

$$\varphi = \arctan\left(\frac{D/2}{s}\right) \in \pm[0.0098^\circ, 0.0112^\circ]$$

which corresponds to an angular divergence,  $\Delta(2\theta) = \Psi - 2\theta$ , in the characteristic Bragg peak (Figure 3.8b) where

$$\Psi = \arctan\left(\frac{d_1 + d_2}{l_2}\right) = \arctan\left(\frac{l_2 \tan(2\theta + \varphi) + l_1 \tan \varphi}{l_2}\right)$$

For the pure monohydrated state the induced peak broadening due to this instrumental effect is  $\Delta(2\theta)_{1WL} \in \pm[0.0728^\circ, 0.0770^\circ]$ , whereas for the bi-hydrated state the corresponding peak broadening is  $\Delta(2\theta)_{2WL} \in \pm[0.0731^\circ, 0.0774^\circ]$ .<sup>8</sup>

Additionally, a further broadening is caused by the non-monochromatization of the beam (leading to other scattering angles by Bragg's law) and by parasitic edge scattering from the pinholes. However, these contributions are significantly inferior to the above discussed instrumental peak broadening with respect to intensity/and or size.

The intensity of the non-monochromatic and/or non-collimated parasitic radiation is much lower than the effective core beam when a monochromatizer and collimators (mirrors and 3-pinhole collimation system) are used. Thus, the peak broadening deduced above is only suited for estimating the order rather than the exact numerical value of this effect.

**Sample contribution** Let  $b$  define the width of the beam,  $c$  the diameter of the sample capillary and  $l$  the distance from the capillary to the detector (Figure (3.9)). Then the angular divergence,  $\Delta(2\theta) = \Psi - 2\theta$ , in the Bragg peak due to the beam and sample width is given

$$\Psi = \arctan\left(\frac{d + b}{l}\right) = \arctan\left(\frac{(c + l) \tan(2\theta) + b}{l}\right)$$

leading to an angular divergence of  $\Delta(2\theta)_{1WL} = \pm 0.1149^\circ$  and  $\Delta(2\theta)_{2WL} = \pm 0.1103^\circ$  for the monohydrated and bi-hydrated states respectively.<sup>9</sup>. These

<sup>8</sup>Where it is assumed that  $2\theta_{1WL} = 7.13^\circ$  and  $2\theta_{2WL} = 5.84^\circ$

<sup>9</sup>Assuming that  $2\theta_{1WL} = 7.225^\circ$  and  $2\theta_{2WL} = 5.869^\circ$

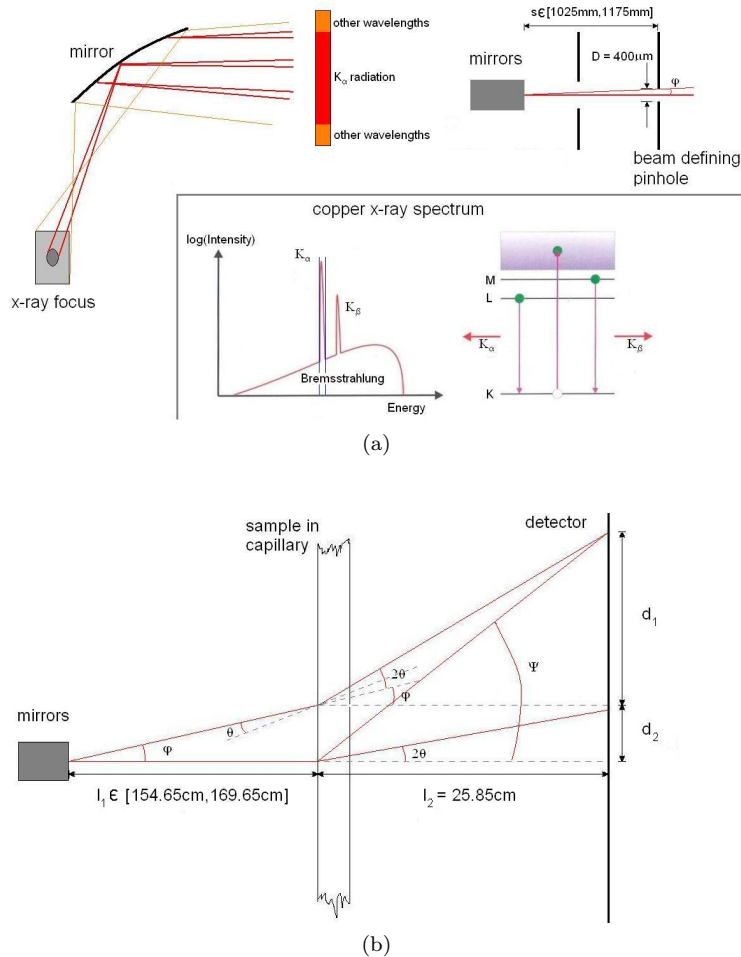


Figure 3.8: Instrumental peak broadening. (a) The upper schematics show radiation divergence due to 'point' source and finite pinhole size (leading to a non-collimated beam) and non-monochromatized beam. The bottom right schematics illustrate that because of the relatively large focus not only  $K_{\alpha}$  radiation is Bragg reflected by the mirror, but also a small 'parastitic' wavelength interval from the generated X-ray spectrum. (b) Geometrical considerations for evaluating the  $2\theta$  angular divergence,  $\Delta(2\theta)$ .

results also indicate the order rather than the exact numerical value of the peak broadening.

**Calculated values** The Gaussian and Lorentzian components of the peak width,  $\omega_G$  and  $\omega_L$ , are deductible from the fitted design parameters peak FWHM,  $\omega$ , and shape parameter,  $\eta$ , (see 1.4.5, especially Equation (1.57)). The linewidth of the Gaussian component is generally attributed to the instrumental resolution [7].

A representative selection of the initial reference scan yields  $\omega_L^{1WL} = (0.11 \pm 0.2)^\circ$  and  $\omega_G^{1WL} = (0.13 \pm 0.2)^\circ$ , whereas a selection of the reference end scans

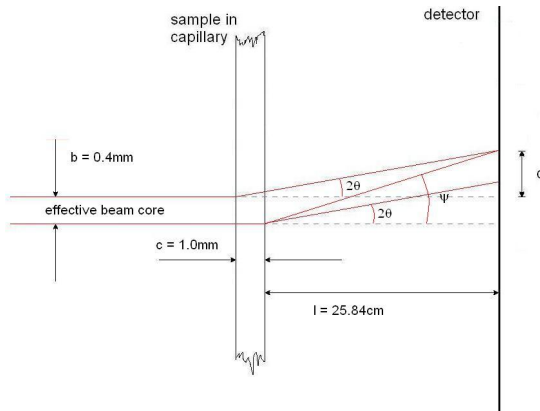


Figure 3.9: Sample peak broadening. The finite widths of both the beam as well as the sample capillary lead to scattering from a representative sample volume rather than from the ideal sample 'point'. Thus the recorded signal is a mixture of divergent contributions from several small scattering volumes leading to a peak broadening; if one follows the extremes of the initially collimated beam (red lines) one observes by simple geometrical considerations possible scattering alternatives of volume elements of identical state. Allowing for partial scattering volumes of different states, the broadening may be even larger.

correspondingly gives  $\omega_L^{2WL} = (0.12 \pm 0.1)^\circ$  and  $\omega_G^{2WL} = (0.11 \pm 0.1)^\circ$ .

The fitted values of both the instrumental and sample induced broadening are of the same *order* (and almost same value) as the theoretical roughly estimated values. Consequently the agreement is good.

#### AVERAGE PARTICLE SIZE

By knowing the FWHM related to particle contribution, the Scherrer equation (Equation 1.36) can be used to give an estimate of the average particle size. In our case, utilizing the data from the initial reference scan and taking the Lorentzian peak width,  $\omega_L$ , to represent the sample width, the mean crystallite dimension along a line normal to the reflecting plane is found to be  $(0.064 \pm 0.029)\mu m$ . This is of the correct order, but still a bit too low compared to the expected value of  $\sim 0.1\mu m$  from other studies (for instance [7]).

This discrepancy can be due to the existence of *microstrain*. If so, the Scherrer equation can be amended to include a strain description [47]. The pure sample broadening includes both size and strain broadening and is easily given as the sum of the two

$$\omega_{\text{size+strain}} = \omega_{\text{size}} + \omega_{\text{strain}}$$

where  $\omega_{\text{strain}} = \zeta \tan \theta$  and  $\zeta$  being the strain. Microstrain thus generally increases the FWHM as a function of  $2\theta$ . Applying the strain value of 0.57% for the bulk found in [7] and subtracting the strain contribution from the total FWHM, the expected particle size is corrected to  $(0.077 \pm 0.044)\mu m$ . This corresponds to about  $\sim 63$  fundamental silicate lamellae in an average crystallite.

In [6] particles of 20 – 100 layers are reported.

However, it is also probable that  $\omega_L$  includes other contributions thus leading to a too low particle thickness estimate.

### ANISOTROPY

The powder sample is composed of originally randomly distributed particles and therefore assumed to be isotropic. However, the sample may be influenced to prefer directional alignment thus displaying a larger degree of anisotropy. This is mainly attributed to clay synthesis and packing effects.<sup>10</sup> A check on this matter was investigated for scans taken at equal positions. The results revealed a slight degree of anisotropy varying with sample position. However, no large changes in time signifying altering due to for example water vapor or clay swelling may be demonstrated.<sup>11</sup>

Figure 3.10 shows a typical plot<sup>12</sup> for an arbitrary chosen position known to have been passed by the intercalation front in the last scans. Note how the anisotropic distribution is consistent with time (represented by different recorded series).

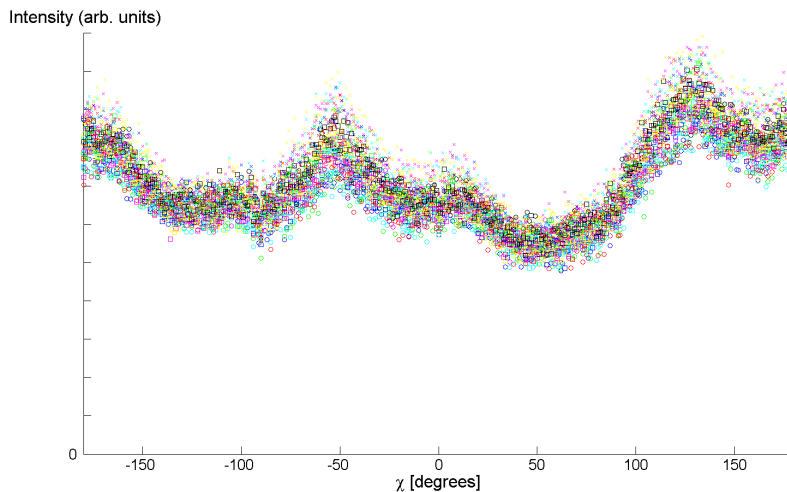


Figure 3.10: Sample anisotropy at  $x = 6.6\text{mm}$ . Note that the sample volume is slightly anisotropic. However, the different scans (represented by the variations of colour and symbol markers) demonstrate no significant change to this anisotropy with time.

---

<sup>10</sup> Anisotropy can be caused by water intercalation into the sample crystallites. This intercalation may also inflict changes in the mesoporosity.

<sup>11</sup> Any changes with time would probably only lead to subtle changes in the anisotropy not detectable in this experiment.

<sup>12</sup> As opposed to integrating radially for obtaining the intensity we integrate around the Debye-Scherrer interference rings and plot the intensity as a function of the angular increment.

### 3.2.2 Dynamics of water intercalation

In this part of the analysis the dynamics of the water intercalation front is examined. The intercalation front advances in space with time and thus changes the diffraction profiles from a fully developed pure monohydrated Bragg peak via mixed intercalation states to a fully developed pure bi-hydrated Bragg peak. This evolution may be visualized by fixing either the time or the spatial coordinate and varying the other.

**Evolution in time of (001) Bragg peaks** Figure 3.11a and 3.11b display the evolution in time of the diffraction signals recorded over a limited angular interval. The signals are not processed beyond the simple integration of the raw data (and the radial normalization implied therein).

We observe how the alternating  $d$ -spacing with time due to the intercalation of water changes the peak form and position; the 1WL peak decreases on behalf of the increasing 2WL peak. Also states of mixed order are observed between the peaks. These will be discussed in 3.2.4.

**Evolution in space of (001) Bragg peaks** Another way of visualizing the dynamics is by varying the spatial coordinate while 'fixing' the time coordinate, that is restricted to a *small* time interval. The slower the dynamics, the larger the time interval can be. This is because for a 'fixed' time coordinate we assume the scans to be referred to a single time coordinate, which is possible only where there has been no significant change in the normalized hydration intensities within this very interval.

Figure 3.12a and 3.12b display the evolution in space of the diffraction signals.

**Normalization of the hydration peaks** As noted in the figure text of Figure 3.12b, differences in the background contributions scale the intensities of the Bragg diffraction scattering unevenly from position to position. Thus a normalization of the intensities is essential for a proper comparison of the dynamics at *different* positions.

Assuming that the *area* of the pure peaks (mixed hydration contributions neglected) reflects the ratio of the total scattering volume to exist in such a purely hydrated state, we normalize the fitted areas of the hydrated peaks by the area of a *fully developed* pure peak state meaning no random intercalation present; for the monohydrated case the initial reference scans of fully developed 1WL peaks were taken as normalizing reference, whereas for the bi-hydrated peaks the first of the end reference scans, known to be fully developed 2WL, were used as normalization reference.

Only the first positions along the sample had undergone a complete transition from a fully developed pure 1WL state to a fully developed pure 2WL state during the experiment. For these the ratio between the reference areas of different hydration states are given in Figure 3.13, and the mean value, hereafter referred to as the '*peak factor*', was found to be  $\sim (0.696 \pm 0.042)$ . The peak factor should equal unity as the calculation is carried out on basis of the normalized interference function.<sup>13</sup> This misfit may indicate that our calculated

---

<sup>13</sup>The area of the peaks of the interference function are all equal to unity (see Equation

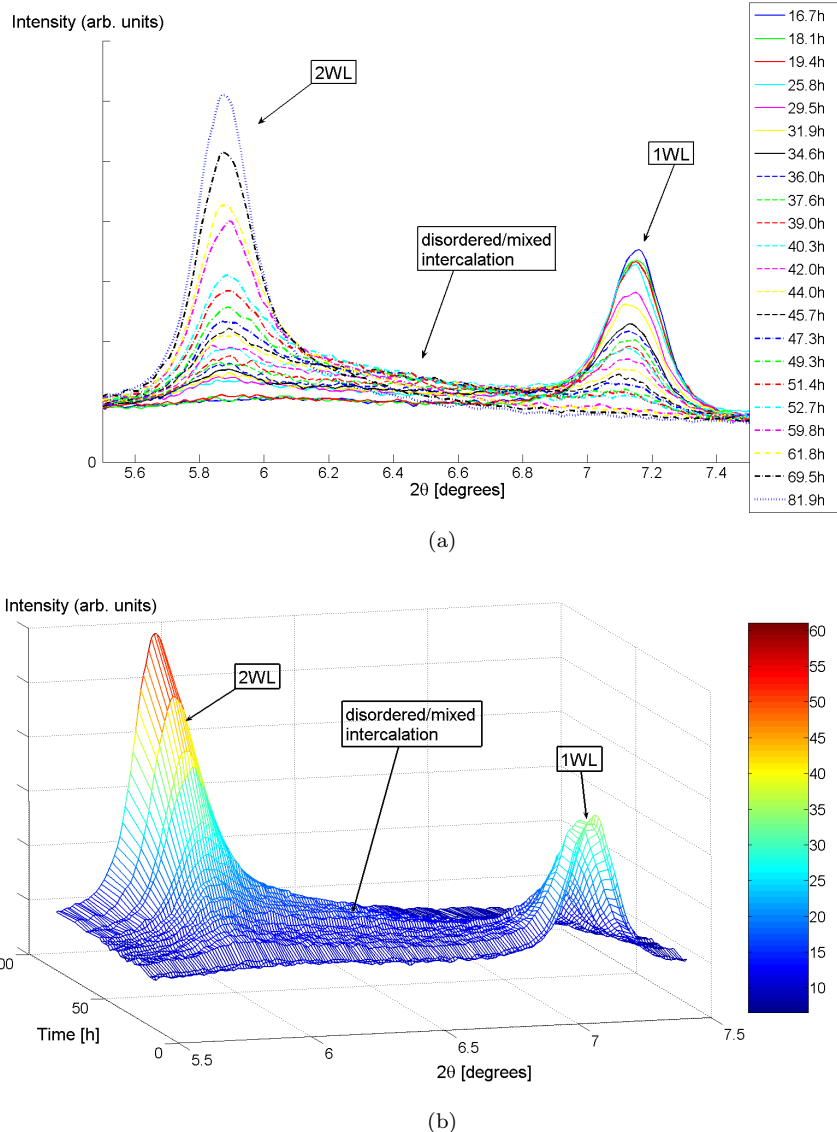


Figure 3.11: Time evolution of the (001) Bragg diffraction curves for fixed position coordinate  $x = 7.1\text{mm}$  over the limited angular interval of  $2\theta \in [5.5^\circ, 7.5^\circ]$ . (a) A traditional 2D representation of the diffraction curves. The time of the scans are tabulated in the text box. (b) A 3D representation of the diffraction curves. The introduction of the time dimension in the plot emphasizes the dynamics in the evolution and consequently the rate of the transition.

squared layer structure factor (see 1.18),  $|G|^2$ , is slightly displaced to the left. A correction shift to the right implies that the relative  $|G|^2$ -factor decrease is greater for the 2WL-peak compared to the 1WL-peak.<sup>14</sup>

(1.33)) independent of the  $d$ -spacing.

<sup>14</sup>Notice how much a tiny displacement in the  $|G|^2$ -factor changes the relative normalization factor of the 2WL-peak compared to the 1WL-peak. The reason is simply that the gradient

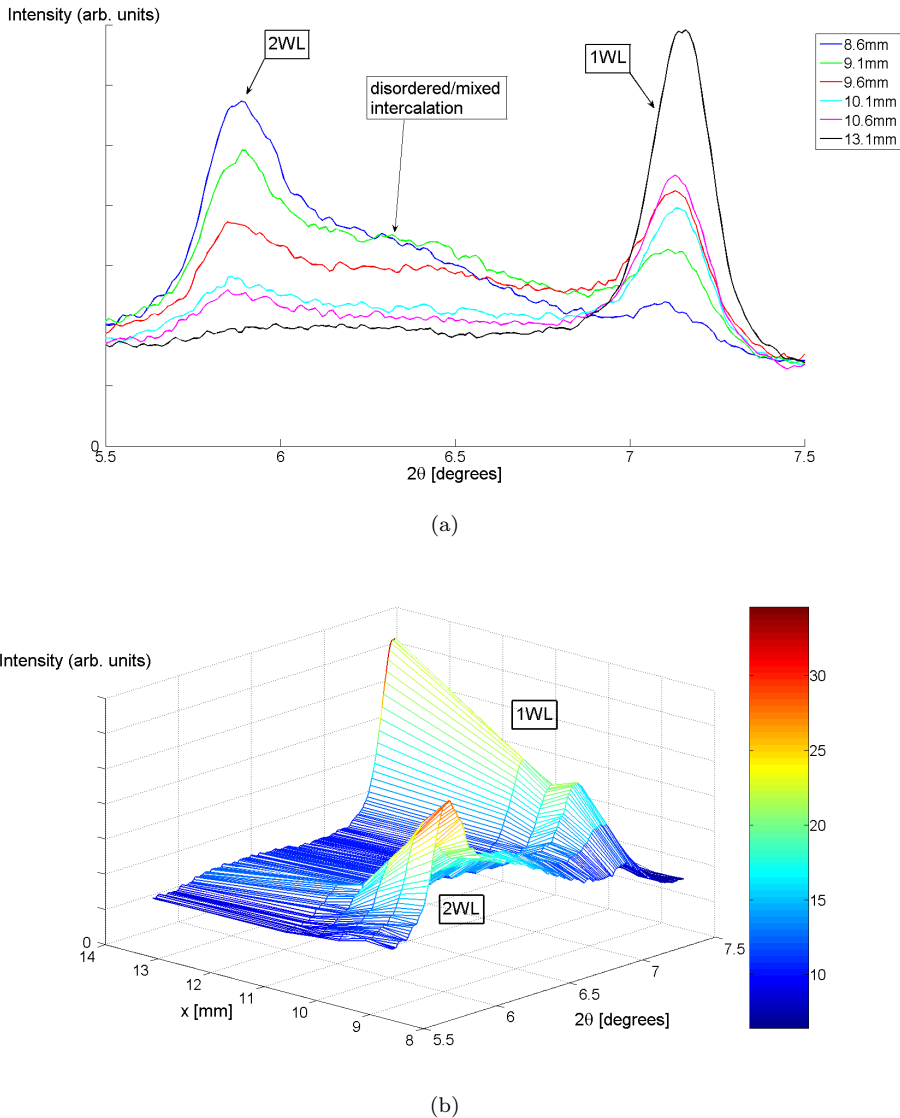


Figure 3.12: Spatial evolution of the (001) Bragg diffraction curves for 'fixed' time coordinate  $t = (348.5 \pm 1.0)h$  over the same limited angular interval of  $2\theta \in [5.5^\circ, 7.5^\circ]$ . (a) In the experiment the intercalation front was followed closely. Thus the scans include significant disordered contribution in the commensurate Bragg peak area. This is evident by the 2D representation. (b) In the 3D representation there seems to be an abnormality in the incline of the 1WL peak height (this is also seen in the 2D representation by close investigation). However, this is simply because the graphs are not normalized, and as mentioned in 3.1.3 the scans inhibit different amounts of background contributions, thus varying the intensity heights of the peaks. Conversely, by studying the peak *shape* of the 1WL peak around the *apparent* deviation, the 'normality' of the spatial evolution is restored.

---

is significantly larger for smaller  $2\theta$  angles in this range.

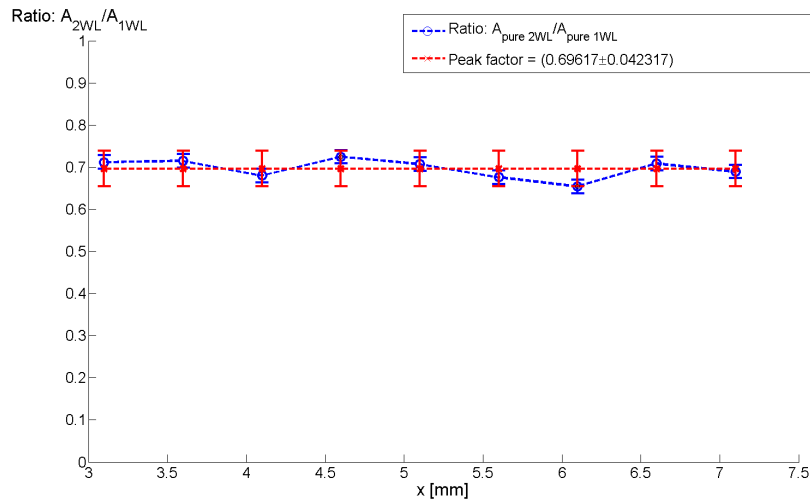


Figure 3.13: Determination of the peak ratio of pure hydration states applied for normalization.

However, this disagreement is *not* likely to concern the matters discussed here in any considerable way as we are focusing on the *dynamic behaviour* in preference to comparing the descriptive parameters of the *different* hydration states

In the case of the remaining bi-hydrated scans, for which there exists no fully developed pure bi-hydrated peaks as reference, the peak ratio was utilized to calculate the expected reference areas for the 2WL peaks.

This hydration ratio thus represents the *normalized (001) Bragg peak intensities*.

Unfortunately the initial reference scans recorded *prior* to the experiment were not performed under the same humidity and temperature conditions as those prevailing during the experiment.<sup>15</sup> This mistake may account for at least some of the deviation in the peak factor from unity; comparing the fully developed pure peak area of the reference scans with scans at corresponding sample positions taken *during* the experiment and besides assumed to be purely monohydrated, the comparison reveals that the monohydrated peak area at experimental conditions was on average 0.87 that of the corresponding area at pre-experimental conditions.

#### TIME AND SPATIAL EVOLUTION OF HYDRATION STATES

Now that the intensities are normalized a proper comparison of the spatial and time evolution of the hydration states is possible.

<sup>15</sup>The initial reference scans were recorded under room temperature and ambient air humidity.

**Time evolution of the normalized (001) Bragg peak intensities** For each position, the time evolution of the hydration states, represented by the normalized peak areas, were plotted. Figure 3.14 shows this evolution in time for an arbitrary chosen sample position. The large error bars for low normalized intensities are due to relatively large uncertainty in the fits of *small* hydration peaks. As the peaks grow, the fits become more accurate thereby decreasing the error bars.

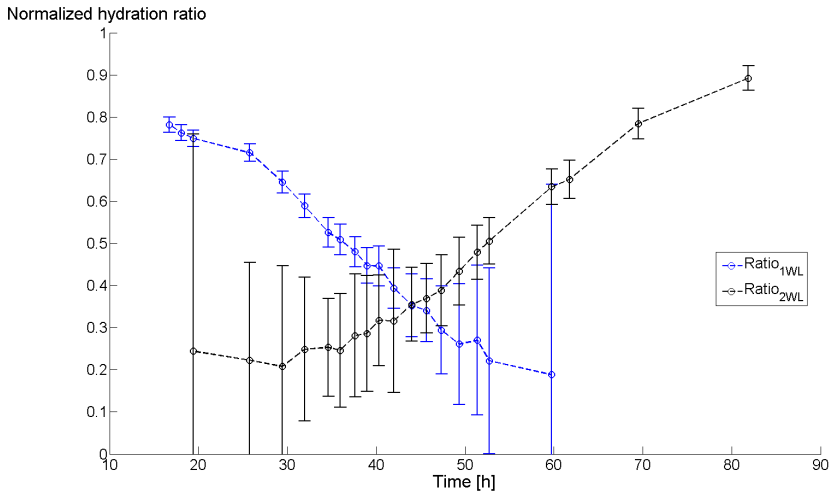


Figure 3.14: Time evolution of the *normalized* (001) Bragg peak intensities for fixed position coordinate  $x = 7.1\text{mm}$ .

The intersection of the two hydration curves was estimated at a hydration ratio of  $\sim (0.35 \pm 0.05)$ , which means that about 35% of the crystallites are monohydrated, 35% bi-hydrated and the remaining 30% disordered/mixed at the intersection.

**Spatial evolution of the normalized (001) Bragg peak intensities** We are also able to plot normalized hydration intensities for a 'fixed' time (Figure 3.15). In this way we may determine additional intersection points of the two hydration curves.

**3D representation of the normalized hydration states** A script was made in order to give a 3D representation of the dynamics of the normalized states. This can be very useful in observing the relation between the spatial and time coordinate.

The data points were represented as a 3D matrix with the time coordinate, spatial coordinate and normalized intensity as the three matrix parameters (corresponding to the Cartesian coordinates ( $x,y,z$ )). As only one intensity measurement can be obtained for each time coordinate, the vacances in the matrix (that is for the all the remainders of the spatial coordinates) had to be interpolated. This was done linearly by the time weighed average of the two closest scans of identical spatial coordinate.

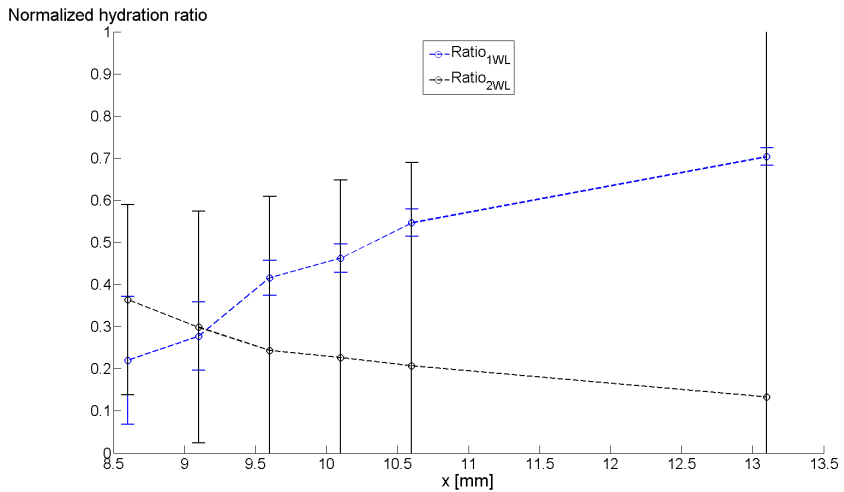


Figure 3.15: Spatial evolution of the *normalized* (001) Bragg peak intensities for 'fixed' time coordinate  $t = (348.5 \pm 1.0)h$ .

The results are plotted in Figure 3.16a and Figure 3.16b for the mono- and bihydrated cases respectively. Figure 3.14 and Figure 3.15 may then be viewed as vertical planar intersections of the 3D model.

**Analysis** From Figure 3.14, Figure 3.15 and Figures 3.16a and 3.16b the intercalation process is observed to be fast (large gradient of the curvatures) for small ingress parameters  $x$ . However, for increasing ingress parameters the absolute value of the curvature gradient decreases rapidly and seemingly approaches zero asymptotically, indicating the slowing down of the intercalation front speed to zero.

However, the dynamics of this gradient with spatial and time coordinate only roughly indicates the behaviour of the intercalation front. A more precise definition needs to be established.

#### INTERCALATION FRONT

A natural choice for defining the *center* of the intercalation front is the intersection of the hydration curves, which implies that the proportion of crystallites is equally large for the two pure hydration states. On page 73 this is experimentally found to be  $(0.35 \pm 0.05)$  for our data plots, which indicates a relatively stable criteria.

The dynamics of the intercalation front (e.g.: center) can thus be readily determined from the several intersections of time- and spatial evolution plots of normalized Bragg intensities. In Figure 3.17 these intercalation front time and spatial coordinates have been plotted with their two-dimensional errorbars (although they are vanishingly small for the blue data set). The blue data points are determined by varying the time coordinate and maintaining the spatial

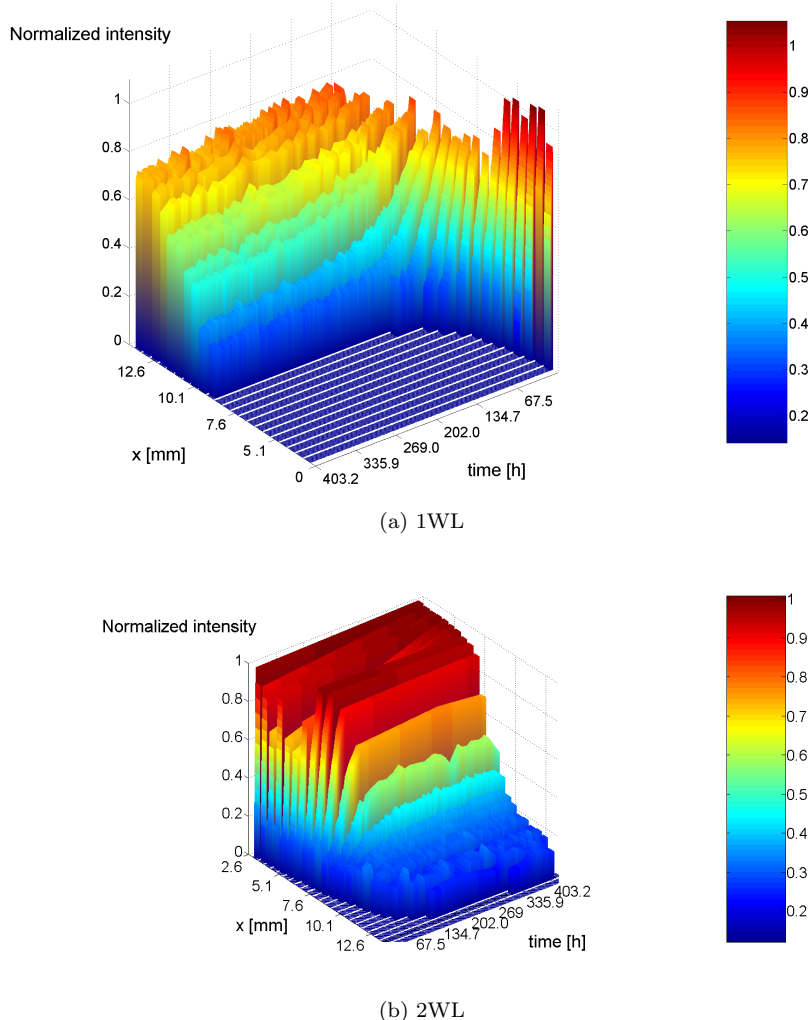


Figure 3.16: 3D representation of the normalized hydration dynamics. Observe how the absolute value of the gradient of the curvatures of fixed positions decreases with increasing ingress parameter  $x$ .

coordinate fixed, whereas the pink data points are conversely determined varying the spatial coordinate and holding the time coordinate significantly 'fixed'. The two data sets almost perfectly collapse.

**Function fit** Several functions were attempted for functional fitting; simple exponential ( $x = x_0 \left(1 - e^{-\frac{t}{\tau}}\right)$ ; two degrees of freedom), stretched exponential ( $x = x_0 \left(1 - e^{-\left(\frac{t}{\tau}\right)^\beta}\right)$ ; three degrees of freedom), multi-termed simple exponential ( $x = x_0 \left(e^{-\frac{t}{\tau_1}} - e^{-\frac{t}{\tau_2}}\right)$ ; three degrees of freedom) and a power-law

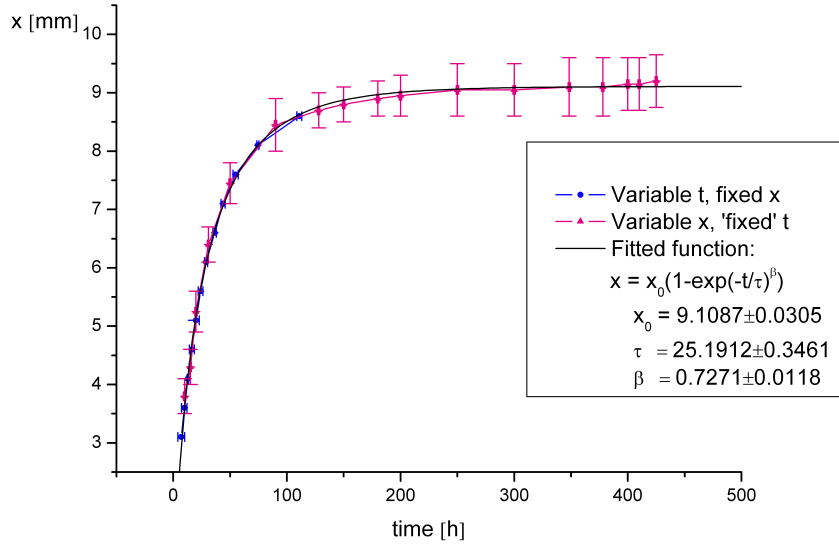


Figure 3.17: Function fit of the intercalation front. The intersection points of the hydration curves result in two data series corresponding to holding one of the time or spatial variables fixed while varying the other (blue and pink data points). We define the collapse of these points to reflect the dynamics of the spatial evolution of the intercalation front. A stretched exponential yielded an almost perfect fit (black line) of the data points.

$$(x = x_0 \left(1 - \left(\frac{t}{\tau}\right)^\beta\right); \text{three degrees of freedom}).^{16}$$

The stretched exponential yielded the best fit by far

$$x = x_0 \left(1 - e^{-\left(\frac{t}{\tau}\right)^\beta}\right) \quad (3.3)$$

with fitted parameters  $x_0 = (9.1087 \pm 0.0305) \text{ mm}$ ,  $\tau = (25.1912 \pm 0.3461) \text{ s}^{-1}$  and  $\beta = (0.7271 \pm 0.0118)$ . The function is plotted in Figure 3.17 and is seen to be an excellent fit to the data points.

**Speed and width of the intercalation front** Defining the intercalation *head* as the boundary of where there is a noticeable change in the hydration state of the 2WL hydration state, and correspondingly defining the intercalation *tail* to be where there is a formidable extinction of the 1WL hydration state, the *time* evolution of the normalized hydration states provides some information on the speed at which the intercalation front advances through the sample. For the position  $x = 7.1 \text{ mm}$  in Figure 3.14 this can be roughly estimated to be (at least)  $\sim 40 \text{ h}$ , but we are clearly suffering under the lack of data scans and successful fits for small peaks sufficiently far from the center of the front. Similar estimates at

<sup>16</sup>The theorists allegedly 'prefer' a combination of a stretched exponential with a power law. However, the large degree of freedom thus implied would almost certainly result in a successful fit. Meanwhile one here wishes to restrict the degree of freedom to a minimum.

other positions are possible, but the great inaccuracies in these crude estimates are so large that further investigation is meaningless. Nevertheless, the head as well as the tail are also expected to behave as stretched exponentials with the same  $\tau$  and  $\beta$  parameters, but with respectively higher and lower asymptotic constants  $x_0^{\text{head}}$  and  $x_0^{\text{tail}}$  compared to the fitted center value  $x_0^{\text{center}}$ .

On the other hand the *spatial* data present a similar representation (see for instance Figure 3.14), but the width of the plot is instead related to the width of the front. In this experiment the recorded data frames were taken at positions mainly *in the neighbourhood* of the intercalation front. Positions sufficiently far from this 'action pot' were not scanned. Thus we were once again not able to monitor the dynamics sufficiently far from the intercalation front. However, at the end of the experiment a reference end scan was recorded (see 2.2.4) that included *all* sample positions. As the intercalation front was nearly halted at this point, at least significantly slow compared to the duration of the scans, we were able to consider this scan series to be a reflection of the *simultaneous* picture of the entire sample.

Figure 3.18 shows the normalized intensities for this ending reference scan. This is the best spatial plot there is in this experiment where the scanned

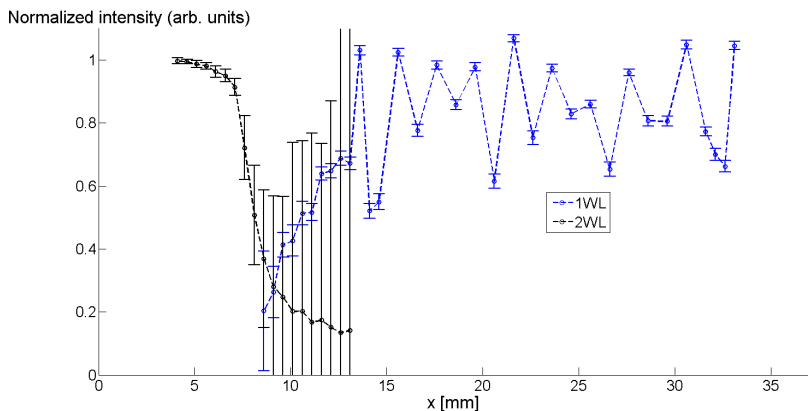


Figure 3.18: Normalized intensities at the end of the experiment.

positions stretch far beyond the 'action pot' of the vicinity of the intercalation front. However, here we encounter another problem in obtaining a good fit for small peaks and the great errorbars they inflict. Thus only a crude estimate of the front width may be deducted; from Figure 3.18 the transition from the monohydrated to the bi-hydrated state is observed to occur within  $\sim (6.5 \pm 2.0)\text{mm}$ . Taking the width of the beam ( $\sim 0.4\text{mm}$  for the core beam) into account and assuming that the apparent width of the intercalation front results from the convolution of the beam width the front profile, we estimate the width of the intercalation front to be  $\sim 6\text{mm}$  at  $x \sim 9.1\text{mm}$  into the sample. This is a far greater value than obtained in [15] not taking into consideration the significant inaccuracy. However this clearly suggests a very wide front compared to the ingress (approximately 2 : 3 ratio).

It would be worth trying to plot the evolution in time and space of the hydration states as a function of the measured normalized amplitude of the peaks. This would result in values for every scan, also the scans with small peaks not passing the pseudo-Vogitian fit procedure. Conversely the amplitude does not necessarily relate to the area and the proportion of the scattering elements in the correct manner. But an estimate on both the width and speed of the intercalation front should be easily obtained.

#### TIME-FRACTIONAL VARIABLE

In the discussion of diffusion, normal and anomalous, in 1.3 a method of introducing a fractional scaling parameter was proposed as a mean to check for anomality in the transport process. This could be done assuming some limiting conditions on the system setup.

In our case these conditions were met,<sup>17</sup> and consequently an attempt was made on plotting the hydration states as a function of a spatio-temporal scaling variable  $\eta = \frac{x}{t^{\gamma/2}}$  where  $\gamma$  is the time-fractional parameter. According to 1.3 one should then obtain a universal curve signifying a data collapse. For normal diffusion  $\gamma = 1$  is to be expected, whereas  $0 < \gamma < 1$  signifies a case of subdiffusive behaviour.

It proved difficult to obtain a data collapse for the full time and/or spatial data range here presented. As mentioned earlier the focus during the experiment had all been on the 'activity pot' of the intercalation front thereby 'neglecting' the far environment of this front not knowing the implication of this for the later analysis. As the dynamics of the intercalation front after a short while was relatively slow compared to the rate of scanned frames, we obtained several recorded frames for only a limited range of positions for a given time interval. In short this measuring method implied that there was only a small considerable overlap of the different data sets of various non-neighbouring positions. This complicated a comparison of data collapses of different  $\gamma$ -values because the series representing time evolution of each position was seemingly aligned after one another rather than on top of each other when varying the time-fractional.

However, a crude estimate was nevertheless possible from Figures 3.19a, 3.19b and 3.19c. These seemed to indicate that  $\gamma$  varies with time and/or position (these are, as argued for above, very much related and almost inseparable in this context) from initially close to that of normal diffusion and approaching very low values for the final scans and/or positions.

It is also important to reflect on what is the underlying *diffusing media* related to the estimation of  $\gamma$  from the hydration states: The hydration states reflect the amount of a sample volume that is in a *pure* hydrated state. This is again likely to reflect some degree of relative humidity in the surrounding porous environments. However, it is this threshold limit that initiates the fast intercalation process ('fast' is used here as opposed to the 'slow' intercalation process

---

<sup>17</sup>These conditions are reflected in the assumption of a semi-infinite media and may be explicitly expressed in the boundary conditions of the given case (see for example Equation (1.44) in 1.3.1).

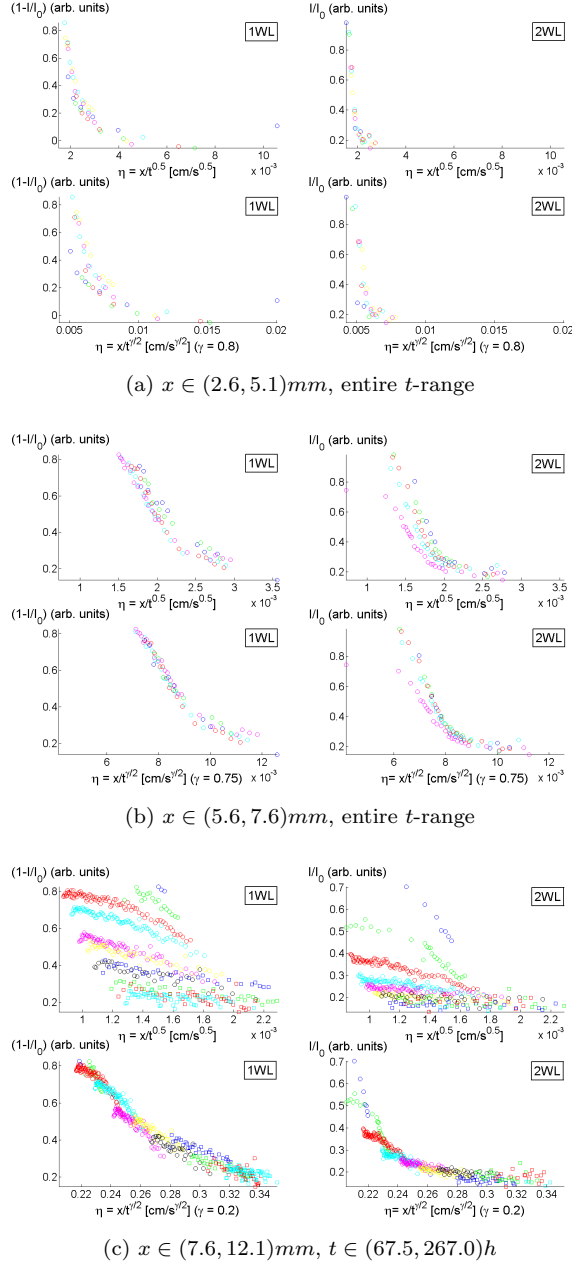


Figure 3.19: Data collapse with a spatio-temporal scaling variable. (a) For the first data set, representing the first sample positions,  $\gamma = 1$  yields the best fit implying normal diffusion behaviour.  $\gamma = 0.8$  is also plotted for reference. (b) For the second data set, representing positions further into the sample,  $\gamma \sim 0.75$  gives the best data collapse implying anomalous behaviour. (c) Finally for the last positions far into the sample  $\gamma \sim 0.2$  implies a strong anomalous behaviour. Notice the limitation in the time range for this last series.

possibly described by the previously discussed detection of peak displacement). Whether or not this 'threshold transport', represented by the center of the intercalation front, through the sample can be described as diffusive remains to be said. Provided that this is true, the results thus seem to imply a decreasing  $\gamma$ -parameter with time/spatial ingress.

### 3.2.3 Hydrophilic character of glass capillaries

The glass capillary is known to be quite *hydrophilic* and therefore attracts water. Hydrophilic refers to the physical property of a molecule that can bond with water ( $H_2O$ ) through a hydrogen bonding. According to thermodynamics all matter seek to be in a low-energy state, and hydrogen bonding of a polar molecule to water thus lowers the energy state [43].

Silica surfaces are known to exhibit up to about  $8\mu mol/m^2$  of hydroxyl groups, which corresponds to about 4.6 free hydroxyl groups per  $10nm^2$  of glass [48]. This high density causes a strong attraction of water.

In order to avoid disturbance due to this phenomenon, a *silanization* process was carried out. Here the free hydroxyl groups are made to react with silicon compounds to yield a *hydrophobe* glass surface. Hydrophobes, also called lipophobes, are not electrically polarized, and because they do not form hydrogen bonds, water is repelled in favor of bonding internally [43]. The hydrophobes instead prefer other neutral and nonpolar solvents or molecular environments.

**Method** There was no known procedure to be found in literature describing the silanization of glass capillaries, hence the entire process had to be done by trial and error. However, other literature (for example [48]) describing other silanization procedures suggested silanization by vapor treatment as the best method. The applied method in this context was adapted as best possible.

A small amount of silanization reagent<sup>18</sup> was injected at the open ends of the glass capillaries, which were next turned up-side down and put in a beaker. A glass lid was used to create a sealed off environment. The beaker with the samples was heated at  $200^\circ C$  for about one hour. During this time, the silicon compound evaporates and is expected to bind covalently to the free hydroxyl groups of glass (Figure 3.20).

**Check** A check on the result was done by examining the contact angle in a silanized capillary and compare this to that of a non-treated capillary. The result can clearly be seen in Figure 3.21, confirming a successful silanization treatment.

**Analysis** Eight samples of Na-fluorohectorite was prepared in similar glass capillaries, four being treated with silanization solution and the other four remaining non-treated. The temperature was lowered and an equal humidity gradient was imposed on all the samples.

The idea is to investigate whether or not the hydrophilic properties of the capillaries affect the speed of the water transport in any significant manner.

<sup>18</sup> Silanization solution 1 from Sigma-Aldrich. Chemical facts: ~ 5% dimethyldichlorosilane ( $C_2H_6Cl_2Si$ ) in heptane.

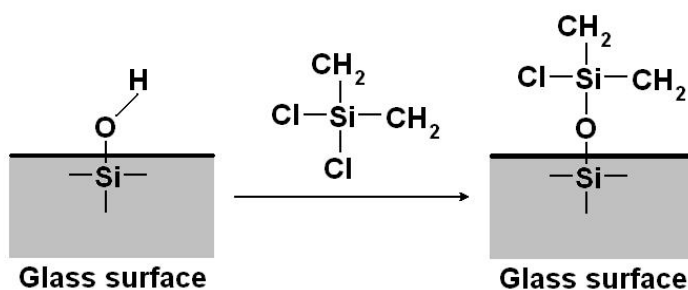


Figure 3.20: Silanization of hydrophilic glass surface with reactive chlorosilane.

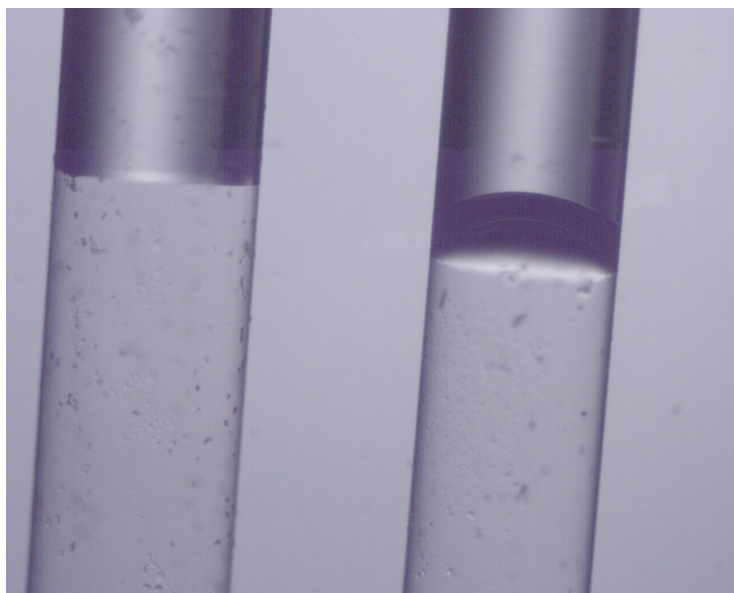


Figure 3.21: Microscope photograph of a silanized and a non-treated glass capillary. The capillary to the left was treated with a silanization solution, whereas that to the right was non-treated. Note the difference in contact angle; the water is clearly attracted along the glass walls of the non-treated capillary. Conversely, the water surface in the treated capillary is almost 'flat' and sharp.

Unfortunately it is still too early for any results of this presently ongoing experiment to be presented in this report.

### 3.2.4 Disordered/mixed intercalation

Referring to Figure 3.11a states of mixed intercalation is clearly visible between the Bragg peaks. A representative transition via mixed states is plotted in Figures 3.22a to 3.22f. The fitted data for the pure peaks have been subtracted from the recorded data, thus revealing the recordings intermediate of the Bragg peaks believed to be the signature of mixed/disordered intercalation. For these intermediate points, very broad line shapes are observed including two or more

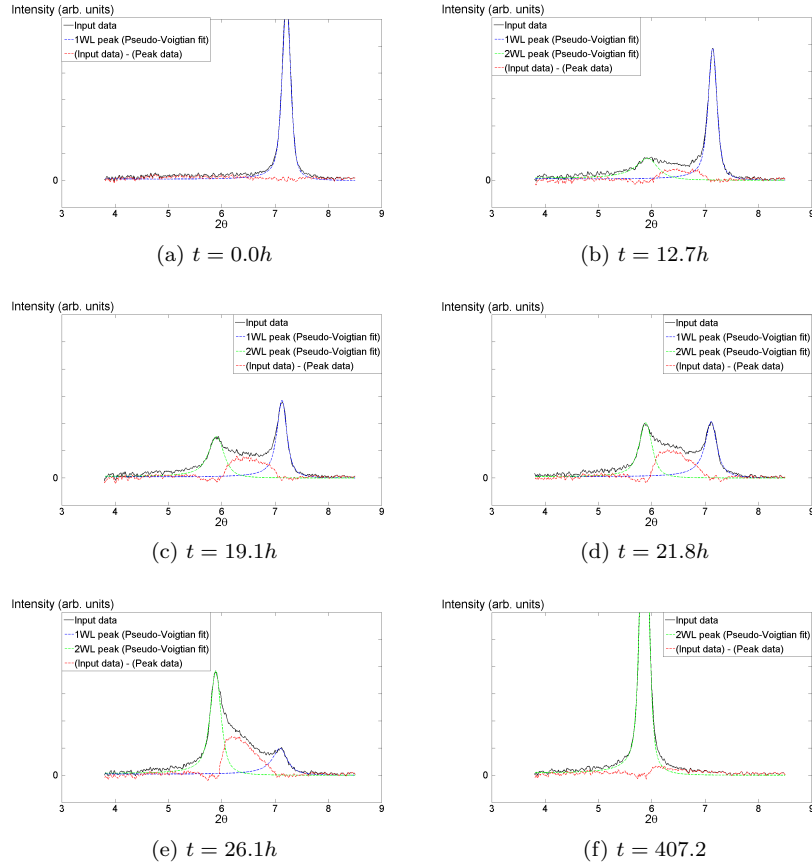


Figure 3.22: Disordered intercalation. The figure series shows the evolution of the disordered intercalation at a fixed position  $x = 5.6\text{mm}$ . The black curve is the recorded data, while the blue and green curves represent the pseudo-Voigtian fits of the mono- and bi-hydrated cases respectively. The red curve is the peak fits subtracted from the recorded data thus yielding the contribution of mixed states.

peaks. This series, naturally being a very crude estimate, is pretty much consistent with the transient Hendricks-Teller mixed-intercalation formalism (described in 1.2.12) and thus clearly illustrates the considerable contribution from this two-state coexistence.

This transition region of Hendricks-Teller state is what complicates peak fitting procedures during hydration dynamics. The peak width and height of the Hendricks-Teller state, originating in the combination of different states of different possibilities, is determined by the closeness of the respective interference maxima of the two conditions, but as the series clearly reveals the tails of the Hendricks-Teller state and the pure Bragg peaks overlap considerably. Thereby the shoulder often seen appearing on the left side of the monohydrated peaks and on the right side of the bi-hydrated peaks is the sign of Hendricks-Teller mixed intercalation indicating a small proportion of respectively two and one water-layer-spacings existing in the scattering volume.

We leave the discussion at this point. The purpose was only to illustrate the observable interpeak signals and relate them to the Hendricks-Teller formalism as well as throw light on the asymmetrical effects this cause on the peak shape, thus complicating the peak fitting procedures.

### 3.3 Discussion

In this experiment some aspects regarding the underlying physics of water transport were considered. First a slight displacement of the Bragg peaks was observed for positions far from the intercalation front. This point will be discussed in 3.3.1. Then the intercalation front was defined, plotted and function fitted to a stretched exponential. The relation between this stretched exponential and the time-fractional parameter is discussed in 3.3.2.

#### 3.3.1 Peak displacement

In subsection 3.2.2, examining the terminating reference scan, the Bragg peak of pure monohydrated states was observed to be slightly displaced towards lower angles, almost linearly, for positions close to the end of the sample and thus far from the intercalation front.<sup>19</sup> Especially interesting was the seemingly linear approach and subsequent collapse of the two curves respectively describing the initial reference peak values and the terminating reference peak values (Figures 3.7a and 3.7b).

The displacement can not be due to thermal expansion; for that the order is too large, and such a contribution would *decrease* the  $d$ -spacing, not *increase* as observed, due to the lowering of temperature from the initial reference scan series to the terminating reference series. The order of the displacement was found to be about  $0.0043\text{\AA}$  per centimeter of ingress in the apparent *linear* region of the displacement (the light blue plots of the monohydrated cases in Figures 3.7a and 3.7b).

**Underlying causes** Such a displacement would imply, given that there are no instrumentally or experimentally inflicted causes, a change in the physical property of the  $d$ -interlayer spacing. There may be two reasons or a combination of the two; first the displacement is a signal of water intercalation into the interlayer spacing thus slightly increasing the basal distance  $d$ . As proposed in subsection 3.2.1 one can imagine this process of water diffusing into the interlayer spacing where all the favourable positions are occupied in an attempt to minimize the system energy. Thus the intercalating water molecules are positioned in more unfavourable positions leading to a small expansion of the interlayer spacing. The driving force of the water vapor diffusion into the interlayer spacing (thus equalizing the chemical potential caused by unevenly balanced particle concentrations) is possible balanced by the energy needed to expand the layer distance. Hence the rate of this expansion would be proportional to the dynamics of the relative humidity in the mesopores, thus directly

<sup>19</sup>The bi-hydrated peaks also displayed an equal and opposite displacement, however the data for the monohydrated case were better suited for a closer investigation.

relating the displacement to water vapor porous diffusion.<sup>20</sup>

Secondly a peak displacement may origin in the curve fitting procedure. A peak shoulder will appear to the left due to water intercalation, and this shoulder could bias the peak fitting. In any case, whether the first or the second or possibly both factors contribute, the physical interpretation origins in intercalation of water. Thus such a peak displacement is anyhow directly related to the presence of water in the sample volume and can thus be utilized for tracing the water vapor front directly once the displacement is known as a function of the relative humidity.

Let us go back to the first argument. One can imagine this process to continue until a limiting threshold value of the relative humidity is reached. At this point the 'slow' displacement inhibited up till now is overshadowed by a much faster and larger contribution. After the domain of this 'fast' intercalation a 'slow' intercalation domain is once again reached thus slightly displacing the bi-hydrated peaks in a similar manner depending on the relative humidity.

Assuming the relative distributions of these 'fast' and 'slow' humidity domains to be temperature sensitive, an explanation is given for why different humidities impose different speeds of the intercalation front. For instance for the second scan series (2.2.5) the intercalation speed was found to be much faster than compared to the third series, which has been the main focus of this report. For the second series the temperature was significantly lower,  $T_2 \sim 10^\circ C$ , than that of the third series,  $T_3 \sim 15^\circ C$  (see subsection 2.2.4). However, the relative humidity was also lower (constantly decreasing from about  $RH \sim 85\%$  to  $RH \sim 65\%$  before terminating the series) than that of the third series ( $RH_{humid} \sim 99.9\%$ ). Then assuming that the threshold value for the second series with lower temperature is much lower than in the case of the third series. Thus the lower relative humidity of the imposed humidity 'reservoir' is compensated for by a lower temperature-dependant threshold value.

**Humidity gradient** The humidity gradient is assumed to be linear at infinite time. At one sample end we have an 'infinite' humidity reservoir, while at the opposite end the air is non-humid. By equilibrium conditions a linear gradient is a plausible assumption. At  $t = 0$  the humidity gradient is a delta function. With time it evolves and approaches the equilibrium (linear) gradient. The closer the real gradient is to the equilibrium gradient, the slower is the dynamics of the water vapor front. Assuming that the initiation of the ('fast') water intercalation process from a mono- to a bi-hydrated state relies on a limiting relative humidity threshold, this explains the corresponding decrease in the speed of the intercalation front and subsequent complete halt. This development is outlined in Figure 3.23. The coloured lines indicate different time plots of the suggested water vapor gradient through the system. The intersection of the threshold value with the humidity profile defines the intercalation front. These intersection points are checked on the abscisse at  $x = 0, x', x'', x''', x_{INF}$ . The endpoint of our experiment corresponds to the pink line where the water front has almost

---

<sup>20</sup>If so it is the slow dynamics of the water vapor front which enables the detection of this systematical displacement with spatial position. In the case of faster dynamics these small shifts would probably not appear as related because the dynamics of the water transport is comparable in size to the scan rate. For slow dynamics, as in our reference end scans, the picture on the other hand appear as close to static and therefore enables this detection.

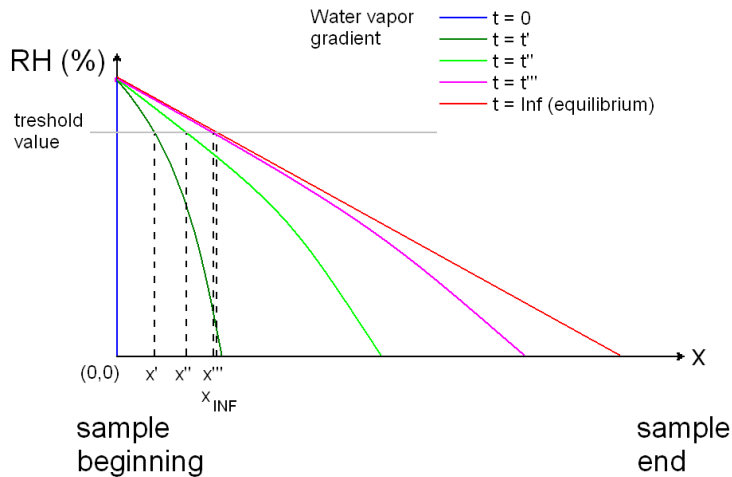


Figure 3.23: Suggested relation between the humidity gradient and intercalation front.

reached the end of the sample. From the plot of peak displacements (Figure 3.7a and 3.7b) the collapse of data line was at about  $x \sim 35\text{mm}$  (the length of the sample capillary is about  $\sim 42\text{mm}$ ). Thus the water front is expected to move slowly towards equilibrium as the gradients of the two states are already very close. From the intersects of the threshold defining line in the figure and the humidity gradient we observe that at this state an advance in the humidity front results in a significantly smaller advance in the lagging intercalation front.

**Finalizing comment** The ideas presented in this subsection are just exactly ideas and must not be interpreted otherwise. However they give rise to aspects worth investigating closer in future experiments. In order to examine the effect of the fitting procedure on seemingly pure peaks and whether or not the fitting itself could inflict this regular peak displacement, various fittings were performed for representative peaks. Although the uncertainty imposed by different fitting criterias were not found to be of the same order as the displacement, experimental errors as a cause to the systematical displacement can still not be completely excluded and needs closer investigation.

### 3.3.2 Anomalous transport

The data collapse obtained by introducing a spatio-temporal scaling variable suggests a  $\gamma$ -value varying with time and/or positions. This preliminary indicates a varying anomalous behaviour of the water intercalation front. Not being able to scale the time dependency of the hydration states at different positions is normally an indication of different underlying physics.

A semi-log plot of the hydration states (Figure 3.24) seem to separate the spatial region into two realms; one for  $x < 8.1\text{mm}$  (the steep plots) and the other for  $x > 9.1\text{mm}$  (the almost horizontal series). Notice how this corresponds to the seemingly final ingress of the water intercalation front. Also with time there seems to be a sharp distinction around  $t \sim 100h$ . From Figure 3.17 this

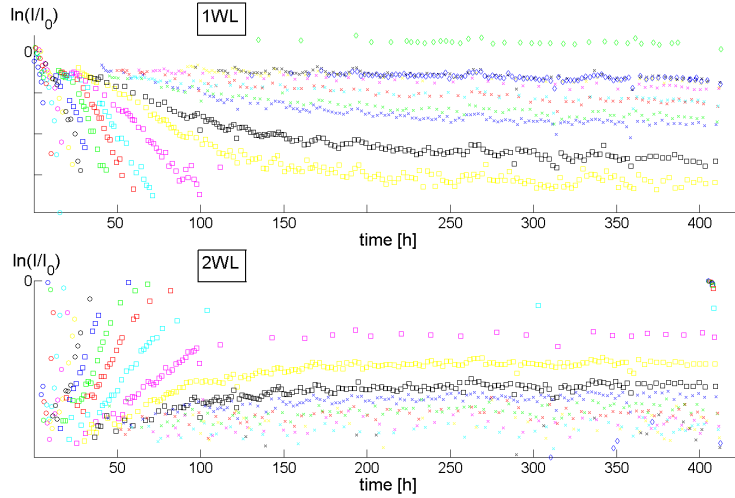


Figure 3.24: Semi-log plot of the evolution of normalized hydration states.

corresponds to the time at where the intercalation front practically comes to a halt ( $100h$  is approximately four times the characteristic time constant of the fitted stretched exponential in Figure 3.17).

From the analysis of the spatio-temporal scaling variable and especially the crudely estimated results connected to the Figures 3.19a, 3.19b and 3.19c, it is tempting to view these results in connection with the information drawn out of the semi-log plot of Figure 3.24. Doing so the diffusion of the intercalation front seem to be anomalous with  $\gamma \sim (0.75 - 1)$  before it practically halts at  $x \sim 9mm$ .

The *stretched exponential* of the fitted intercalation front function given by Equation (3.3) returned a characteristic time parameter of  $\beta \sim 0.7271$ . This value is supposedly related to the time-fractional parameter  $\gamma$  under some conditions allowing related integrals to be solved. However, the proper relation has not yet been found in any literature.

Once again I would like to underline the fact that at this point the ideas are pure speculations. Further investigation needs to be performed in order to establish anything on this matter. Also notice that we are now treating the diffusion character of the *intercalation front*. However, its relation to the *water vapor front* is not yet fully known beyond plausible assumptions of a threshold value.

**Comment** Imagine hydrophilic walls in a porous media. In the pore structure there will exist a front intersecting the dry and humid regions. How this water behaves in the pores, as vapor or condensated as small droplets, is not yet known. Anyhow the water will be attracted along the pores with a constant force due to the hydrophilic characteristics. But the same characteristics also induce friction proportional to the area of the humid walls. As the 'pulling

force' is constant and the friction force increases, a logical assumption would be to expect that the diffusion will not behave linearly.

Note that this mind play only is based on the fact of diffusion in a porous material of hydrophilic character.

A similar experiment has been performed on a sample of zeolite [40], which was determined experimentally to be anomalous with a time-fractional parameter of  $\gamma \sim 0.36$ . However, there are some major differences in these two experiments; zeolite does not swell, and the nanopores are of another character. Furthermore the experiment on zeolite was performed with saturated water and not vapor as in our case. Nevertheless, the experiment disclosed anormalous diffusion in a nanoporous media.

#### ERRORS AND IMPROVEMENTS

As always corrections can and should be done in order to improve the validity of the results. Here only the most important considerations will be discussed.

Several subjects in this experiment focused on the normalized hydration states. These were, for the monohydrated case, referenced to the intital reference scan. However, these were recorded under different temperatures and humidities than those prevailing during the experiment. The error thereby imposed is unknown.

Another obvious error source is the fitting procedure. This is a very critical element. Not only does the script need to be correct, but the inputs must also be optimized. Despite the huge effort put into minimizing and localizing parametric error sources, the automation of the fitting procedure may have given rise to some errors not known.

Some consecutive scans of the identical position clearly deviated in intensity, but not in shape, in such a way that the only possible explanations are either sudden fluctuations in the beam, which is not very likely, or that the goniometer is not returning the sample to the exact same location as in the previous scan. These intensity fluctuations are manifested as small 'jumps' in several of the plots.

Also the existence of a pressure gradient would influence the diffusion rate in an unwanted manner.

Last, but not least, the hydrophilic property of the glass capillary *may* introduce some effects on the speed of the observable water transport. This matter will however likely be solved and presented in some future works.

Finally the biggest improvement given the same facilities would be to extend the spatial scan interval and not only focus on the 'activity pot' around the intercalation front. Through this invaluable information can be gained making feasible a more detailed estimate of certain physical parameters, especially the width of the front and the speed at which it advances through a fixed sample position.

# Chapter 4

## Conclusion

The Wide Angle X-ray Scattering (WAXS) measurements of water vapor transport in general and the water intercalation front in particular were performed on a powder sample of the synthetic clay mineral Na-fluorohectorite known to be purely monohydrated at the initiation of the experiment. The (001) Bragg peak gives an indication of the interlayer stacking distance of the fundamental layered silica lamellae through the application of the scattering angle and Bragg's law. Lowering the temperature and imposing a humidity gradient the dynamics of the interlayer spacing was monitored in the dynamics of the scattering signature as water intercalated through the sample. Through analyzing these data different aspects of the water transport were enlightened and examined.

The intercalation process was known to be temperature and humidity dependent. At the prevailing conditions,  $T \sim 15^\circ C$  and  $RH_{\text{humid}} \sim 99.9\%$  and  $RH_{\text{dry}} \sim 0.03\%$ , the intercalation front was shown to yield a good fit with a stretched exponential

$$x = x_0 \left(1 - e^{-\left(\frac{t}{\tau}\right)^\beta}\right)$$

with fitted parameters  $x_0 = (9.1087 \pm 0.0305) \text{ mm}$ ,  $\tau = (25.1912 \pm 0.3461) \text{ s}^{-1}$  and  $\beta = (0.7271 \pm 0.0118)$ . The asymptotic parameter  $x_0$  indicates the penetration depth of the intercalation front, whereas the characteristic time constant  $\tau$  says something about the rate at which the intercalation front advances through the sample. Finally the remaining  $\beta$  parameter is thought to be related to the fractional time parameter  $\gamma$  under certain conditions and thereby says something about the possible anomaly of the diffusive character.

Furthermore the head and tail of the front is likely to follow the same stretched exponential, but with respectively higher and lower asymptotic parameters  $x_0$ , counting for the observed broadening of the front width.

An attempt was done on introducing a spatio-temporal scaling parameter for the normalized hydration states. A universal curve of the entire data span for various  $\gamma$ -parameters was not found, however data collapse was observed to some degree when restricting the data to certain time intervals/positions. These estimated  $\gamma$  values were shown to decrease with time and/or positional ingress. Moreover the apparent inaccuracy did not seem to validate these observations.

Nevertheless, by comparing the behaviour of the intercalation front to the deducted knowledge on penetration depth and characteristic time constant, an anomalous behaviour with  $\gamma \sim [0.75, 1]$  seems to be the best estimate if one should be given.

The intercalation front was also shown to have a considerable width; almost displaying a 2:3 ratio with the penetration depth as the asymptotic value  $x_0$  was approached. This is in contrast with the narrow widths previously reported for similar experiments. Furthermore at  $x = 7.1$  into the sample the intercalation front was estimated to use at least 40h on advancing through the sample position head and tail.

Despite the lack of good estimates on the width of the front, both head and tail are nevertheless expected to display the same stretched exponential form; probably with the same time constant  $\tau$  and fractional time parameter  $\gamma$ , but with a respectively higher and lower valued asymptotic parameters  $x_0^{\text{head}}$  and  $x_0^{\text{tail}}$ .

A small but seemingly ordered displacement of the monohydrous as well as the bi-hydrated peak center values was observed at the end of the experiment. For peaks being visually symmetrical, also in a semi-log plot, this displacement appeared to be linear with a gradient of roughly  $\sim 0.04\text{\AA}$  per centimeter of ingress for the monohydrous case. '

The displacement is suggested to be due to the presence of water vapor in the surrounding mesoporous space leading too subtle intercalation of water into the interlayer spacing, but not inflicting a transition of water layer state. The initiation of such a process is believed to be due to a threshold limit in the relative humidity.

An estimate was given for the particle size utilizing the Scherrer equation with the deducted Lorentzian peak widths from the peaks fitted by a pseudo-Voigtian function. This mean thickness of the crystallites was found to be a bit lower than expected, but none-size contributions to the Lorentzian peak width, for instance strain, is assumed to compensate for this discrepancy. Finally a signature of random or mixed intercalation states attributable to the Hendricks-Teller formalism was detectable at all sample positions.

## Suggestions for future experiments

A study of the peak displacements as a function of relative humidity under fixed temperature conditions would be very interesting. Furthermore a similar setup like in this experiment, but rather scanning the sample back and forth instead of focusing on the 'action pot' of the intercalation front, would probably also give a useful insight into the physics behind these effects if any at all.

Anyhow a study should be performed of the onset of the 'fast' intercalation process as a function of relative humidity and with fixed temperature; in other words examine the existence of a threshold value and determine the numerical values if such do exist.

# Bibliography

- [1] J.O. Fossum. Complex physical phenomena in clays. Presented at: Nato Advanced Study Institute: 'Soft Condensed Matter: Configurations, Dynamics and Functionality', 1999.
- [2] D.L. Rowell. *Soil Science - Methods & Applications*. Longman Scientific & Technical, 1994.
- [3] <http://www.materialkemi.lth.se>.
- [4] <http://www.gly.uga.edu/schroeder>.
- [5] Duane M. Moore and Robert C. Reynolds Jr. *X-ray Diffraction and the Identification and Analysis of Clay Minerals*. Oxford University Press, second edition, 1997.
- [6] E. DiMasi, J.O. Fossum, T. Gog, and C. Venkataraman. Orientational order in gravity dispersed clay colloids: A synchrotron x-ray scattering study of na-fluorohectorite suspensions. *Physical Review E*, 64, 2001.
- [7] G. da Silva, J.O. Fossum, E. DiMasi, K.J. Måløy, and S.B. Lutnæs. Synchrotron x-ray scattering studies of water intercalation in a layered synthetic silicate. *Physical Review E*, 66, 2002.
- [8] S.A. Solin. Clays and clay intercalation compounds: Properties and physical phenomena. *Annu. Rev. Mater. Sci.*, 1997.
- [9] B. Velde. *Introduction to Clay Minerals*. Chapman & Hall, 1992.
- [10] K.D. Knudsen, J.O. Fossum, G. Helgesen, and M.W. Haakestad. Small-angle neutron scattering from a nanolayered synthetic silicate. *Physica B*, 352, 2004.
- [11] P.D. Kaviratna, Thomas J. Pinnavaia, and P.A. Schröder. Dielectric properties of smectite clays. *J. Phys. Chem. Solids*, 57(12), 1996.
- [12] Patrick Bernier, John E. Fisher, Siegmar Roth, and Stuart A. Solin, editors. *Chemical Physics of Intercalation II*, volume 305 of *NATO Advanced Science Institute Series. Series B, Physics*. Plenum, 1993.
- [13] [http://www.soils.wisc.edu/virtual\\_museum/soil\\_smectite](http://www.soils.wisc.edu/virtual_museum/soil_smectite).
- [14] J.O. Fossum, Y. Méheust, K.P.S. Parmar, K.D. Knudsen, K.J. Måløy, and D.M. Fonseca. Intercalation-enhanced electric polarization and chain formation of nano-layered particles. *Europhysics Letters*, 74(3), 2006.

- [15] G. Løvoll, B. Sandnes, Y. Méheust, K.J. Måløy, J.O. Fossum, G.J. da Silva, M.S.P. Mundim, R. Droppa Jr., and D.M. Fonseca. Dynamics of water intercalation fronts in a nano-layered synthetic silicate: A synchrotron x-ray scattering study. *Physica B*, 370, 2005.
- [16] Roland Pusch and Raymond N. Yong. *Microstructure of Smectite Clays and Engineering Performance*. Taylor & Francis, 2006.
- [17] <http://www7430.nrlssc.navy.mil/facilities/emf/nanocomp.htm>.
- [18] <http://www.phys.ntnu.no/complex/>.
- [19] <http://www.webmineral.com/data/hectorite.shtml>.
- [20] David A. Laird. Model for crystalline swelling of 2:1 phyllosilicates. *Clays and Clay Minerals*, 44(4), 1996.
- [21] Bruker AXS. *NanoSTAR SAXS System User Manual Vol. 2*, 2004.
- [22] *Basics of X-ray Diffraction*. Scintag Inc., 1999.
- [23] Jens Als-Nielsen and Des McMorrow. *Elements of Modern X-Ray Physics*. Wiley, 2001.
- [24] J. Richard Christman. *Fundamentals of Solid State Physics*. Wiley, 1988.
- [25] Christopher Hammond. *The Basics of Crystallography and Diffraction*, volume 5 of *IUCr Texts on Crystallography*. Oxford University Press, second edition, 2001.
- [26] Harol P. Klug and Leroy E. Alexander. *X-Ray Diffraction Procedures*. Wiley, 1954.
- [27] U. Shmueli. *Reciprocal space*, volume B of *International tables for crystallography*. Kluwer academic publishers, 2001.
- [28] Michael Bass et al. *Fundamentals, techniques & design*, volume 1 of *Handbook of Optics*. McGraw-Hill, Inc., 1995.
- [29] <http://physics.nist.gov/physrefdata/ffast/text/cover.html>.
- [30] G.W.Brindley, G.Brown, et al. *Crystal Structures of Clay Minerals and their X-ray Identification*, volume Monograph No. 5 of *Mineralogical Society*. Oxford University Press, 1984.
- [31] Eric Ferrage et al. New insights on the diffraction of interlayer water in bi-hydrated smectite from x-ray diffraction profile modeling of  $00l$  reflections. *Chem. Mater.*, 17, 2005.
- [32] Prabal Dasgupta. On use of pseudo-voigt profiles in diffraction line broadening analysis. *FIZIKA A (Zagreb)*, 9(2), 2000.
- [33] G. da Silva, J.O. Fossum, E. DiMasi, and K.J Måløy. Hydration transitions in a nanolayered synthetic silicate: A synchrotron x-ray scattering study. *Physical Review B*, 67, 2003.

- [34] Sterling Hendricks and Edward Teller. X-ray interference in partially ordered layer lattices. *Chemical Physics*, 10(3), 1942.
- [35] G. Brown and R. Greene-Kelly. X-ray diffraction by a randomly interstratified clay mineral. *Acta Cryst.*, 7, 1954.
- [36] Yves Méheust. Unpublished.
- [37] <http://chaos.ph.utexas.edu/>.
- [38] United States Environmental Protection Agency. Estimation of infiltration rate in the vadose zone: Compilation of simple mathematical models volume 1, 1998.
- [39] Morten Hjorslev Hansen and Ernst Jan de Place Hansen. Building physics 2002 - 6th nordic symposium: Session 9 - moisture properties - experimental methods, 2002.
- [40] Eduardo N. de Azevedo, Paulo Loureiro de Sousa, Ricardo E. de Souza, M. Engelsberg, Mirla de N. do N. Miranda, and Maria Aparecida Silva. Concentration-dependent diffusivity and anomalous diffusion: A magnetic resonance imaging study of water ingress in porous zeolite. *Phys. Rev. E*, 73, 2006.
- [41] P. Thompson, D.E. Cox, and J.B. Hastings. Rietveld refinement of debye-scherrer synchrotron x-ray data from  $\text{Al}_2\text{O}_3$ . *J. Appl. Cryst.* (1987), 20, 1986.
- [42] Microcal Software, Inc. *User's manual: Origin Peak Fitting Module*, 1997.
- [43] <http://en.wikipedia.org>.
- [44] G.K. Wertheim, M.A. Butler, K.W. West, and D.N.E. Buchanan. Determination of the gaussian and lorentzian content of experimental line shape. *Rev. Sci. Instrum.*, 45(11), 1974.
- [45] T. Ida, M. Ando, and H. Toraya. Extended pseudo-voigt function for approximating the voigt profile. *J. Appl. Cryst.*, 33, 2000.
- [46] Kathleen Lonsdale et al., editors. *Physical and Chemical Values*, volume III of *International tables for x-ray chrystallography*. Kynoch Press, 1968.
- [47] Mike Meier. Measuring crystallite size using x-ray diffraction, the williamson-hall teqnique. 2005.
- [48] Extract recieved from Sigma-Aldrich Norway AS. Construction of liguid membrane microelectrodes.
- [49] C. Hammon. *Introduction to Crystallography*, volume 19 of *Microscopy Handbooks*. Oxford University Press, 1990.
- [50] Kathleen Lonsdale et al., editors. *Mathematical tables*, volume II of *International tables for x-ray chrystallography*. Kynoch Press, 1972.
- [51] J. Richard Christman. *Fundamentals of Solid State Physics*. John Wiley & Sons, first edition, 1988.

- [52] Kenneth D. Knudsen, Jon Otto Fossum, Geir Helgesen, and Vegard Bergaplass. Pore characteristics and water absorption in a synthetic smectite clay. *J.Appl.Cryst.*, 36, 2003.
- [53] <http://chemed.chem.purdue.edu/genchem/topicreview/bp/ch8/valenceframe.html>.
- [54] <http://epswww.unm.edu/xrd/xrdclass/06-diffraction-ii.pdf>.
- [55] Masayasu Tokonami. Atomic scattering factor for O<sup>2-</sup>. *Acta Cryst.*, 19, 1965.
- [56] Karlheinz Schwarz and Heniz Schultz. X-ray scattering factors for O<sup>2-</sup> and N<sup>3-</sup>. *Acta Cryst.*, A34, 1978.
- [57] Marcello Merli, Luciano Ungaretti, and Roberta Oberti. Leverage analysis and structure refinement of minerals. *American Mineralogist*, 85, 2000.
- [58] Tommy Nakken Aalerud. Synchrotron x-ray scattering studies of water intercalation in synthetic nickel-fluorohectorite. Master's thesis, Norwegian University of Science and Technology, 2001.
- [59] H. van Olphen. *An Introduction to Clay Colloid Chemistry*. John Wiley & Sons, second edition, 1977.
- [60] Jacob Israelachvili. *Intermolecular & Surface Forces*. Academic Press, second edition, 1995.

## Appendix A

# Lattice sum as Dirac's delta function

A brief proof of equation (1.16)

$$|S_N(\xi)| \longrightarrow \delta(\xi)$$

will be given.

For a geometrical series

$$S_N = \sum_{n=0}^{N-1} k^n = 1 + k + k^2 + \cdots + k^{N-1} = \frac{1 - k^N}{1 - k}$$

the sum is convergent in the limit  $N \rightarrow \infty$  if and only if  $|k| < 1$ , for which

$$S_\infty = \frac{1}{1 - k}$$

The multiplication of  $\vec{\mathbf{Q}}$  and  $\vec{\mathbf{R}}$  in equation (1.12) returns for *one dimension*  $2\pi(hn + \xi n)$ , setting  $k = i2\pi\xi$  in the geometrical series (as the term  $e^{i2\pi hn} \equiv 1$  for  $h, n = \text{integers}$ ). For  $\xi \rightarrow 0 \Rightarrow |k| \rightarrow 0$ , and

$$S_{N \rightarrow \infty} = 1$$

which shows that the lattice sum can be written in terms of a Dirac's delta function for  $N$  and  $\xi$  sufficiently large and small respectively.

## Appendix B

# Calculations of atomic form factor

### B.1 Detailed expression for the atomic form factor

The atomic scattering factor is given in Equation (1.8)

$$f(\vec{Q}, \hbar\omega) = f_0(\vec{Q}) + f'(\hbar\omega) + i f''(\hbar\omega)$$

where quantum mechanical, relativistic and other effects are included in  $f'$  and a phase lag is allowed for in  $f''$ .

However, a more elaborate expression will be discussed in this chapter. The atomic scattering factor is composed of a real and an imaginary part

$$f = \text{Re}(f) + i\text{Im}(f)$$

The real part can be expressed as

$$\text{Re}(f) = f_0 + f' = f_0 + f_{\text{corr}} + f_{\text{NT}}, \quad f_{\text{corr}} = f_1 + f_{\text{rel}} - Z \quad (\text{B.1})$$

where  $f_0$  is the 'normal' coherent scattering factor (Equation (1.7)),  $f_{\text{corr}}$  the correction term and  $f_{\text{NT}}$  the nuclear Thomson scattering. The correction term is composed of the non-relativistic anomalous dispersion  $f_1 - Z$  and the relativistic correction factor  $f_{\text{rel}}$ , where  $f_1$  is some tabulated value found in literature.

The imaginary part of the dispersion correction is simply linked to the photoeffect cross-section at the photon energy  $E$  and is, like  $f_1$ , found in literature.

$$\text{Im}(f) = f'' = f_2 \quad (\text{B.2})$$

### B.2 Calculations

The intensity is proportional to the atomic form factor squared (Equation (1.27)), hence

$$I \propto |f|^2 = f^* f = [\text{Re}(f)]^2 + [\text{Im}(f)]^2 = (f_0 + f_1 + f_{\text{rel}} - Z + f_{\text{NT}})^2 + f_2^2 \quad (\text{B.3})$$

<b>Electronegativity</b>	
H	2.20
Li	0.98
O	3.44
F	3.98
Na	0.93
Mg	1.31
Si	1.90

Table B.1: Values for electronegativity of the composite elements of Na-FH [53]

**Ionization** The atomic form factor,  $f$ , varies with the state of ionization. However, the scattering curves for neutral and fully ionized states differ significantly only at very low  $\frac{\sin \theta}{\lambda}$  values ( $< 0.3 \text{ \AA}^{-1}$ ), and the effects of ionization state are detectable only in that region [57].  $\frac{\sin \theta}{\lambda} \in [0.0227 \text{ \AA}^{-1}, 0.1216 \text{ \AA}^{-1}]$  for this experiment, thus a correction is appropriate. Different litterature propose different approaches.

The *electronegativity* of an atom is the relative ability of the atom to draw electrons in a bond towards itself. The electronegativities for the composite atoms in Na-FH are displayed in Table B.1.

The general rule is that when the difference in electronegativity of two elements is  $< 1.2$ , the bond between atoms of these elements is assumed to be *covalent*. For differences  $> 1.8$  we assume the bond to be *ionic*, while for intermediate differences, the bond is said to be *polar* or *polar covalent*.

Electronegativites summarise the tendency of an element to gain, lose or share electrons when it combines with another element. However, there are limits to the success of this application. For instance, Si and F have electronegativity differences ( $\Delta EN = 2.08$ ) which lead us to expect the bond to behave as if it was ionic, but the bond displays covalent character. This is due to that each element is assigned only one electronegativity value, which is used for all bonds. But fluorine is less electronegative when it bonds to semimetals, such as Si, or nonmetals than when it bonds to metals.

If one consider bonds between elements of more than one oxidation state, the ability to draw electrons in a bond towards itself becomes larger as the oxidation state of the atom increases. As the oxidation state becomes larger, the differences between the electronegativites for a metal and the nonmetal with which it combines decreases, and the bonds between these two elements therefore becomes less ionic (or more covalent). For instance, Si atoms in a +4 oxidation state is more electronegative than the same atoms in lower oxidations states, and the bonding of a nonmetal to this state displays a more covalent character than what is to be 'expected' [53].

Based on the above reasoning and other litterature [5], the halfionized atomic scattering factors are used for Si and silicate O, while fully ionized values are used for the other cations and F. For water the scattering factor is the sum of

the factors for H<sup>+</sup> and O<sup>2-</sup>.<sup>1</sup>

**'Normal' (non-dispersive) coherent scattering** The 'normal' coherent scattering factor (Equation (1.7)) is a function of the element and momentum transfer,  $\vec{Q}$ , which includes both a radiation energy dependence ( $\lambda$ ) and angular dependence ( $\sin \theta$ ) (through the Laue condition (or Bragg's law) for constructive interference (see page 12)). The function is normalized in units of the amount of scattering occurring from a single electron. The values are found in literature, generally expressed as a function of discrete values of  $\frac{\sin \theta}{\lambda}$  or as coefficients of polynomial fits to curves of these values.

For our purpose the values were found in literature [55] for the O<sup>2-</sup> ion and [46] for the remaining elements.<sup>2</sup>

As the coherent scattering factors are all given as discrete values as functions of  $\frac{\sin \theta}{\lambda}$ , a polynomial fit of 10th order was carried out for each of the elements. Thereby the factors are given as mathematical functions of  $\theta$  (as  $\lambda$  is constant (2.1.1)) and may be evaluated continuously over the proper angle interval for this present study. See Figure B.2.

**Dispersive scattering factors** The dispersive scattering factors were determined and extrapolated from tabulated values found in [29]. A graphical presentation is given in Figure B.2.

**f<sub>1</sub> and f<sub>2</sub>** The values for  $f_1$  and  $f_2$  are found in proper literature as a discrete function of the photon energy (E). Consequently a polynomial fit of 10th order was appropriate in order to determine the best interpolated values. See Figure B.2

The ionization state of an atom changes the position of the absorption edge on the energy scale. However, the radiation energy for this experiment was significantly beyond any absorption edges of the composite elements and thus did not represent any difficulties.

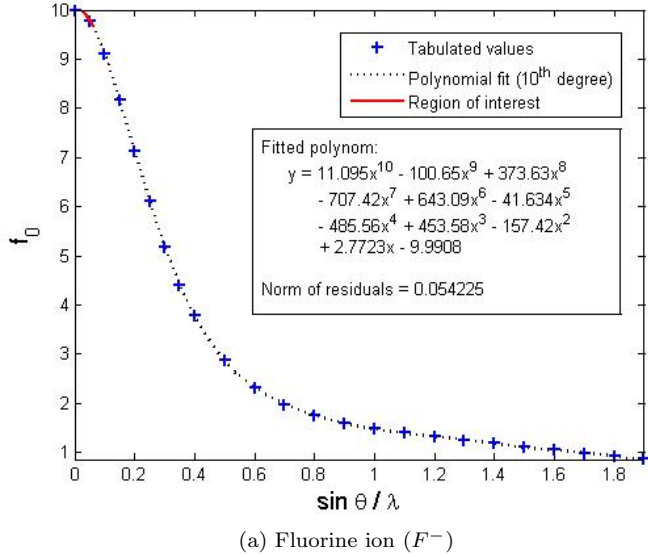
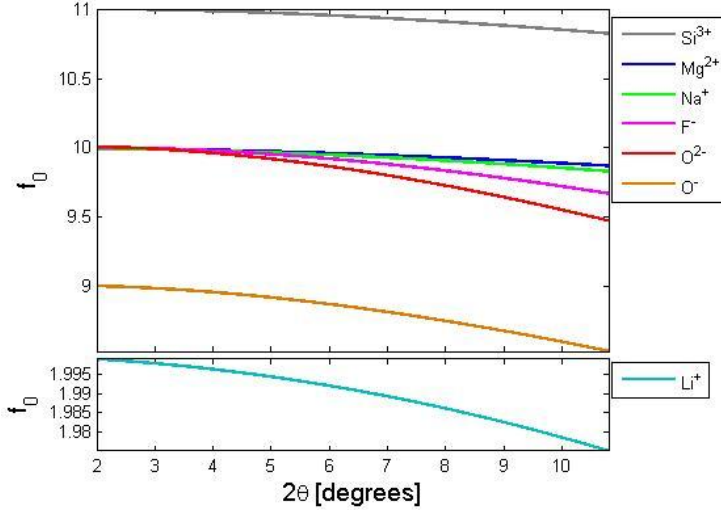
**Nuclear Thomson scattering** The nuclear Thomson scattering,  $f_{NT}$ , is small and negative in phase relative to the electronic form factor ( $f_0 + f_{corr}$ ). In this context this term may be neglected.

**Relativistic corrections** There are two different values (denoted  $f_{rel}^1$  and  $f_{rel}^2$ ) given for the relativistic correction of the scattering factor [29], but they may both be neglected in this context as they are of much smaller order than the other contributions. This goes for all the elements.

---

<sup>1</sup>This is generally also the case if there are any OH<sup>-</sup> present, as in normal hectorite.

<sup>2</sup>Coherent X-ray factors ( $f^0$ ) are available for atoms and some positive and negative ions. However, free negative ions such as O<sup>2-</sup> are unstable and therefore the corresponding form factors are not easily obtainable. Though, there are several methods for investigating these values (for instance [56]). The extent to which they differ by method chosen is insignificant in this context.

(a) Fluorine ion ( $F^-$ )

(b) All elements

Figure B.1: Non-dispersive ('normal') scattering factors. (a) Polynomial fit of 10<sup>th</sup> order for the fluorine ion ( $F^-$ ) taken as the example. The region of interest for our purpose is marked with a red line, corresponding to the angular interval of  $2\theta \in [2.0^\circ, 10.8^\circ]$ . (b) Non-dispersive scattering factor for  $2\theta \in [2.0^\circ, 10.8^\circ]$  for all the composite elements in Na-Fluorohectorite.

**Values for the composite elements in Na-FH** The summing up is done in Table B.2. Note that the non-dispersive term  $f_0$  is given as an interval corresponding to  $2\theta \in [2.0^\circ, 10.8^\circ]$ , the angular range studied in this experiment.

It is worth noting that the dependence of  $f$  upon the energy and angular dependence *may* not be strictly separable as indicated by the separation of  $f_0$

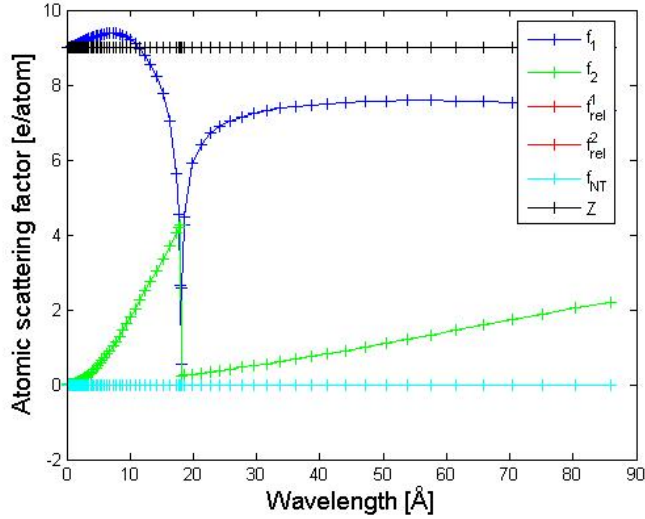


Figure B.2: Dispersive scattering factors (the fluorine ion ( $F^-$ ) taken as the example). We observe that  $f_1$ ,  $Z$  and to some extent  $f_2$  are the main contributing terms, whereas  $f_{NT}$  and  $f_{rel}$  may be neglected in this context. The special behaviour around  $\sim 18\text{\AA}$  corresponds to the K-shell edge limit. For higher elements, the higher order edge limits (LI, LII, LIII etc.) may also be visible for higher wavelengths (lower energy).

and  $f_{\text{dispersive}}$ .

### B.3 Atomic scattering factor squared

Equation (B.3) is tabulated for the elements in Na-Fluorohectorite in Table B.3 and displayed in Figure B.3 for the angular interval  $[2.0^\circ, 10.8^\circ]$ .

Elements <sup>†</sup>	Atomic form factors [e/atom]						f <sub>NT</sub>	f <sub>2</sub>
	f <sub>0</sub>	f <sub>1</sub>	f <sub>rel</sub>	Z				
H	-‡	1.0000	1.0519E-04, 0.0000E+00	1	-5.4423E-04	1.0724E-06		
Li	[1.9989,1.9751]	3.0014	-9.8613E-04, -6.0000E-04	3	-7.1131E-04	3.3350E-04		
O	[9.0035,8.5336] <sup>††</sup>	8.0519	7.7133E-03, -4.2000E-03	8	-2.1944E-03	3.1984E-02		
	[10.0070,9.4731] <sup>††</sup>							
F	[10.0027,9.6694]	9.0757	-9.9395E-03, -5.4000E-03	9	-2.3389E-03	5.2906E-02		
Na	[9.9942,9.8299]	11.1421	1.5378E-02, -8.4000E-03	11	-2.8873E-03	1.2311E-01		
Mg	[9.9962,9.8695]	12.1819	-1.8616E-02, -1.0800E-02	12	-3.2502E-03	1.7756E-01		
Si	[11.0013,10.8231]	14.2665	-2.6197E-02, -1.5600E-02	14	-3.8284E-03	3.2954E-01		

Table B.2: Atomic scattering factors for the composite elements of Na-fluorohectorite.

† The non-dispersive contribution ( $f_0$ ) is calculated for the *ionized* composites, whereas the dispersive contributions (the remaining factors) are calculated from the neutral atom. The implied discrepancy is not significant in this context.

† This is a direct result from the above assumption as we regard the  $H^+$  ion, which do not include any scattering electrons.

†† For the  $O^-$  case (silicate oxygen).

‡‡ For the  $O^{2-}$  case (water).

$ f ^2$ for $2\theta \in [2.0^\circ, 10.8^\circ]$
H            3.4535E-07†
Li          [3.9951,3.9006]
O          [81.8530,73.5716]‡
F          [101.0170,90.5710]††
Na          [101.3753,94.7750]
Mg          [102.4551,99.1559]
Si          [103.2587,100.7009]
Si          [126.5147,122.5386]

Table B.3: Atomic scattering factor squared for all of the composite elements of Na-FH.

† Hydrogen appears as  $H^+$ -ion (or proton). Thus there are no scattering electrons present, and only the dispersive contributions are included, for which the order indicates that they can be neglected.

† For the  $O^-$  case.

†† For the  $O^{2-}$  case.

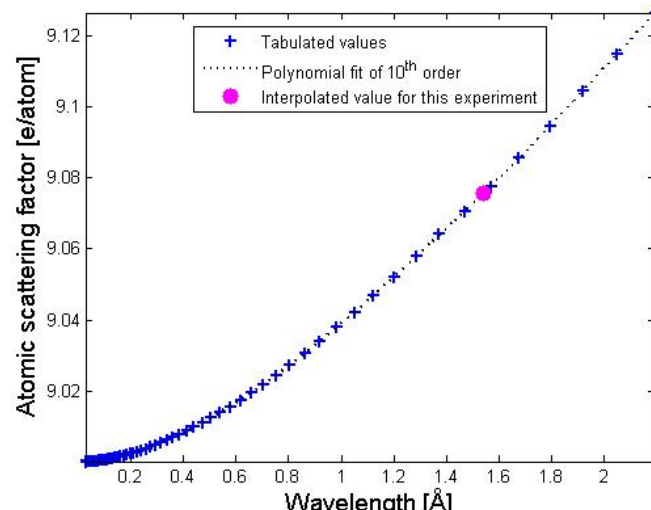
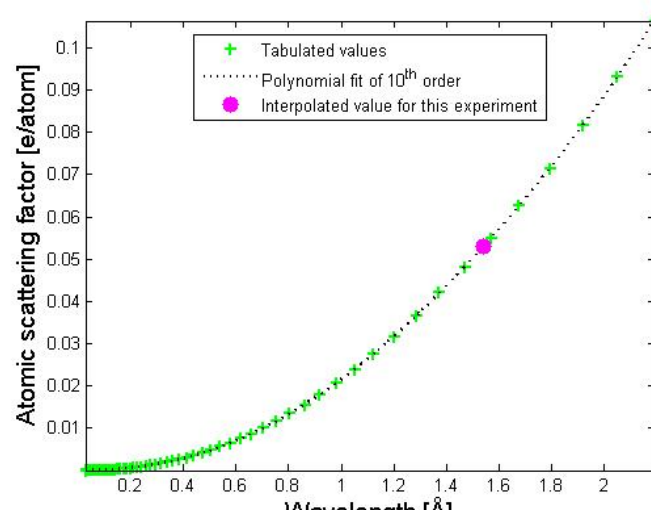
(a)  $f_1$ (b)  $f_2$ 

Figure B.3: Graphical representation of the non-dispersive scattering factors  $f_1$  and  $f_2$  for the fluorine ion ( $F^-$ ) and the corresponding polynomial fits. The interpolated values valid for this experiment are marked with big pink dots.

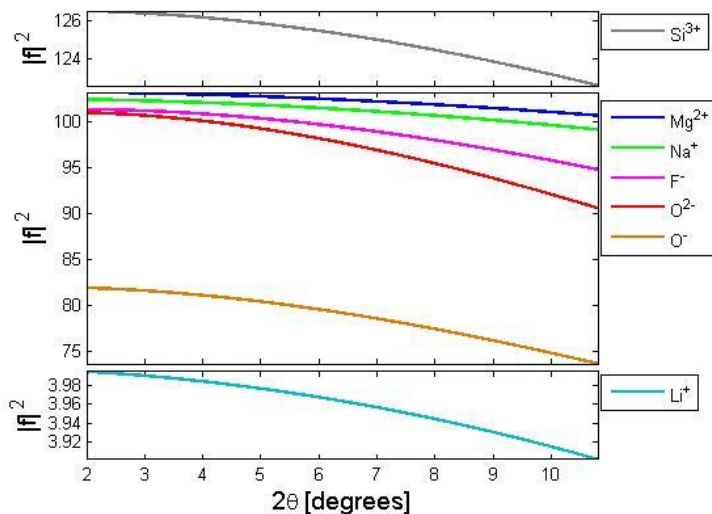


Figure B.4: Graphical representation of the atomic form factor squared for all of the composite elements of Na-FH.

## Appendix C

# MatLab script for peak fitting

```
0001 function [parameters,error_bars] = peakfitwax(matrix,G2Lp, ...
0002                               order,xpos,biased, ...
0003                               x_width_lower,x_width_upper, ...
0004                               display_graph,sensitivity,first,second,third)
0005
0006 % Pseudo-Voigtian fit to input data (matrix form)
0007 %   PARAMETERS =
0008 %   PEAKFITWAXS(MATRIX,G2LP,ORDER,XPOS,BIASED,X_WIDTH_LOWER,X_WIDTH_UPPER, ...
0009 %                           DISPLAY_GRAPH,SENSITIVITY,FIRST,SECOND,THIRD)
0010 %
0011 %   MATRIX:      normalized data input as a matrix
0012 %   G2LP:        layer structure and Lorentzpolarization vector
0013 %   ORDER:       order of G2Lp (this is due to avoid numerical
0014 %                 difficulties when operating with extremely small/large values)
0015 %   XPOS:        approximate peak position
0016 %   BIASED:      preferred direction of the weighing of the x-data
0017 %   X_WIDTH_LOWER: lower width of x-data on which to do the fit
0018 %   X_WIDTH_UPPER: upper width of x-data on which to do the fit
0019 %   DISPLAY_GRAPH: graphical comparison of the input and fitting (type
0020 %                     'y' for display, otherwise type 'n')
0021 %   SENSITIVY:    Criteria for aborting the least square fitting loop
0022 %   FIRST:        lower limit of left zone of interest for baseline appropximation
0023 %   SECOND:       upper limit of left zone of interest for baseline appropximation
0024 %   THIRD:        lower limit of right zone of interest for baseline appropximation
0025 %
0026 % Returns PARAMETERS - a matrix [mu,xc,w,A,wG,error_max,error_min,backgroundparameters]
0027 %   with the parameters for the pseudo-Voigtian fit found by the method of least squares
0028 %   approximation, and the parameters for the background fit.
0029 % and ERROR_BARS - a matrix [mu_error,xc_error,A_error]
0030 %   with the error bars for the design variables
0031 %
0032 % Made by:      Yves Meheust
0033 % Modified by:  Lars Ramstad Alme      Trondheim 27/03/06
0034 % Last revision: 15/06/06
0035 %
0036 % Ex:      fitwaxspeakbiasedbbsub(importplotsodata('C:\Integratedframes\...
0037 %                               scan001.plt'),f2,10^8,5.88,'l',0.3,0.3,'y',...
0038 %                               0.001,2,3.8,8.5)
0039
0040
0041
0042 % Loading of the data and reduction to the correct domain
0043 xdat=matrix(:,1);
0044 ydat=matrix(:,2);
0045 [xred,yred,imax]=Reducedata(xdat,ydat,xpos,x_width_lower,x_width_upper);
0046 [xred_2,G2Lpred,imax_2]=Reducedata(xdat,G2Lp./order,xpos,x_width_lower,x_width_upper);
0047
0048 %Determination of the baseline from normalized data
```

```

0049      [backgroundparameters,maxerror,minerror] = powerbaseline(matrix,first,second,third,display_graph);
0050
0051
0052 %Subtraction of baseline from normalized input data
0053     ysub = ydat-BackgroundFunction(backgroundparameters,xdat);
0054     xsub = xdat;
0055     yredsub = yred-BackgroundFunction(backgroundparameters,xred);
0056     xredsub = xred;
0057
0058 %Divide by Layer structure and Lorentzpolarizationfactors
0059     yredsubG2Lp = yredsub./G2Lpred;
0060
0061 % Initial values
0062     mu=0.5;
0063     xc=xredsub(imax);
0064     w=GetWidth(imax,xredsub,yredsubG2Lp,biased);
0065     A=0.5*yredsubG2Lp(imax)/((2*mu/(pi*w)) + (2*(1-mu)*nthroot((log(2)/pi)/w,2)));
0066
0067     par0(1)=mu;
0068     par0(2)=xc;
0069     par0(3)=w;
0070     par0(4)=A;
0071
0072 % Define set of lower and upper bounds on the design variables
0073 % (mu,xc,w,A,y0)
0074     LB = [0,0,0,0];
0075     UB = [1,Inf,Inf,Inf];
0076
0077 % Fitting of the data
0078     par=lsqcurvefit(@PseudoVoigt,par0,xredsub,yredsubG2Lp,LB,UB);
0079     mu=par(1);
0080     xc=par(2);
0081     w=par(3);
0082     A=par(4);
0083
0084     [parfit,squaredS,residual,exitflag,output,lambda,J]=...
0085                         lsqcurvefit(@PseudoVoigt,par,xredsub,yredsubG2Lp,LB,UB);
0086
0087     counter = 1;
0088     abort = false;
0089     approvedfit = true;
0090     while abs(1-parfit(1)/par(1))>sensitivity | abs(1-parfit(2)/par(2))>sensitivity | ...
0091             abs(1-parfit(3)/par(3))>sensitivity | abs(1-parfit(4)/par(4))>sensitivity
0092         par = parfit;
0093         [parfit,squaredS,residual,exitflag,output,lambda,J] = ...
0094                         lsqcurvefit(@PseudoVoigt,par,xredsub,yredsubG2Lp,LB,UB);
0095         if counter==1000          %aborts function if no satisfying approximation is reached
0096             parfit(:) = NaN;
0097             abort = true;
0098             break
0099         end
0100         counter = counter+1;
0101     end
0102     par = parfit;
0103
0104 % Estimation of the errors
0105     [dof,s,error_bars]=DetermineErrorBars(xred,par,squaredS,J);
0106
0107 % Criterias for an approved fit
0108     %Find max in the zone of interest
0109     wideinterval.width = 0.25;
0110     [xintervalsub,yintervalsub,iposmax]=Reducedata(xsub,ysub,xpos,wideinterval.width,wideinterval.width);
0111     [maxvalue_zoneofinterest,maxpos_zoneofinterest] = max(yintervalsub);
0112
0113     %Find max in a narrow interval around the expected peak
0114     narrowinterval.width = 0.15;
0115     [xposred,yposred,iposmax]=Reducedata(xsub,ysub,xpos,narrowinterval.width,narrowinterval.width);
0116     [maxvalue_zoneofpeak,maxpos_zoneofpeak] = max(yposred);
0117
0118     amp = amplitude(par);
0119     error = yredsubG2Lp-PseudoVoigt(par,xredsub);
0120     [error_max, error_max_pos] = max(error);
0121     [error_min, error_min_pos] = min(error);
0122

```

```

0123 ampfactor = 5; %for Criteria 3: the factor for which the fitted amplitude must exceed the
0124 %maximum deviation of the fit
0125 %Criteria 1: max value in zone of fit is within a narrow
0126 %interval around the expected peak
0127 if maxvalue_zoneofinterest>maxvalue_zoneofpeak
0128 message = ['Did not match criteria 1 - xmax = ',num2str(xintervalsub(maxpos_zoneofinterest))];
0129 par(:) = NaN;
0130 error.bars(:) = NaN;
0131 approvedfit = false;
0132 %Criteria 2: the calculated xc-value must lie within the same interval
0133 elseif par(2) < xpos-narrowinterval_width | xpos+narrowinterval_width < par(2)
0134 message = ['Did not match criteria 2 - calculated xc = ',num2str(par(2))];
0135 par(:) = NaN;
0136 error.bars(:) = NaN;
0137 approvedfit = false;
0138 %Criteria 3: amplitude of the fit is minimum 'ampfactor' times the maximum
0139 %deviation of the fit
0140 elseif amp < ampfactor*error_max | amp < abs(ampfactor*error_min)
0141 message = ['Did not match criteria 3 (amp=',num2str(amp), ...
0142 ', ', num2str(ampfactor),'*errormax=',num2str(ampfactor*error_max), ...
0143 ', ', num2str(ampfactor),'*errormin=',num2str(ampfactor*error_min)];
0144 par(:) = NaN;
0145 error.bars(:) = NaN;
0146 approvedfit = false;
0147 end
0148
0149
0150 % Visual comparison of the plot and data and return of the parameters
0151 if abort == false
0152 if display_graph == 'y'
0153 graphs = figure;
0154 graphs = subplot(3,1,1);
0155 yfit=PseudoVoigt(par,xsub);
0156 plot(xsub,ysub,'.b',xredsub,yredsubG2Lp.*G2Lpred,'.r',...
0157 xsub,PseudoVoigt(par0,xsub).*(G2Lp'./order),'-g',xsub,yfit.*(G2Lp'./order),'-k');
0158 legend('Data with background subtracted','Chosen data range for fitting',...
0159 'Initial guess','Pseudo-voigtian fit','Location','NorthEastOutside');
0160 if approvedfit == true
0161 title('Pseudo-Vogitian fit of experimental data');
0162 else
0163 title(['Not approved fit (pseudo-vogitian) of the peak (' ,message, ')']);
0164 end
0165
0166 subplot(3,1,2);
0167 yfitredsub=PseudoVoigt(par,xredsub)./order;
0168 plot(xredsub,yredsubG2Lp./order,'.r',xredsub,yfitredsub,'-k');
0169 legend('Data with background subtracted and corrected for |G|^2Lp',...
0170 'Pseudo-voigtian fit','Location','NorthEastOutside');
0171
0172 if approvedfit == true
0173 subplot(3,1,3);
0174 plot(xredsub,error./order,'.b',xredsub,0,:k',xredsub(error_max_pos), ...
0175 error_max./order,'or',xredsub(error_min_pos),error_min./order,'or');
0176 text(xredsub(error_max_pos),1.1*error_max./order,... ...
0177 ['Max error']); % = ',num2str((error_max./order));
0178 text(xredsub(error_min_pos),0.9*error_min./order,... ...
0179 ['Min error']); % = ',num2str(error_min./order));
0180 legend('Error in pseudo-voigtian fit','Location','NorthEastOutside');
0181 end
0182 end
0183
0184 %Deduce the natural widths of the peak:
0185 if approvedfit == true;
0186 global omega;
0187 global eta;
0188 omega=w;
0189 eta=mu;
0190
0191 wL_init=omega;
0192 wL = fsolve(@wL2eta,wL_init);
0193
0194 global gammaL;
0195 gammaL=wL;
0196

```

```

0197     wG_init=omega/2;
0198     wG = fsolve(@wG2w,wG_init);
0199
0200     parameters = [par,wL,wG,error_max,error_min,backgroundparameters];
0201     return
0202 else
0203     parameters = [par,NaN,NaN,NaN,NaN,backgroundparameters];
0204 end
0205 else
0206     parameters = [par,NaN,NaN,NaN,NaN,backgroundparameters];
0207     return
0208 end
0209
0210
0211
0212
0213
0214 %%%%%%
0215 %%%%
0216 %%%% Subroutines
0217 %%%%
0218 %%%% Subroutine wG2w
0219 %%%%
0220 function y=wG2w(x)
0221 global omega;
0222 global gammal;
0223 omega;
0224 gammal;
0225 y=(x.^5+2.69269*gammal*x.^4+2.42843*gammal.^2*x.^3+...
0226 4.47163*gammal.^3*x.^2+0.07842*gammal.^4*x+gammal.^5).^(1/5)-omega*ones(1,length(x));
0227 return
0228
0229
0230 %%%% Subroutine wl2eta
0231 %%%%
0232 function y=wl2eta(x)
0233 global omega;
0234 global eta;
0235 %omega
0236 %eta
0237 aux=x/omega;
0238 y= 1.36603*aux-0.47719*aux.*aux+0.11116*aux.^3-eta*ones(1,length(aux));
0239 return
0240
0241
0242 %%%% Subroutine Reducedata
0243 % Subroutine Reducedata
0244 function [x,y,imax]=Reducedata(xdat,ydat,xpos,x_width_lower,x_width_upper)
0245 j=0;
0246 for i=1:length(xdat)
0247 if ( xdat(i)<=xpos & (xpos-xdat(i)) <= x_width_lower ) | ...
0248 ( xdat(i)>=xpos & (xdat(i)-xpos) <= x_width_upper )
0249 j=j+1;
0250 x(j)=xdat(i);
0251 y(j)=ydat(i);
0252 index(j)=i;
0253 end
0254 end
0255 [ypos,imax]=max(y);
0256 return
0257
0258
0259 %%%% Subroutine Getwidth
0260 %%%%
0261 function w=GetWidth(imax,xred,yred,biased)
0262 i=imax;
0263 [xred_max, xred_max_pos] = max(xred);
0264 [xred_min, xred_min_pos] = min(xred);
0265
0266 if biased == 'r'
0267 while yred(i)>yred(imax)/2
0268 if i==xred_max_pos
0269 [ymin, imin] = min(yred); %this if-sequence will be activated when the
0270 xredhalf = xred(imin);

```

```

0271         break
0272     end
0273     i=i+1;
0274     xredhalf = xred(i);
0275   end
0276 elseif biased == '1'
0277   while yred(i)>yred(imax)/2
0278     if i==xred_min_pos %this if-sequence will be activated when the
0279       [ymin, imin] = min(yred); %peak is smaller than the surrounding background
0280       xredhalf = xred(imin);
0281       break
0282     end
0283     i=i-1;
0284     xredhalf = xred(i);
0285   end
0286 else
0287   'Biased must be assigned (1/r)'
0288   return
0289 end
0290 w=abs(xredhalf-xred(imax));
0291
0292 %%%%%%%%%%%%%%%%%%%%%%%%%%%%%%%%%%%%%%
0293 % Subroutine 'PseudoVoigt'
0294 function f=PseudoVoigt(par,xdata)
0295
0296 % Parameters
0297 mu=par(1);
0298 qc=par(2);
0299 w=par(3);
0300 A=par(4);
0301
0302 % Computation of the function at abscisse value q
0303 x=xdata-qc;
0304 hw1=w/2;
0305 fact1=sqrt(log(2)/pi)/hw1;
0306 intens1=(1-mu)*fact1*exp(-log(2)*(x.*x)/(hw1*hw1));
0307 hw2=w/2;
0308 fact2=1/(hw2*pi);
0309 intens2=(mu)*fact2./(1+(x.*x)/(hw2*hw2));
0310 f=A*(intens1+intens2);
0311
0312 return
0313
0314
0315 %%%%%%%%%%%%%%%%%%%%%%%%%%%%%%%%%%%%%%
0316 % Subroutine BackgroundFunction
0317 function f = BackgroundFunction(param,xdata)
0318   f = param(3).*xdata.^param(2)+param(1);
0319   return
0320
0321
0322 %%%%%%%%%%%%%%%%%%%%%%%%%%%%%%%%%%%%%%
0323 % Subroutine DetermineErrorBars()
0324 function [dof,s,error_bars_vec]=DetermineErrorBars(xdata,par,squaredS,J)
0325   dof=length(xdata)-length(par); %degree of freedom
0326   s=sqrt(squaredS/dof);
0327   %fprintf('Chi2 = %f\t dof = n - p = %d\t Chi2/(n-p) = %f\n',squaredS,dof,s*s);
0328   C=inv(transpose(J)*J);
0329
0330   for i=1:length(par)
0331     error_bars_vec(i)=s*sqrt(C(i,i));
0332   end
0333
0334 return
0335

```

# List of Figures

1.1	Schematic diagram of single a silicate tetrahedron and a single aluminium or magnesium octahedral unit. Taken from [3] . . . . .	2
1.2	Various views of tehtrahedral and octahedral layers. Taken from [4] . . . . .	2
1.3	Schematic diagrams of 1:1, 2:1 and 2:1+1 platelets. Taken from [5]	3
1.4	Location and type of water in a clay mineral. . . . .	5
1.5	Schematic diagrams of a smectite clay mineral. Taken from [13].	6
1.6	Generic structure of smectite with intercalated water. Taken from [17] . . . . .	7
1.7	Typical hydration states in smectites. . . . .	7
1.8	Offset in a clay mineral. Modified from [13] . . . . .	8
1.9	Possible structures generated from the 1nm thick platelet of a swelling clay. Taken from [18] . . . . .	9
1.10	Different types of exchange sites on clay particles. . . . .	10
1.11	AFM photographs of Na-fluorohectorite. . . . .	11
1.12	Bragg scattering geometry. Taken from [24]. . . . .	14
1.13	Phase difference in atom scattering. Taken from [26]. . . . .	15
1.14	Uncollimated scattering from a crystallite. Taken from [23]. . . . .	20
1.15	Ideal powder diffraction and the Debye-Scherrer cone. Taken from [23]. . . . .	22
1.16	Diffraction grating. Modified from [28] . . . . .	25
1.17	Proportions and spatial configuration of Na-FH. Taken from [7].	28
1.18	Graphical representation of the layer structure factor squared. . . . .	30
1.19	Graphical representation of the Lorentz-polarization factor. . . . .	30
1.20	Graphical representation of the squared layer structure and Lorentz-polarization factor. . . . .	31
1.21	Graphical representation of the interference function. . . . .	32
1.22	Graphical comparison of the different factors. . . . .	33
1.23	Theoretical modelled intensity for pure hydration states in Na-fluorohectorite. . . . .	33
1.24	Gaussian and Lorentzian distributions. Taken from [43]. . . . .	42
1.25	Voigtian distribution. Taken from [43]. . . . .	43
2.1	NanoSTAR hardware. Taken from the Bruker webpage. . . . .	45
2.2	Linefocus to 'point' focus. . . . .	46
2.3	Göbel mirrors optics. Taken from [21]. . . . .	46
2.4	Pinhole collimating system. Taken from [21]. . . . .	47
2.5	Sample holder . . . . .	48

2.6	Setup of the circulating air . . . . .	49
2.7	Mortar and X-ray glass capillary . . . . .	50
2.8	Schematic illustration of the scattering geometry. . . . .	51
2.9	Sample nanography . . . . .	52
3.1	Photoseries of time-evolution of Debye-Scherrer scattering rings. . . . .	55
3.2	Radial integration of raw data (pixel frame). . . . .	56
3.3	Angular step size as a function of pixel resolution. . . . .	57
3.4	Fitting of the background noise and subtraction from data. . . . .	59
3.5	Division of the background subtracted data by the layer structure and Lorentz-polarization factors. . . . .	60
3.6	Pseudo-Voigtian peak fit. . . . .	61
3.7	Monohydrated peak displacement. . . . .	64
3.8	Instrumental peak broadening. . . . .	66
3.9	Sample peak broadening. . . . .	67
3.10	Sample anisotropy. . . . .	68
3.11	Time evolution of the (001) Bragg diffraction curves (fixed position). . . . .	70
3.12	Spatial evolution of the (001) Bragg diffraction curves ('fixed' time). . . . .	71
3.13	Determination of the peak ratio of pure hydration states applied for normalization. . . . .	72
3.14	Time evolution of the <i>normalized</i> (001) Bragg peak intensities (fixed position). . . . .	73
3.15	Spatial evolution of the <i>normalized</i> (001) Bragg peak intensities ('fixed' time). . . . .	74
3.16	3D representation of the normalized hydration dynamics. . . . .	75
3.17	Function fit of the intercalation front. . . . .	76
3.18	Normalized intensities at the end of the experiment. . . . .	77
3.19	Data collapse with a spatio-temporal scaling variable. . . . .	79
3.20	Silanization of hydrophilic glass surface with reactive chlorosilane. . . . .	81
3.21	Microscope photograph of a silanized and a non-treated glass capillary. . . . .	81
3.22	Disordered intercalation. . . . .	82
3.23	Suggested relation between the humidity gradient and intercalation front. . . . .	85
3.24	Semi-log plot of the evolution of normalized hydration states. . . . .	86
B.1	Non-dispersive scattering factors. . . . .	98
B.2	Dispersive scattering factors fluorine. . . . .	99
B.3	Graphical representation of the non-dispersive scattering factors $f_1$ and $f_2$ for the fluorine ion . . . . .	101
B.4	Atomic scattering factors squared. . . . .	102

# List of Tables

1.1	Atomic scattering factors squared. . . . .	28
1.2	Values for the layer structure factor. . . . .	29
B.1	Electronegativites. . . . .	96
B.2	Atomic scattering factors for the composite elements of Na-FH. .	100
B.3	Atomic scattering factors squared. . . . .	100